



저작자표시-비영리-변경금지 2.0 대한민국

이용자는 아래의 조건을 따르는 경우에 한하여 자유롭게

- 이 저작물을 복제, 배포, 전송, 전시, 공연 및 방송할 수 있습니다.

다음과 같은 조건을 따라야 합니다:



저작자표시. 귀하는 원저작자를 표시하여야 합니다.



비영리. 귀하는 이 저작물을 영리 목적으로 이용할 수 없습니다.



변경금지. 귀하는 이 저작물을 개작, 변형 또는 가공할 수 없습니다.

- 귀하는, 이 저작물의 재이용이나 배포의 경우, 이 저작물에 적용된 이용허락조건을 명확하게 나타내어야 합니다.
- 저작권자로부터 별도의 허가를 받으면 이러한 조건들은 적용되지 않습니다.

저작권법에 따른 이용자의 권리는 위의 내용에 의하여 영향을 받지 않습니다.

이것은 [이용허락규약\(Legal Code\)](#)을 이해하기 쉽게 요약한 것입니다.

[Disclaimer](#)

공학박사 학위논문

**Study on Kinetics of Vibrationally
Excited Hydrogen Molecule in
Hydrogen Negative Ion Source**

수소 음이온원에서 진동 여기 수소 분자의
거동에 대한 연구

2016년 8월

서울대학교 대학원

에너지시스템공학부

당 정 증

Study on Kinetics of Vibrationally Excited Hydrogen Molecule in Hydrogen Negative Ion Source

지도 교수 황 용 석

이 논문을 공학박사 학위논문으로 제출함
2016년 4월

서울대학교 대학원
에너지시스템공학부
당 정 증

당정증의 공학박사 학위논문을 인준함
2016년 6월

위 원 장 김 곤 호 (인)

부위원장 황 용 석 (인)

위 원 조 용 섭 (인)

위 원 유 석 재 (인)

위 원 정 경 재 (인)

Abstract

Study on Kinetics of Vibrationally Excited Hydrogen Molecule in Hydrogen Negative Ion Source

Jeong-Jeung Dang

Department of Energy System Engineering

The Graduate School

Seoul National University

Hydrogen negative ion source is a very useful ion source which is utilized in a proton accelerator or a neutral beam injector for fusion plasma heating and current drive. The negative ion is favored in these applications by its high neutralization efficiency. The negative ion production mechanism can be categorized as two types. The first one is a volume production mechanism which produces the negative ion via a dissociative electron attachment (DA) reaction with a vibrationally excited hydrogen molecule and a low energy electron. The other mechanism is a surface production occurred when a hydrogen atom or an atomic ion collide with the surface deposited by a low work function material such as the cesium. The negative ion source in Seoul National University adopts the volume production mechanism. In order to enhance an efficiency of the volume production, there is a magnetic filter field perpendicular to the axis of the ion source. The magnetic filter field generates a large gradient of the electron temperature between a driver region and an extraction region. The high energy electron in the driver region maintains a discharge and efficiently excites vibrational states of the molecule. Contrarily, the low energy electron at the extraction region is favorable to the DA reaction and

prevents the destruction of the negative ion by an electron impact detachment.

In order to understand the physics and characterize the ion source designed according to the volume production mechanism and the magnetic filter concept, various diagnostics are carried out. The plasma parameters such as the electron temperature and density are measured by an axially moving Langmuir probe. The negative ion density at the extraction region is diagnosed by a photo-detachment technique with Nd:YAG laser. To determine a vibrational state distribution function (VDF), the Fulcher- α spectroscopy is introduced. However, the Fulcher- α spectroscopy could not give an information on the higher vibrational states ($v>4$) which are key elements in the DA reaction. Therefore, the VDF is modeled by a particle balance equation and compared with the spectroscopic measurement. As a result, it is confirmed that the VDF of the present negative ion source is in a non-Boltzmann distribution which requires a special treatment of the Fulcher- α spectroscopy for the VDF determination. A zero-dimensional model is developed to get a correct VDF by the Fulcher- α spectroscopy.

Though the zero-D VDF model successfully identifies the relationship between the VDF and the Fulcher- α spectrum, the negative ion density estimation from the zero-D model is still deviated from that of the laser photo-detachment diagnostics. Thus, one-dimensional model is developed to account for the effect by the collision of excited hydrogen molecules during the transport from the driver region to the extraction region. It is found by the 1-D model that higher vibrational states are relaxed by the collision with the hydrogen atom or molecule. Consequently, the molecules in the higher vibrational states transit into the lower states when they arrive at the extraction region. Thus, the 1-D model greatly improves the negative ion density estimation in the consideration of the vibrational relaxation. Especially, the vibrational-translational (V-T) energy transfer reaction becomes important at high pressure regime. Thus, the over-estimation tendencies of the 0-D and the Boltzmann VDF model are corrected in the 1-D model at the high pressure regime.

Also, the 1-D model is applied to a short length ion source and its result is compared with the diagnostic result, in order to examine effect of the chamber length on the VDF. The result of 1-D model is well matched when the transport length is set as the shortened length, while the negative ion density is underestimated when the transport length is assumed as the same as that of the long length ion source. Thus, it is confirmed that the transport of the hydrogen molecule depends on the chamber length.

Based on the numerical and experimental study, it is identified that the vibrational relaxation of the hydrogen molecule can be represented by the two characteristics length, the effective mean free path and the transport length. The effective mean free path is defined as the diffusive speed divided by the effective collision frequency. The effective mean free path represents the rate of the vibrational relaxation during the vibrationally excited molecule travels from the driver region to the extraction region. The effective mean free path strongly depends on the operating pressure of the ion source. It is shortened at the high pressure by the V-T energy transfer collision with the hydrogen atom and molecule. The transport length represents the distance that the vibrationally excited molecule should be transported, in order to produce negative ion at the extraction region. The transport length is mainly determined by the source geometry and adjusted by the plasma parameter profile. Thus, the efficiency of the negative ion production is enhanced when the effective mean free path is longer than the transport length. In order to satisfy this condition in the negative ion source, the negative ion source should be operated with lower pressure. Also, the strong filter field is required to control the increased electron temperature at the extraction region by the low operating pressure. In addition, thickness of the magnetic filter region should be made short because the transport length should be sustained as short as possible. This concept can be examined by the experiment conducted at TRIUMF. TRIUMF tried several types of the magnetic filter configurations, where the strong and thin

magnetic filter was found to be the most effective without knowing the reason why the thin and strong magnetic filter was favored in the negative ion source. Based on this study, the dependency of the negative ion density on the magnetic filter configuration can be easily understood.

Other important parameter to characterize molecular behavior is the degree of dissociation since the dissociated atom is a main source for the V-T relaxation and the negative ion destruction. In addition, higher dissociation degree leads toward depletion of the hydrogen molecule which is a precursor of the negative ion. Thus, it is investigated that the relationship between the negative ion density and the degree of dissociation which is determined by the optical diagnostic measurements with numerical analyses. The degree of dissociation increases as the rise of the electron temperature and the density. Thus, if the negative ion source is operated at the condition mentioned in previous paragraph, there should be an optimum pressure to maximize the negative ion density since the dissociation of the hydrogen molecule by the high electron temperature at low pressure causes deleterious effect on the negative ion production. Also, the electron density enhancement with higher power cannot increase the negative ion density indefinitely. The negative ion density at high power is saturated and the power efficiency is declined.

In this study an improved one-dimensional VDF model considering the plasma parameters in the negative ion source is developed by accounting for the limitation when the non-Boltzmann VDF is diagnosed by the conventional Fulcher- α spectroscopy. Also, the improved 1-D model can simulate the transport of the hydrogen molecule and the vibrational state relaxation by the collision during the transport from the driver region to the extraction region. In addition, it is examined that the effective mean free path of the vibrationally excited molecule should be longer than the transport length to improve the negative ion production. Also, to optimize the operating condition of the negative ion source, it should be considered

that the kinetics of the hydrogen molecule such as the VDF and the degree of dissociation as well as the plasma parameters. This study is expected to be useful to comprehend the magnetically filtered negative ion source.

Keywords: Hydrogen plasma, Hydrogen negative ion source,
Hydrogen molecule vibrational distribution function,
Fulcher- α spectroscopy, Particle balance equation,
Hydrogen molecule transport

Student Number: 2011-30287

Contents

Chapter 1. Introduction	1
1.1. Volume Production Negative Ion Source.....	1
1.1.1. Volume Production Mechanism of Hydrogen Negative Ion.....	4
1.1.2. Magnetically Filtered Negative Ion Source.....	13
1.2. Motivation and Scope of Study	14
Chapter 2. RF Driven Negative Ion Source and Its Diagnostics	18
2.1. RF Driven Negative Ion Source	18
2.1.1. Overall Structure of the Negative Ion Source.....	18
2.1.2. Magnetic Field Structure in Negative Ion Source.....	21
2.2. Langmuir Probe and Profile Measurement of Plasma Parameters	24
2.2.1. Axially- Scanning Langmuir Probe.....	24
2.2.2. Plasma Parameters in Negative Ion Source	28
2.2.3. Profile of Plasma Parameters.....	30
2.3. Laser Photo-Detachment for the Negative Ion Density Measurement	33
2.4. Fulcher- α Spectroscopy	38
2.4.1. Rotational and Gas Temperature Determination by Fulcher- α Band Spectrum.....	41
2.4.2. Vibrational Temperature Determination by Fulcher- α Spectroscopy	44

Chapter 3. 0-D Model for Vibrational Distribution Function of H₂	47
3.1. Particle Balance Model for VDF	47
3.1.1. Primary Description on the 0-D VDF Model	48
3.1.2. Collision Processes in 0-D VDF Model	49
3.2. Corona Model for Fulcher- α Intensity Ratio.....	58
3.3. Negative Ion Density Estimation.....	63
3.4. Result and Limitation of 0-D VDF Model.....	64
Chapter 4. 1-Dimensional Transport Model to Describe the Relaxation of the Vibrational Distribution Function of the Hydrogen Molecule in Negative Ion Source	69
4.1. Structure of 1-D Transport Model for VDF of H ₂	69
4.2. Main Result of the 1-D Model	76
Chapter 5. Analysis of Kinetics of Vibrational Distribution Function of Hydrogen Molecule in Negative Ion Source	80
5.1. Vibrational Relaxation and Negative Ion Density	80
5.1.1. Vibrational Relaxation and Effective Mean Free Path.....	80
5.1.2. Vibrational Relaxation and Transport Length.....	84
5.2. Degree of Dissociation and Negative Ion Density	91
Chapter 6. Conclusion	95

Appendix A. Determination of Degree of Dissociation with Wide-Range Spectrograph	97
Bibliography	110
Abstract in Korean.....	119

List of Figures

- Figure 1.1. Schematic view of the tandem accelerator. The negative ion is injected into the accelerator and changed the polarity. Thus, negative ion is accelerated at left-hand-side of the gas stripper and the stripped positive ion is accelerated again with the single positive high voltage supply..... 3
- Figure 1.2. The orbit of the negative ion injected into the circular accelerator or storage ring. 3
- Figure 1.3. Cross section of the charge neutralization. The cross section of the positive ion decreases enormously faster than that of the negative ion above 10 keV [3]. 4
- Figure 1.4. Potential energy curves for relevant electronic states of hydrogen molecule (solid lines) and H_2^- ion (dashed lines) [13]. Horizontal lines laid on $X^1\Sigma_g^+$ -state of hydrogen are the vibrational energy of each vibrational state. 7
- Figure 1.5. The cross section of the dissociative electron attachment. There are three peaks corresponding DA channels via $X^2\Sigma_u^+$, $B^2\Sigma_g^+$ and $C^3\Sigma_g^+$ -states of the H_2^- ion, respectively [14, 15]. 8
- Figure 1.6. Cross section of the dissociative electron attachment for several vibrational states..... 8
- Figure 1.7. Transition diagram of e-V reaction. Potential curves of $H_2(X^1\Sigma_g^+)$ state (solid line) and $H_2^-(X^2\Sigma_u^+)$ state (dashed line). The vibrational

states of $H_2(X^1\Sigma_g^+)$ are expressed as horizontal solid lines.	10
Figure 1.8. Transition diagram of E-V reaction. The electronic states of H_2 is excited to $H_2(B^1\Sigma_u^+)$ state and decays to electronic ground state with radiation. Both the vibrational excitation and de-excitation are available in the E-V reaction.	11
Figure 1.9. Reaction rates of the E-V and e-V reactions exciting vibrational number 0 to 7 state. The reaction rate of the E-V reaction is about 4 or 5 orders of magnitudes larger than that of the e-V reaction.	12
Figure 1.10. Schematic figure of magnetically filtered negative ion source. The vibrationally excited molecule by the e-V and E-V reaction in the driver region is moved to the extraction region. The negative ion is produced by DA reaction in the extraction region.	13
Figure 2.1. Cross-sectional view of the negative ion source, arrangement of beam extraction and acceleration electrodes and electric circuit.	18
Figure 2.2. Cross-sectional view of the ion source with different chamber length and the diagnostic tools or set-up.	19
Figure 2.3. Arrangement of cusp field magnets and virtual filter magnets.	21
Figure 2.4. Simulation result for cusp field strength at the driver region.	22
Figure 2.5. Filter field strength along the filter field direction (solid line) and perpendicular direction to the filter field line (dashed line).	23
Figure 2.6. Comparison of the simulation result and the measured filter field strength along the axis of the ion source.	23

Figure 2.7. Diagram of the Langmuir probe and the RF compensation circuit. . .	25
Figure 2.8. Example of I-V curve analysis results obtained from computer based analysis code	27
Figure 2.9. (a) Electron temperature and (b) density of the long chamber according to the operation pressure and RF power.....	28
Figure 2.10. (a) Electron temperature and (b) density of the short chamber according to the operation pressure and RF power.....	29
Figure 2.11. Typical plasma parameter profiles in negative ion source with different chamber length and the filter field strength.	32
Figure 2.12. Diffusion of the electron and ion in the filter magnetic field. The electron flows along the field line and the ions flows across the field line. Thus, net current is generated at the wall.	33
Figure 2.13. Schematic view of laser photo detachment system.	34
Figure 2.14. Dependence of the photo-detachment for the laser energy density and the laser wavelength.	36
Figure 2.15. Photo-detachment current when laser ablates the probe surface.....	37
Figure 2.16. Typical laser photo-detachment signal and photo diode signal detecting laser pulse.	38
Figure 2.17. Energy level diagram for Fulcher- α spectrum related electronic and vibrational states of hydrogen molecule. The vibrational states of the lower and the upper Fulcher state are displayed only first 6 states	

$(\nu=0\sim 5)$	39
Figure 2.18. Typical Fulcher- α spectrum measured at negative ion source. The spectra from the first four vibrational and first five rotational states are depicted. Only these spectra are used in the diagnostics.	40
Figure 2.19. The Boltzmann plot of the rotational lines of (d, ν) -state. Each Boltzmann plots show good linearity and the rotational temperatures are matched within about 10% error.....	43
Figure 2.20. Gas temperature of the negative ion source (long chamber). Input RF power is (a) 700 W and (b) 900 W.....	43
Figure 2.22. Fulcher- α intensity ratio obtained in negative ion source (long chamber). Input RF power is 700 W.....	45
Figure 2.23. Negative ion density measured by the laser photo detachment and estimated by the Boltzmann VDF	46
Figure 3.1. Re-populating probabilities by the wall collision [63].	56
Figure 3.2. Comparison of the Fulcher- α intensity ratio determined by the experiment and the 0-D VDF model at the driver region of the long chamber and 700 W RF input power.	66
Figure 3.3. VDF obtained by 0-D model at the long chamber with RF input power 700 W. Dashed line is the Boltzmann distribution estimated from the lower vibrational states.....	67
Figure 3.4. The negative ion density obtained by the experiment, Boltzmann VDF and 0-D VDF model at the long chamber discharged by 700 RF power.	68

Figure 4.1.	Discretized chamber by the disk elements.....	70
Figure 4.2.	Discretization of equation (4.8).....	71
Figure 4.3.	Transport region and the electron temperature profile.....	73
Figure 4.4.	Comparison of the diffusive and advective speed.	74
Figure 4.5.	Scale length, normalized density and mean free path of the hydrogen molecule in vibrational state 7.	75
Figure 4.6.	Fulcher- α spectrum intensity ratio calculated by the 1-D model and measured by the spectrometer at the extraction region.....	77
Figure 4.7.	VDF calculated by the 1-D model with 4 Pa and 700 W discharge condition at the long chamber. The Boltzmann VDF estimated by the lower states (dashed line: driver region, dotted line: extraction region).	78
Figure 4.8.	Comparison of the negative ion density obtained by the experiment, Boltzmann VDF, the 0-D VDF model, and the 1-D model.....	79
Figure 5.1.	Mean free path for the relevant processes affecting VDF. The mean free paths of V-T with atom and molecule are strongly depends on the operating pressure, (a) 0.4 Pa and (b) 4 Pa.	81
Figure 5.2.	Pressure dependence of the absolute value of the effective mean free path of hydrogen molecule in vibrational state 7. The effective mean free path has the negative sign, because the vibrational state 7 decays.	83
Figure 5.3.	The effective mean free paths of the respective vibrational states. The effective mean free paths of the higher states are shorter than the lower states. The effective mean free paths of the lower states are elongated,	

because the depopulation of the higher states populates the lower states.....	84
Figure 5.4. Density profile obtained by the 1-D model, according to the position.	85
Figure 5.5. The negative ion density calculation in the short chamber with different transport length.	86
Figure 5.6. Variation of the transport length according to the pressure.....	87
Figure 5.7. The negative ion density calculation with constant transport length and the transport length depending on the pressure.	87
Figure 5.8. The negative ion density calculation with the fitted plasma parameters.	88
Figure 5.9. Filter magnet arrangement fabricated at TRIUMF.	89
Figure 5.10. Dependence of the negative ion current on the filter magnet structure [65].	90
Figure 5.11. Degree of dissociation in long chamber negative ion source discharged by 700 W RF power.	93
Figure 5.12. Dependency of the electron density, degree of dissociation and negative ion density on the RF power. In spite of the increase of the electron density, the negative ion density increases and becomes saturated. Thus, the ion source has the optimum RF power efficiency, because the degree of dissociation increases too.	94

Figure A.1. Full range spectrum of the hydrogen plasma measured by wide-range spectrometer.	99
Figure A.2. Rescaled graphs of each vibrational states (a: 0-0, b: 1-1, c: 2-2, d: 3-3) spectra of Fulcher- α transition. For comparison, the high resolution spectrometer data are also plotted	100
Figure A.3. Example of synthesizing the broadened and superposed spectrum by homemade MATLAB [®] code.	102
Figure A.4. Boltzmann plot and Rotational temperature of Fulcher- α 0-0 band spectrum.....	103
Figure A.5. Fulcher- α 1-1 band spectrum.....	104
Figure A.6. Boltzmann plot and Rotational temperature of Fulcher- α 1-1 band spectrum.....	105
Figure A.7. Boltzmann plots for vibrationally-excited Fulcher- α spectra measured by the high resolution spectrometer.....	106
Figure A.8. Rotational temperatures determined from the 0-0 Fulcher band spectra measured by the high resolution spectrometer and the low resolution spectrometer improved by the synthetic spectrum method.	108
Figure A.9. Degree of dissociation determined by the wide-range spectrum, synthetic spectrum method, and high resolution spectrum.	109

List of Tables

Table 1.1.	Numerical models for the negative ion source.	16
Table 1.2.	Summary of VDF diagnostics	16
Table 3.1.	List of volumetric collision processes of atom, ions and vibrationally unresolved molecule and descriptions.	50
Table 3.2.	List of volumetric collision processes of vibrationally resolved molecule and description.	51
Table 3.3.	List and description on wall collision processes included in the model.	52
Table 3.4.	Coefficients in the formula for the collisional integral.	54
Table 3.5.	Coefficients for the vibrational relaxation by the wall collision [23].	55
Table 3.6.	Radiative transition probability[s ⁻¹] of the Fulcher- ν transition for relevant vibrational number, $(d^3\Pi_u^-, \nu')$ - $(a^3\Sigma_g^+, \nu')$ transition....	60
Table 3.7.	Life time of $d^3\Pi_u^-$ state.	61
Table 3.8.	Frank-Condon factor for transition $(X^1\Sigma_g^+, \nu) - (d^3\Pi_u^-, \nu')$ with relevant vibrational number.	62
Table 3.9.	Vibrational energy of $X^1\Sigma_g^+$, $a^3\Sigma_g^+$ and $d^3\Pi_u^-$ state.	63
Table 3.10.	List of negative ion destruction processes included in the model and description.	64

Chapter 1. Introduction

1.1. Volume Production Negative Ion Source

Main application fields of a negative ion source are a high energy proton accelerator and a neutral beam injector (NBI) heating a plasma or driving a plasma current in a nuclear fusion reactor. In both applications, the negative ion is favored by its efficient charge neutralization.

Ionization following charge neutralization of the negative ion into a positive ion allows a double acceleration in a tandem accelerator with a single high voltage power supply. As shown in Figure 1.1, the negative ion injected into first tube is accelerated toward the positive high voltage electrode. Then, the negative ion is changed to the positive ion inside a charge stripper placed in the high voltage electrode. The positive ion departed from the positive voltage electrode is accelerated toward to a ground electrode. The negative ion is also utilized in a circular proton accelerator or a circular storage ring. Circular accelerators such as a cyclotron and a synchrotron are operating under magnetic field in a circular beam path. This magnetic field is incompatible to inject the proton inside the accelerators. Thus, if the negative ion is injected into the magnetic field and its electrons are stripped by a foil, direction of the stripped ion in the magnetic field changes behind the foil. Then the stripped proton joins the circular orbit, as depicted in Figure 1.2.

The negative ion source is important in the neutral beam injection system. NBI is one of the most efficient heating and current drive system in the present fusion research devices [1]. Under strong magnetic field of magnetically confined fusion plasmas, neutral particle rather than ion should be injected into the fusion plasma with sufficiently high energy to penetrate into the core of high density plasmas. For

example, ITER NBI is designed as 1 MeV beam energy. However, charge neutralization efficiency of the positive ion drops quickly as the beam energy increase. Based on the charge neutralization cross section of Figure 1.3, the negative ion source is favored for the ITER NBI system.

This useful negative ion source is categorized into two types according to the mechanism of negative ion production. The first one is a volume production mechanism which produces the negative ion by a dissociative electron attachment of a vibrationally excited molecule with a cold electron. Another production mechanism is a surface production occurred when a hydrogen atom or a hydrogen atomic ion impact the surface coated with low work function elements such as cesium. As for now, the surface production ion source is preferred in favor of its higher negative ion beam current. However, it suffers difficulties of cesium injection control and high voltage arcing at an acceleration electrode deposited by the cesium [2]. Thus, the volume production ion source has been studied for better efficiency hoping to be developed as a stable ion source.

To improve the performance of the volume production negative ion source, it is important that an understanding the mechanism of the volume production and related plasma physics, requiring plasma diagnostics and characterization of the ion source.

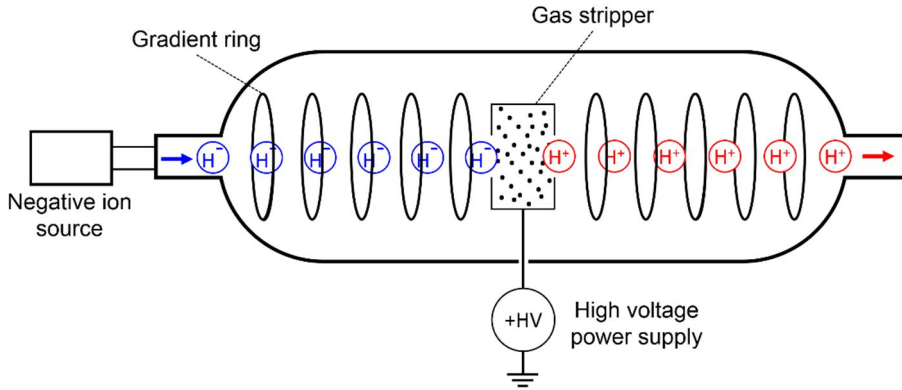


Figure 1.1. Schematic view of the tandem accelerator. The negative ion is injected into the accelerator and changed the polarity. Thus, negative ion is accelerated at left-hand-side of the gas stripper and the stripped positive ion is accelerated again with the single positive high voltage supply.

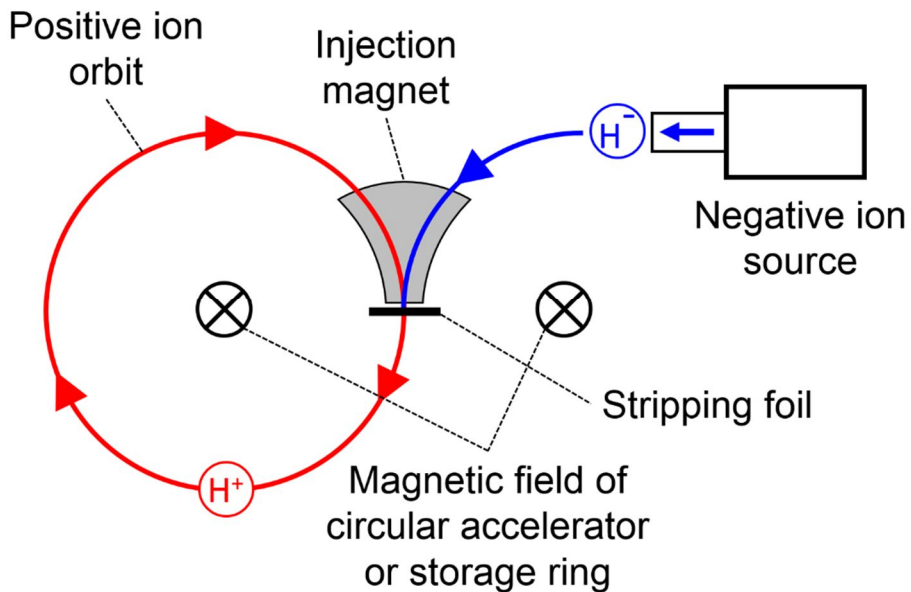


Figure 1.2. The orbit of the negative ion injected into the circular accelerator or storage ring.

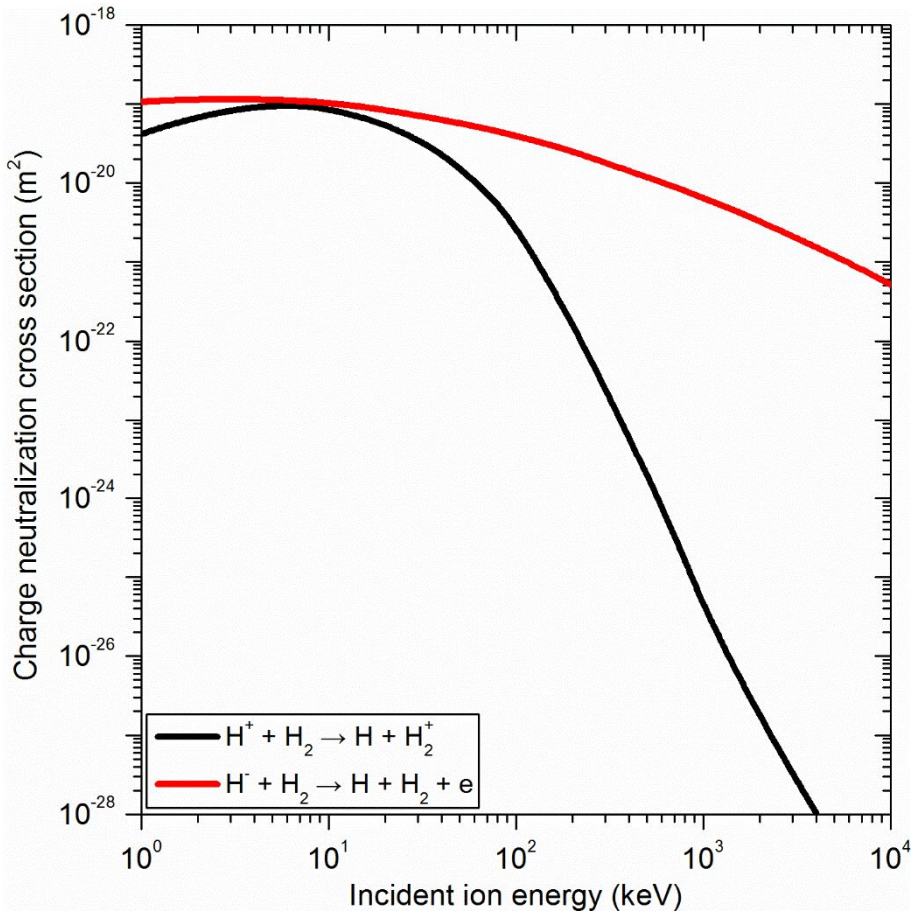


Figure 1.3. Cross section of the charge neutralization. The cross section of the positive ion decreases enormously faster than that of the negative ion above 10 keV [3].

1.1.1. Volume Production Mechanism of Hydrogen Negative Ion

Initial researches on the negative ion source were insufficient to understand on the negative ion production mechanism, and simply extracted negative ions directly from various plasmas generated in duoplasmatron [4, 5] and Penning ion source [6].

In 1977, Nicolpoulou *et al.* found a large difference between a measured negative ion density and an estimated value by the negative ion production

channels known at that time [7].



They knew the dissociative electron detachment (DA) process, but they didn't know the effect of the vibrational states of the hydrogen molecule on DA reaction. On the other hand, theoretical study on a relationship between the DA reaction and H_2^- resonant state had been conducted [8-10]. In 1979, it was theoretically [11] and experimentally [12] proven that the vibrationally excited state of the hydrogen molecule significantly enhances the cross section of the DA reaction. Thus, the study on the DA reaction became a major contribution to the volume production negative ion research.

In order to understand specifically the DA reaction, internal structure of the hydrogen molecule needs to be understood. The internal structure of H_2 is represented by electronic, vibrational and rotational states. The electronic state of H_2 is similar concept with a principal quantum number of the atom. The relevant electronic states of H_2 molecule and H_2^- ion are depicted in Figure 1.4. When the hydrogen molecule in $X^1\Sigma_g^+$ -state, which is an electronically ground state, is impacted by the electron, the electronic state is transited to other electronic state or forms the H_2^- ion. If the electron is captured and H_2^- is generated, it can be dissociated into the negative ion H^- and the atom. This reaction is called as the dissociative electron attachment (DA) reaction. Thus, if the hydrogen molecule is collided by the electron whose energy is lower than 20 eV, the hydrogen molecule has three different DA channels via $X^2\Sigma_u^+$, $B^2\Sigma_g^+$ and $C^3\Sigma_g^+$ -states of the H_2^- ion, respectively. Thus, there are three respective peaks in the DA cross section

corresponding to each channel. As shown in Figure 1.5, first peak of the cross section near 4 eV is the DA channel via $X^2\Sigma_u^+$ state. A magnitude of the first peak is about a tenth of that of the third peak near 14 eV. As mentioned in previous paragraph, this relatively low cross section leads the under-estimation of the equilibrium negative ion density, because the early researchers did not know about the effect of the vibrational state on the DA reaction.

The vibrational state is a sub-state of the electronic state, and the rotational state is the sub-state of the vibrational state. As depicted in Figure 1.4, the vibrationally excited states of the electronically ground state, $X^1\Sigma_g^+$, is overlapped with $X^2\Sigma_u^+$ states of H_2^- . Thus, the vibrationally excited molecule is relatively easy to form H_2^- ion. Consequently, the negative ion production is closely related with the vibrational state of H_2 . As depicted in Figure 1.6, the vibrationally resolved DA cross section increases according to the vibrational number of up to 9. The maximum value of the DA cross section of the vibrational state 9 is almost a hundred thousand times larger than that of the maximum value of the dissociative attachment shown in Figure 1.5. That is, the higher vibrational states of hydrogen molecule should be populated to enhance the negative ion production. Also, other notable feature of the DA reaction has decreasing cross section with a threshold energy. Therefore, the low energy electron is preferred to the DA reaction because the cross section is decreasing with energy and the threshold energy is reduced with higher vibrational numbers.

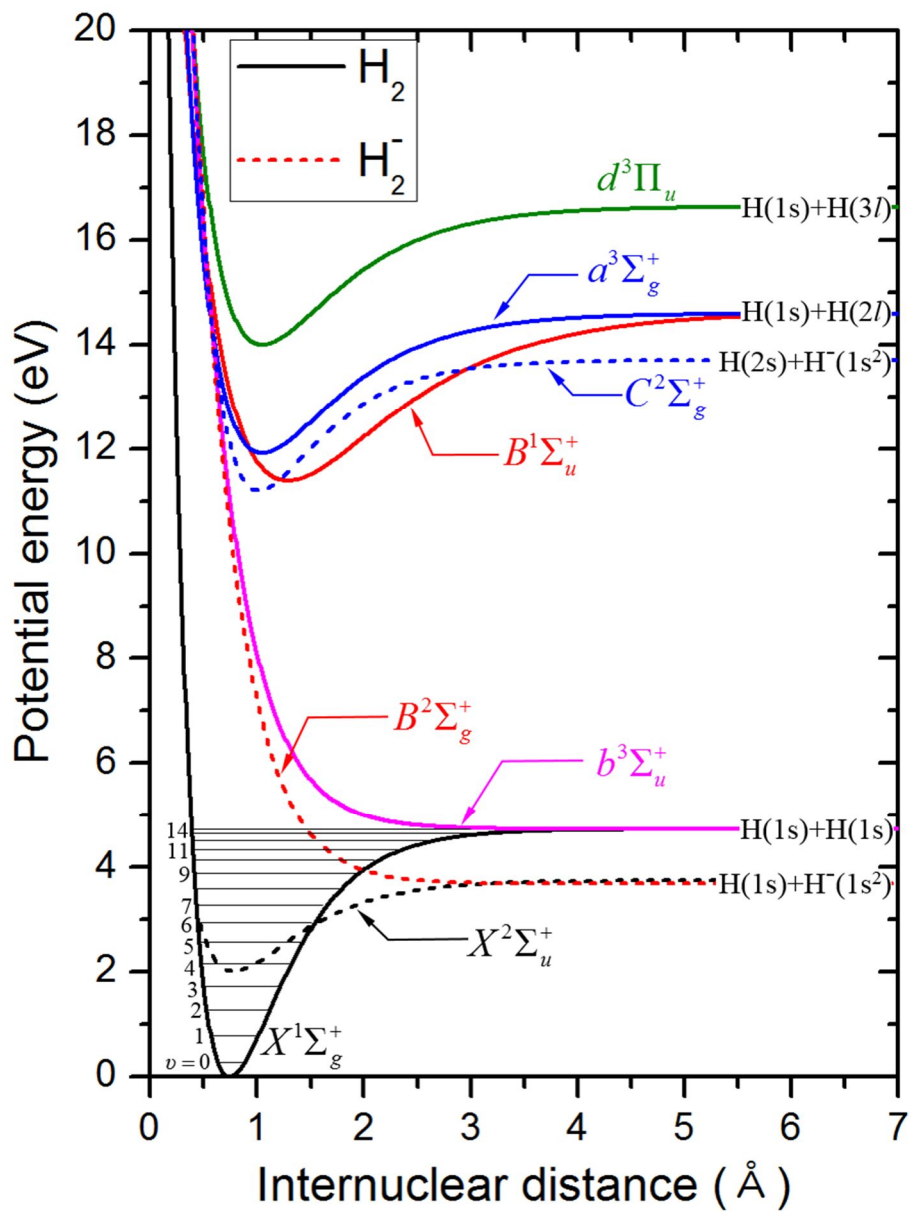


Figure 1.4. Potential energy curves for relevant electronic states of hydrogen molecule (solid lines) and H_2^- ion (dashed lines) [13]. Horizontal lines laid on $X^1\Sigma_g^+$ -state of hydrogen are the vibrational energy of each vibrational state.

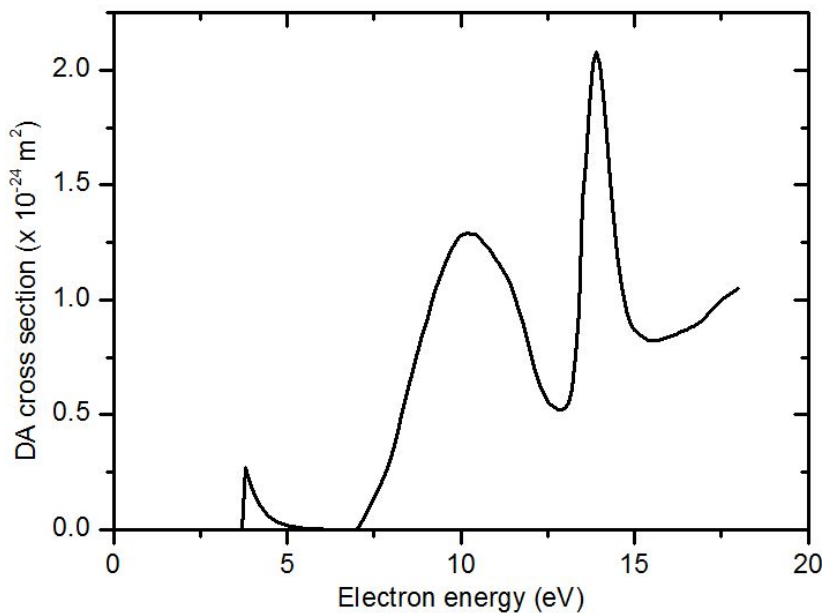


Figure 1.5. The cross section of the dissociative electron attachment. There are three peaks corresponding DA channels via $X^2\Sigma_u^+$, $B^2\Sigma_g^+$ and $C^3\Sigma_g^+$ -states of the H_2^- ion, respectively [14, 15].

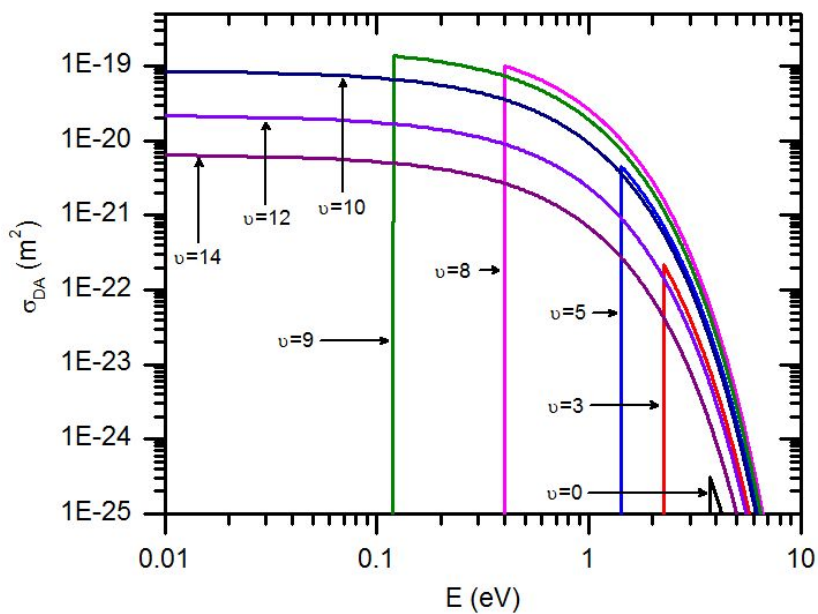


Figure 1.6. Cross section of the dissociative electron attachment for several vibrational states.

The vibrationally excited molecule is populated by two major channel. The first channel is vibrational excitation via H_2^- resonant state (e-V), and the other is excitation-radiative decay vibrational excitation (E-V). The reaction result as the vibrational excitation is the same in two reactions, but the excitation mechanism of two reactions are totally different.

The transition diagram of e-V reaction is depicted in Figure 1.7. The vibrational state is excited via $H_2^-(X^2\Sigma_u^+)$ state which is an unstable state overlapped with $H_2(X^1\Sigma_g^+)$ state. Thus, the e-V reaction can excite the H_2 with the low energy electron because a threshold energy of this reaction is low. However, this reaction is not proper to populate higher vibrational state.

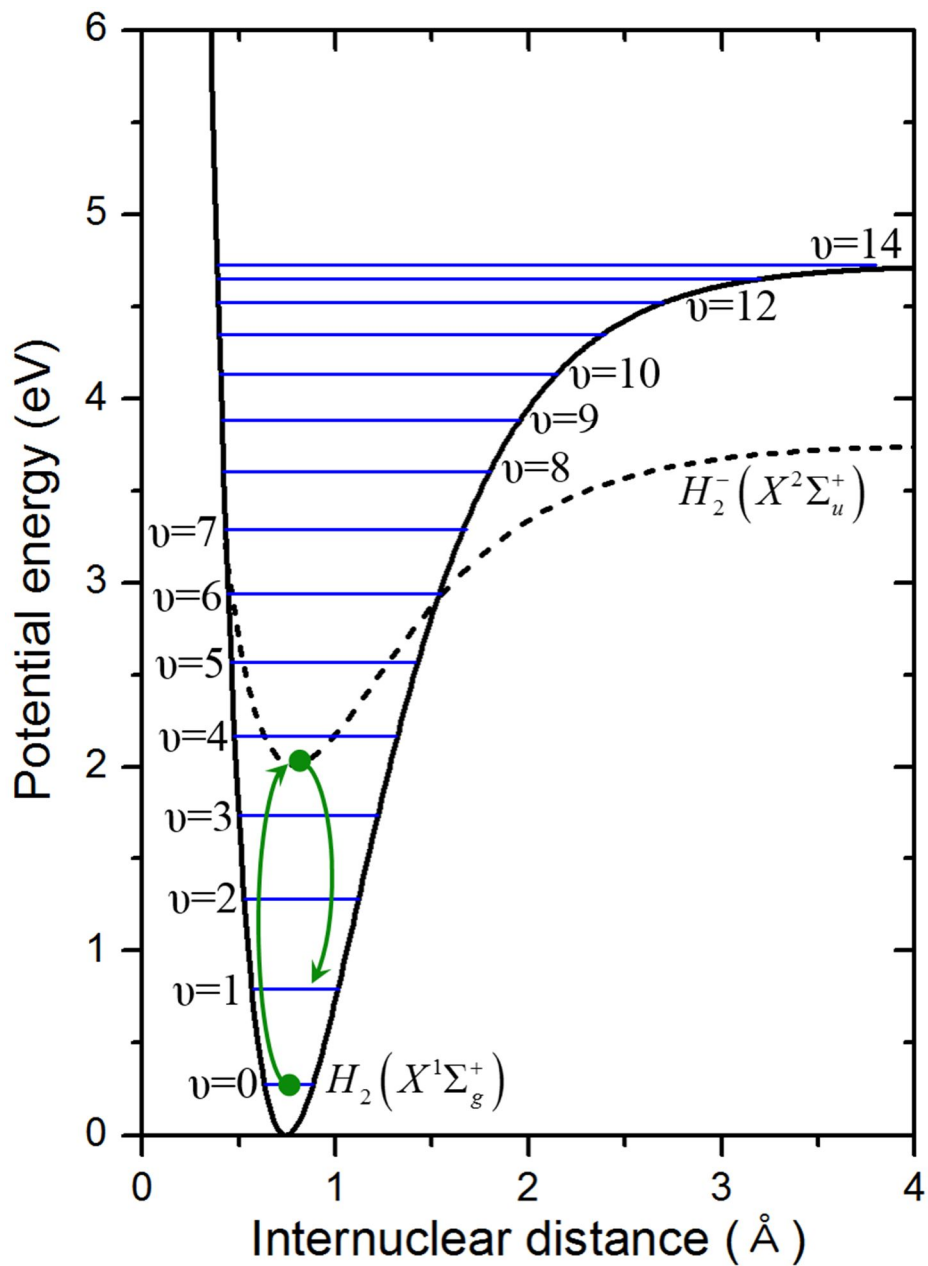


Figure 1.7. Transition diagram of e-V reaction. Potential curves of $H_2(X^1\Sigma_g^+)$ state (solid line) and $H_2^-(X^2\Sigma_u^+)$ state (dashed line). The vibrational states of $H_2(X^1\Sigma_g^+)$ are expressed as horizontal solid lines.

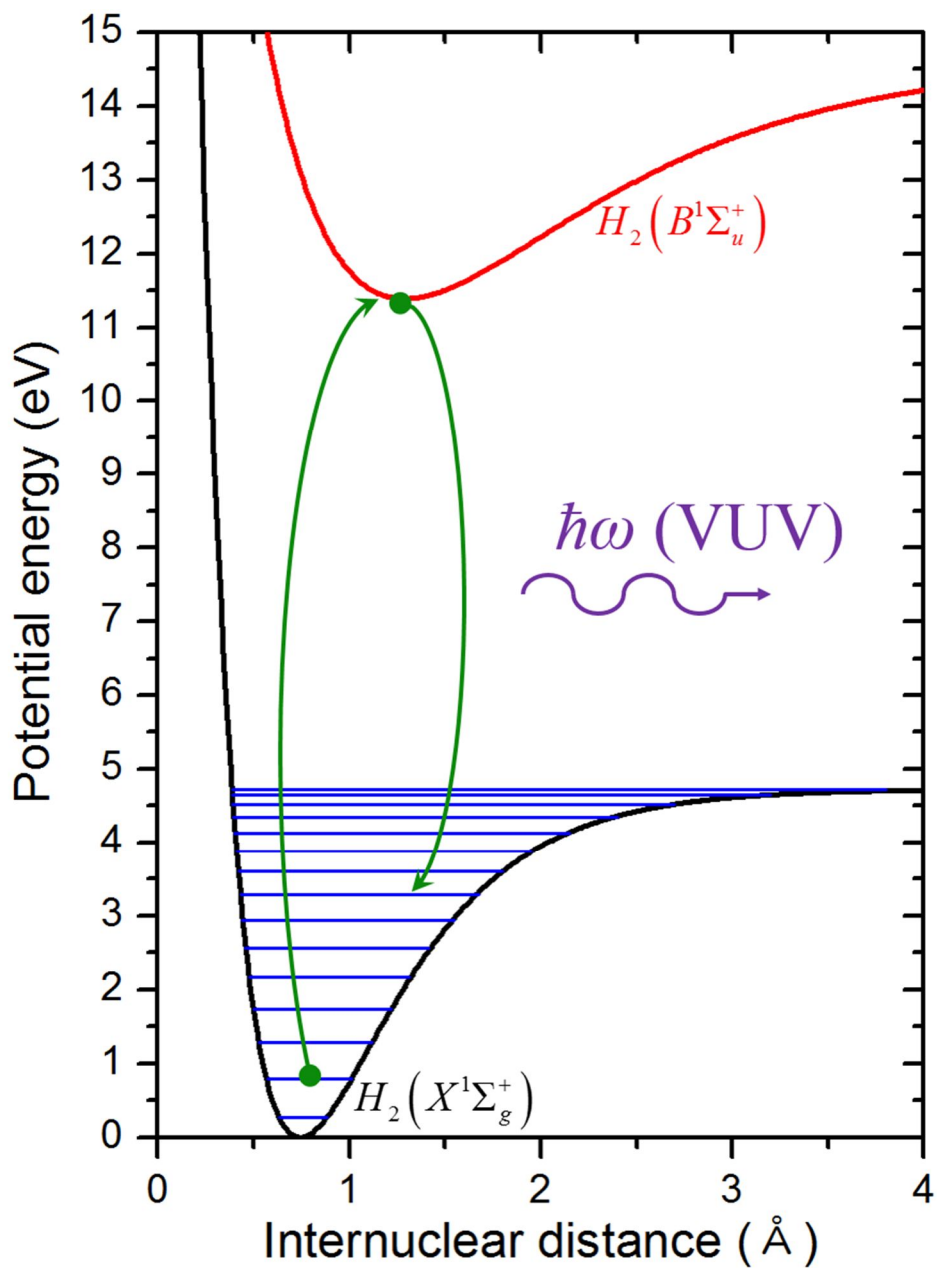


Figure 1.8. Transition diagram of E-V reaction. The electronic states of H_2 is excited to $H_2(B^1\Sigma_u^+)$ state and decays to electronic ground state with radiation. Both the vibrational excitation and de-excitation are available in the E-V reaction.

In contrast to the e-V reaction, the E-V reaction has a high threshold energy because the vibrational excitation is induced by the radiative decay of the electronically excited molecule, as shown in Figure 1.8. Though its higher threshold energy, the E-V reaction is efficient to populate higher vibrational state. For example, the reaction rate of the E-V reaction exciting 0 state to 7 state is 4 or 5 orders of magnitude higher than that of the e-V reaction with 10 eV electron, as shown in Figure 1.9.

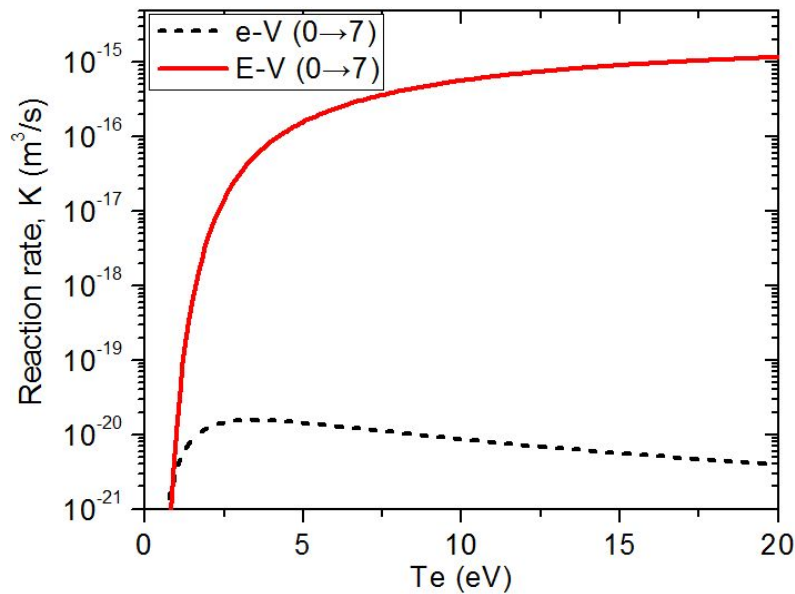


Figure 1.9. Reaction rates of the E-V and e-V reactions exciting vibrational number 0 to 7 state. The reaction rate of the E-V reaction is about 4 or 5 orders of magnitudes larger than that of the e-V reaction.

Thus, in order to increase the negative ion production, different energy electrons are required. High energy electrons are required to populate the vibrationally excited hydrogen molecule effectively and low energy electrons are required to produce negative ions via DA reactions in a single ion source.

According to this basic understanding, a negative ion source with a magnetic filter is chosen as a reference ion source in this study.

1.1.2. Magnetically Filtered Negative Ion Source

A key feature of the magnetically filtered negative ion source is dividing the source into two regions, so called a driver region and an extraction region, as schematically depicted in Figure 1.10. The plasma is formed at the driver region with an RF antenna or a powered electrode. The driver region generates vibrationally excited molecules with high energy electrons. Electrons generated at the driver region diffuse into the extraction region across the magnetic filter field. During the diffusion, the high energy electrons are lost to the chamber wall by their high mobility along the field lines. Only low energy electrons arrive and remain at the extraction region. Thus, the electron energy at the extraction region can be sustained as low as preferred to the DA reaction. Therefore, the magnetically filtered ion source can provide two different energy groups of electrons separately and produce hydrogen negative ions effectively.

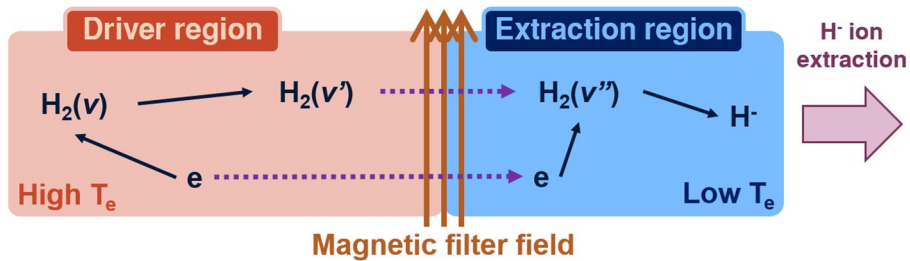


Figure 1.10. Schematic figure of magnetically filtered negative ion source. The vibrationally excited molecule by the e-V and E-V reaction in the driver region is moved to the extraction region. The negative ion is produced by DA reaction in the extraction region.

1.2. Motivation and Scope of Study

In order to understand and improve the volume negative ion source, various global models are developed as listed in Table 1.1. Measured plasma parameters such as electron temperature, electron density and vibrationally excited molecules are important to characterize the negative ion source more accurately with the global model. The properties of the plasma electron can be easily measured by an electrostatic method such as the Langmuir probe. However, the vibrationally excited molecule is difficult to be measured, in spite of its significance in the negative ion source.

There are 15 vibrational states from 0 to 14 in the electronic ground state, $X^1\Sigma_g^+$, of the hydrogen molecule. The partition function of the hydrogen molecule occupying the respective vibrational states is called as a vibrational distribution function (VDF). The VDF depends on neutral gas pressure, temperature and species as well as electron temperature [16]. Especially, higher states of the VDF are largely deviated from the Boltzmann distribution defined by the lower vibrational states. Thus, it is important to measure or estimate accurately the higher states which are in non-Boltzmann distribution and key elements in the dissociative electron attachment. The VDF measurement on the negative ion source was attempted utilizing the coherent anti-Stokes Raman spectroscopy (CARS) for the first time in 1985 [17]. Péalat *et al.* measured the VDF of first 4 states. In 1989, Eenshuistra found the clue of the non-Boltzmann VDF [18]. The vibrational numbers (v) of up to 5 were measured by the resonantly enhanced multi-photon ionization (REMPI), but this experiment was *ex-situ* measurement. *In-situ* measurement was conducted by Wagner *et al.* who utilized the vacuum ultra violet (VUV) laser absorption spectroscopy in 1998 [19]. In 2000, the VUV laser aided measurement such as VUV laser induced fluorescence (LIF) was used to diagnose

the VDFs from 3 to 13 [20], i.e., most states of the VDF. However, the spectrum of the LIF was overlapped with the plasma radiation. Thus, Mosbach *et al.* measured the VDF of only an afterglow in a pulsed negative ion source. Meanwhile, Fantz *et al.* developed a passive optical emission spectroscopy (OES) for the VDF diagnostics [21]. This method was easy and required just a simple optical instrument. However, this OES was only suitable for the lower vibrational states measurement [22].

Therefore, there is no practical solution to diagnose the entire VDF of the continuously operating negative ion source as summarized in Table 1.2. Instead, numerical models have been widely developed to complement the limitation of the VDF diagnostics. Zero-dimensional global models [23-25] can be utilized in this analysis. However, 0-D global model is limited when it is applied to the magnetically filtered negative ion source because the VDF is mostly generated at the driver region and then transported into the extraction region. Although multi-dimensional models for ITER NBI have been developed [26-29], they are focusing to explain phenomena related only with the charged particles such as plasma asymmetry, negative ion transport and extraction, plasma potential distribution and the magnetic filter effect, etc. So, more accurate numerical model accounting for the kinetics on the VDF is needed for the negative ion source with magnetic filter.

Table 1.1. Numerical models for the negative ion source.

Domain	Institute	Model type	Remark
0 - D	Univ. Duisburg-Essen [23], Univ. of Bari [24], SNU [25]	Global or particle balance	Most models are developed as 0-D.
1 - D	Sofia [26]	Fluid	Only charged particle species were included.
2 - D	LAPLACE [27, 28]	Hybrid (Monte Carlo + Fluid)	Most advanced model. Simulation is failed under the high magnetic field strength.
3 - D	Sofia Univ. + IPP [29]	Fluid	Only charged particle species were included.

Table 1.2. Summary of VDF diagnostics

	CARS [17]	REMPI [18]	VUV AS [19]	VUV LIF [20]	OES [21]
Observable vibrational state	$v < 3$	$v < 6$	$v < 6$	$3 < v < 14$	$v < 4$
Accuracy	Good	Good	Good	Good	Low
Experiment difficulty	High	High	High	High	Low
Instruments	2 Laser + PMT	UV laser + TOF MS	VUV laser + VUV spectrograph	VUV laser + VUV spectrograph	Spectrograph
Remark		Ex-situ		Pulse mode	

Therefore, this study tries to by develop an appropriate numerical model which can complement the limitation of the VDF diagnostics, and simulate the populating and the transport of the VDF at the magnetically filtered negative ion source geometry. Also, its results are analyzed by checking key factors determining the population, transport and a variation of the VDF. The numerical model is constructed based on the measured plasma parameters and verified by the optical diagnostics for both the VDF and the negative ion density measurement. Thus, utilizing the numerical model and the spectroscopic diagnostics, this work studies characteristics of the negative ion source based on the physics related with the VDF.

This dissertation consists of following 5 chapters. Chapter 2 is devoted to describe the RF driven negative ion source and the established diagnostics. Also, the fundamental physics related with the diagnostics is introduced. The diagnostic results for the electron temperature, density, and gas temperature are presented in this chapter because they are utilized as input parameters in the numerical study. A structure and feature of the 0-D VDF model developed in this study are introduced in chapter 3. Through a comparison with the Fulcher- α spectrum measurement, the VDF determined by the 0-D model will be verified. Also, it is described that the limitation of the model occurred when the 0-D model is applied to the magnetically filtered ion source geometry. In chapter 4, 1-D VDF transport model developed to overcome the limitation of the 0-D model is introduced. Also, it is described that the main result of the improved 1-D model which shows good agreement with the negative ion diagnostics and the relaxation of the VDF during transport. Based on the numerical and experimental study, the kinetics on the vibrationally excited hydrogen molecule is discussed in chapter 5. Chapter 6 address summary and conclusion of this research.

Chapter 2. RF Driven Negative Ion Source and Its Diagnostics

2.1. RF Driven Negative Ion Source

2.1.1. Overall Structure of the Negative Ion Source

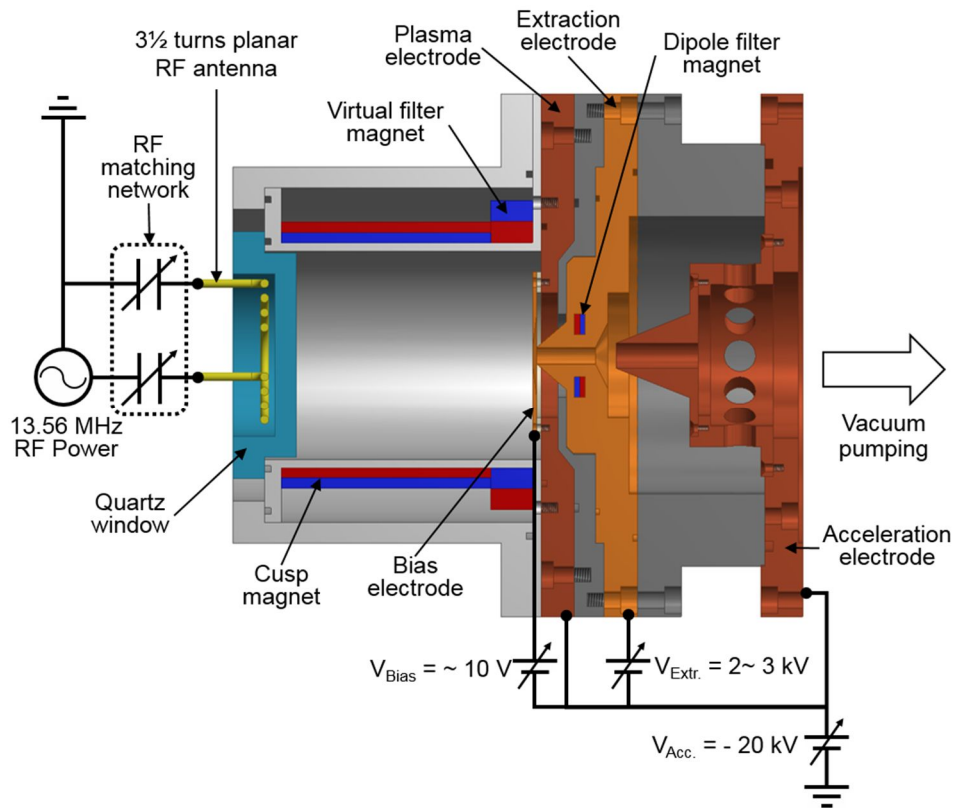


Figure 2.1. Cross-sectional view of the negative ion source, arrangement of beam extraction and acceleration electrodes and electric circuit.

The negative ion source developed at Seoul National University is schematically

depicted in Figure 2.1. The cylindrical chamber is made of stainless steel. At the left end of the chamber, a dielectric window made of quartz is located to apply RF power through a $3\frac{1}{2}$ -turn external antenna. A beam extraction hole is located at the opposite end. A low flow conductance of the extraction hole keeps a differential vacuum pumping condition. Fourteen samarium-cobalt (SmCo) rectangular magnets surround the chamber and generate the azimuthal cusp field for better plasma confinement. Near the extraction hole, three pairs of neodymium (NdFeB) virtual filter magnets are installed as shown in Figure 2.1. In order to remove co-extracted electron as well as enhance the filter field, a pair of samarium cobalt (SmCo) magnets is located inside the extraction electrode and they are called as dipole filter magnets. Those filter magnets sustain the low electron temperature at the extraction region. Detail of the magnetic field is introduced in section 2.1.2.

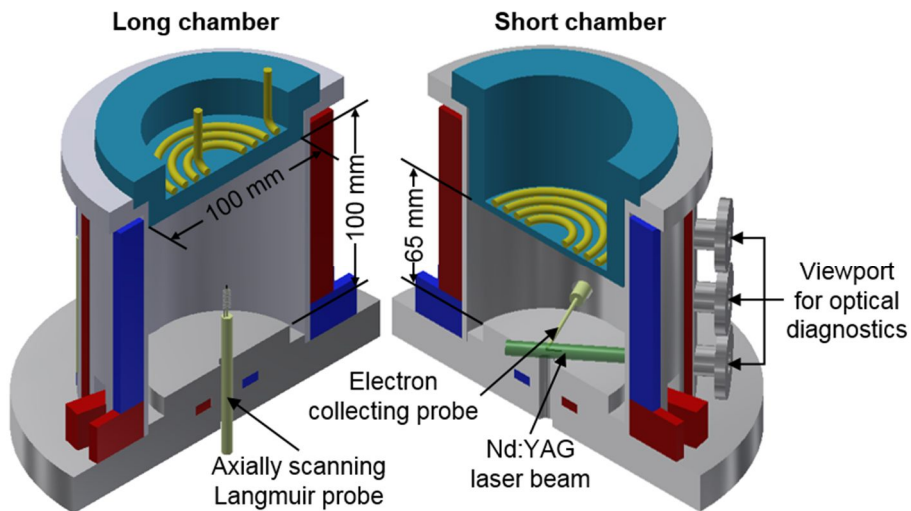


Figure 2.2. Cross-sectional view of the ion source with different chamber length and the diagnostic tools or set-up.

Dimension of the cylindrical plasma chamber is 10 cm in both diameter and length. However, the length of the ion source can be adjusted by replacing the vacuum window with a different depth, as shown in Figure 2.2 오류! 참조 원본을

찾을 수 없습니다.. Thus, two different chamber lengths (10 cm and 6.5 cm) are employed in this study. The 10 cm length chamber and the 6.5 cm length chamber are described as a long chamber and a short chamber, respectively.

The base pressure is about 4×10^{-4} Pa. The pressure of the ion source can be operated in range of 0.4 Pa to 4 Pa. There is no significant difference in the operating pressure according to the chamber length with the same gas flow rate.

The RF power of up to 1 kW is delivered to the plasma through a planar antenna with L-type RF matching network as shown in Figure 2.1. Negative ion beam is extracted from a negatively biased plasma electrode with 3 electrode extraction system as shown in Figure 2.1. The plasma electrode is negatively biased to allow easier negative ion extraction. The voltage of the bias electrode is controlled to generate attractive potential profile to the negative ion extraction by setting the voltage as similar or slightly higher than the plasma potential. The extraction electrode is positively biased to extract the negative ions from the plasma. Also, the magnetic field generated by the dipole magnet inside the extraction electrode guides and eliminates the co-extracted electrons to the extraction electrode. The extraction electrode voltage of typically 2 - 3 kV is optimized to minimize the current entering to the extraction electrode with good beam optics. Finally, the extracted negative ion beam is accelerated to the acceleration electrode. The acceleration electrode is grounded in this system. As mentioned, the beam energy is controlled by the plasma electrode potential. The maximum beam current of the negative ion source of 1.85 mA is achieved with the beam energy of 15 keV [30].

Three diagnostics are established for the negative ion source. They are a Langmuir probe for the plasma parameter measurements, a laser photo-detachment diagnostic system for the negative ion density measurement and an optical diagnostics for the VDF measurement, as presented in Figure 2.2. More details on the diagnostics will be described in following sections.

2.1.2. Magnetic Field Structure in Negative Ion Source

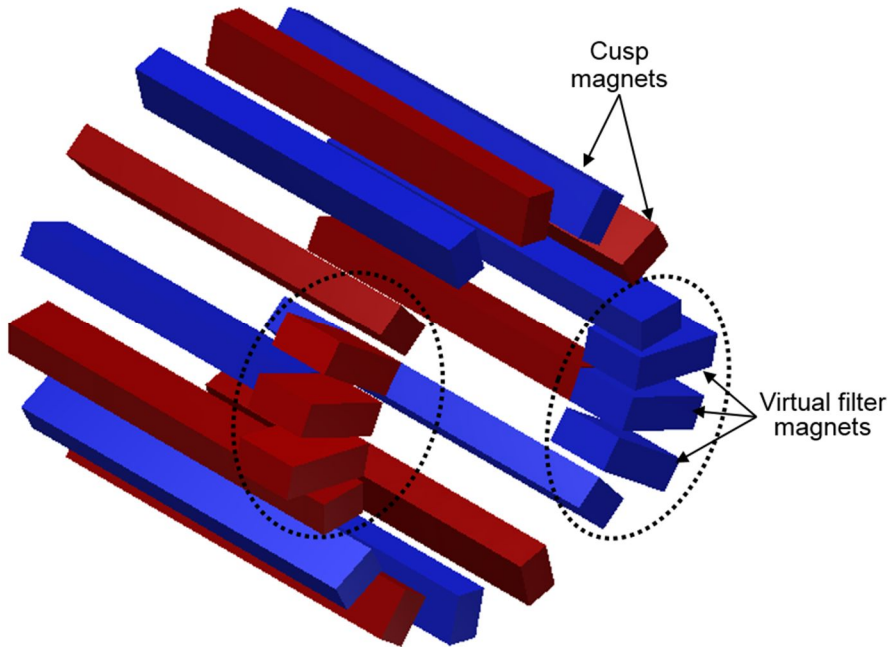


Figure 2.3. Arrangement of cusp field magnets and virtual filter magnets.

As written in previous section, there are two kinds of magnetic fields in the negative ion source. The arrangement of the magnets is depicted in Figure 2.3. The first is cusp field by the SmCo magnet surrounding the chamber. The dimension of the respective cusp magnet is 1 cm in both width and depth, and 10 cm in height. The magnetic field strength at the surface of the magnet is stronger than 0.3 Tesla. The strength of the cusp field is about 0.2 Tesla near the chamber wall and almost zero on the axis of the ion source, as shown in Figure 2.4. The second one is the filter field. There are three pairs of virtual filter magnets. Two pairs of the magnets located between the cusp magnets and their polarities are same with adjacent cusp magnets. Other pair of the magnets located between two pairs of the virtual filter magnet mentioned in the previous sentences. Thus, they are shorter than other cusp magnet by the thickness of the virtual filter magnet that the cusp magnets located

on same column with the central virtual filter magnets. Therefore, the filter field is generated by five consecutive magnets with the same polarity including virtual filter magnets and the cusp magnets, as shown inside the elliptic dashed lines in Figure 2.3. The dimension of the respective virtual filter magnet is 1 cm in width and 2 cm in both height and depth. Also, there is 1 pair of the dipole magnet inside the extraction electrode. The dipole magnet is a thin rectangular magnet. The width and height are both 1 cm, and the thickness is 0.5 cm. The filter field strength is depicted in Figure 2.5 and Figure 2.6. The field strength near the wall is strongly affected by the cusp field as shown in Figure 2.5. Thus, the pure filter field region generated by the filter magnets looks like 30 – 40 mm in length and width. Also, the filter field is strongest at extraction hole and decays exponentially farther away from the extraction hole, as depicted in Figure 2.6. The magnetic field are simulated by COMSOL Multiphysics®, 오류! 참조 원본을 찾을 수 없습니다.and simulation result is well matched with measured filter strength, as shown in Figure 2.6.

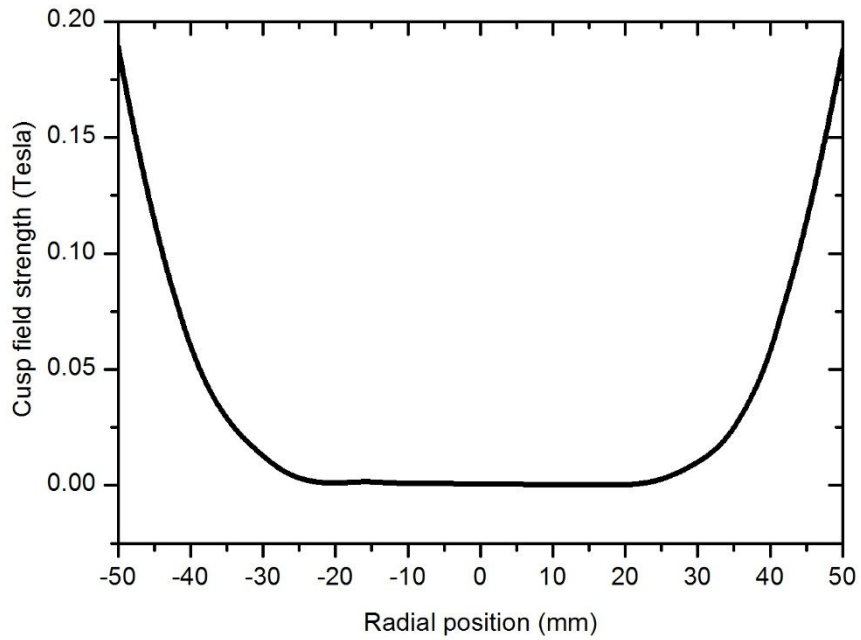


Figure 2.4. Simulation result for cusp field strength at the driver region.

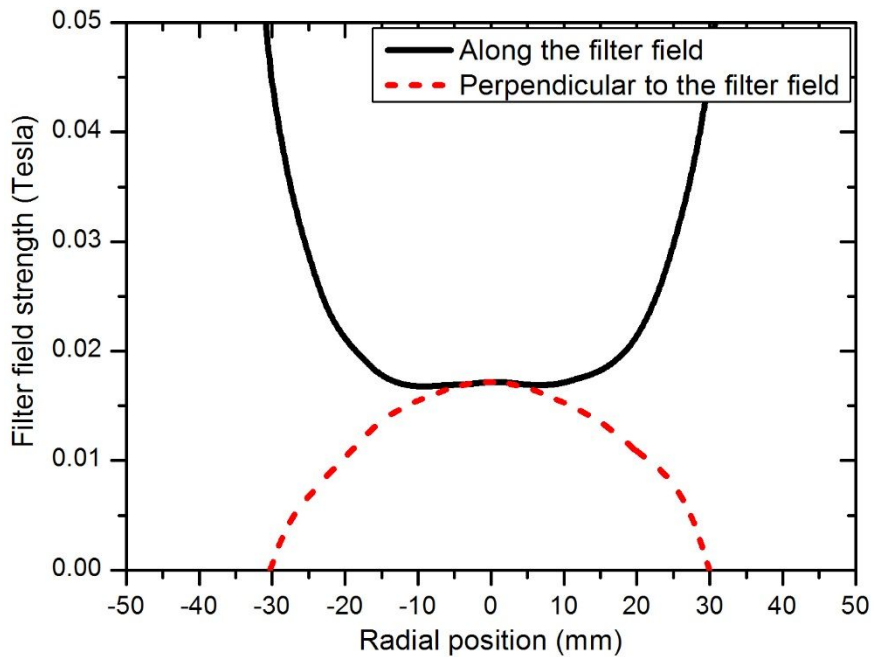


Figure 2.5. Filter field strength along the filter field direction (solid line) and perpendicular direction to the filter field line (dashed line).

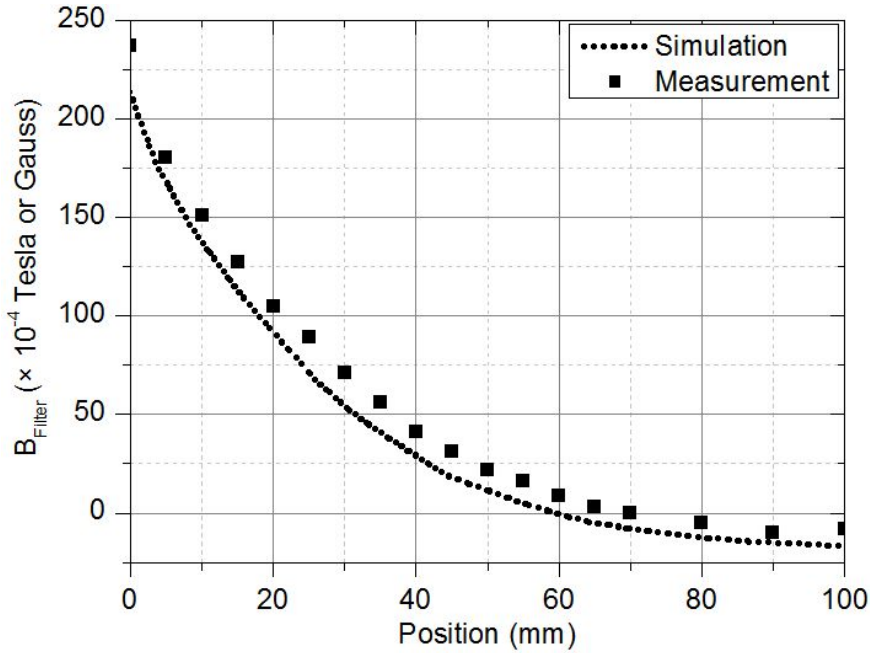


Figure 2.6. Comparison of the simulation result and the measured filter field strength along the axis of the ion source.

2.2. Langmuir Probe and Profile Measurement of Plasma Parameters

2.2.1. Axially- Scanning Langmuir Probe

The Langmuir probe is primary diagnostic tool for the plasma parameters such as electron temperature, density, and plasma potential. In this work, RF compensated cylindrical Langmuir probe is employed. A diagram of the RF compensated Langmuir probe is depicted in Figure 2.7. The I-V curve of the RF driven plasma is distorted by RF pickup. In RF plasmas, the plasma potential can fluctuate according to RF potential. The voltage of I-V curve is a voltage difference

between the biased voltage of the probe tip and the plasma potential. Thus, this voltage difference fluctuates during the probe tip collects the current. Then, the current is recorded as an average of the current measured on the fluctuating voltage. Therefore, RF choke circuit and additional electrode should be inserted to compensate RF oscillation of the plasma potential. The RF choke is fabricated to have high impedance to RF and makes that the biased voltage of the probe is synchronized to RF potential. Also, a reference electrode is inserted as parallel to the probe sheath impedance. Thus, the reference electrode keeps a total impedance of the probe tip is lower than the choke impedance and the RF choke effectively functions. Details of the RF compensation is well described in references [31, 32].

The probe tip is made of a tungsten wire whose diameter is 0.3 mm and length is 1 mm. The reference electrode is made of the same diameter tungsten wire. The reference electrode is manufactured as a coil shape with 10 windings and about 5 mm in coil diameter. Also, Debye length of the negative ion source is typically ~ 0.05 mm. Thus, the charged particle collecting area of the probe can be assumed as same with the probe tip area. In order to analyze I-V curve of the Langmuir probe, the collision-less sheath model is applied.

The Langmuir probe measurement was conducted on the axis of the ion source. The probe can be moved from the bottom plate to in front of the vacuum window. The diagnostics was conducted at every 5 mm along the axis. To obtain I-V curve with low noise, the probe current was averaged of 50 cycles of the probe voltage sweeping.

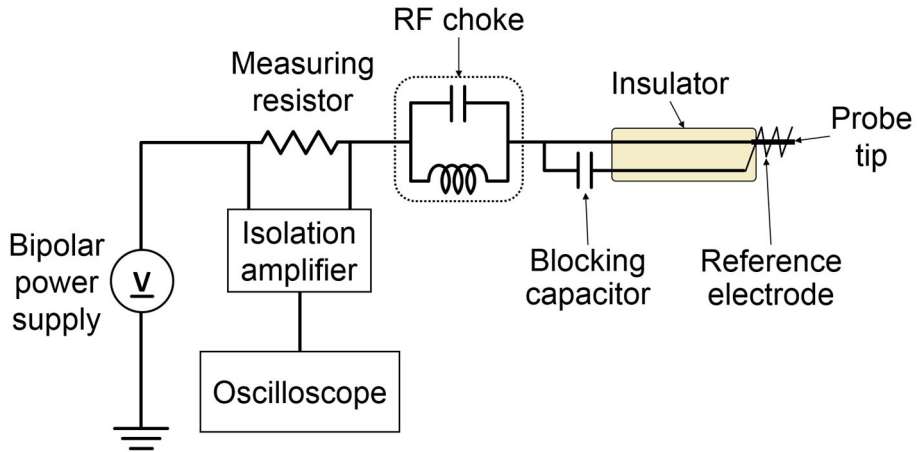


Figure 2.7. Diagram of the Langmuir probe and the RF compensation circuit.

Also, to improve a consistency of the I-V curve analysis and reduce a time to analyze the I-V curve, a computer-based analysis is introduced. The analysis is carried out by assuming Maxwellian electron energy distribution function (EEDF) with the following procedure.

1. Calculate dI/dV and find the plasma potential (V_{pl}) from the maximum of dI/dV .
2. Fit ion current linearly near the ion saturation region.
3. Subtract the linearly fitted ion current from the measured current and set it as the electron current (I_e).
4. Obtain the electron temperature as an average of $qI_e/(dI_e/dV)$.
5. Determine the electron density from the electron temperature and the electron saturation current (I_{es}) defined as the electron current at the plasma potential.

The equations determining the electron temperature and density are expressed as follows

$$I_e = I_{es} \exp\left[\frac{q(V - V_{pl})}{kT_e}\right] \quad (2.1)$$

$$\frac{qI_e}{dI_e/dV} = \frac{qI_{es} \exp\left[\frac{q(V - V_{pl})}{kT_e}\right]}{I_{es} \frac{q}{kT_e} \exp\left[\frac{q(V - V_{pl})}{kT_e}\right]} = kT_e \quad (2.2)$$

$$n_e = \frac{I_{es}}{qA I_{es} \sqrt{\frac{kT_e}{2\pi m_e}}} \quad (2.3)$$

where V is the probe voltage, q is unit charge of the electron, and A is the area of the probe tip. Also, electron energy distribution function (EEDF) can be determined from the second derivative of the electron current. The EEDF, g_e , is expressed as

$$g_e(V_e) = \frac{2m_e}{q^2 A} \sqrt{\frac{2qV_e}{m_e}} \frac{d^2 I_e}{dV_e^2} \quad (2.4)$$

where $V_e = V_{pl} - V$. Also, the Maxwellian and Druyvesteyn EEDF corresponding to the obtained electron temperature are provided for comparison.

An example of the analysis is shown in Figure 2.8.

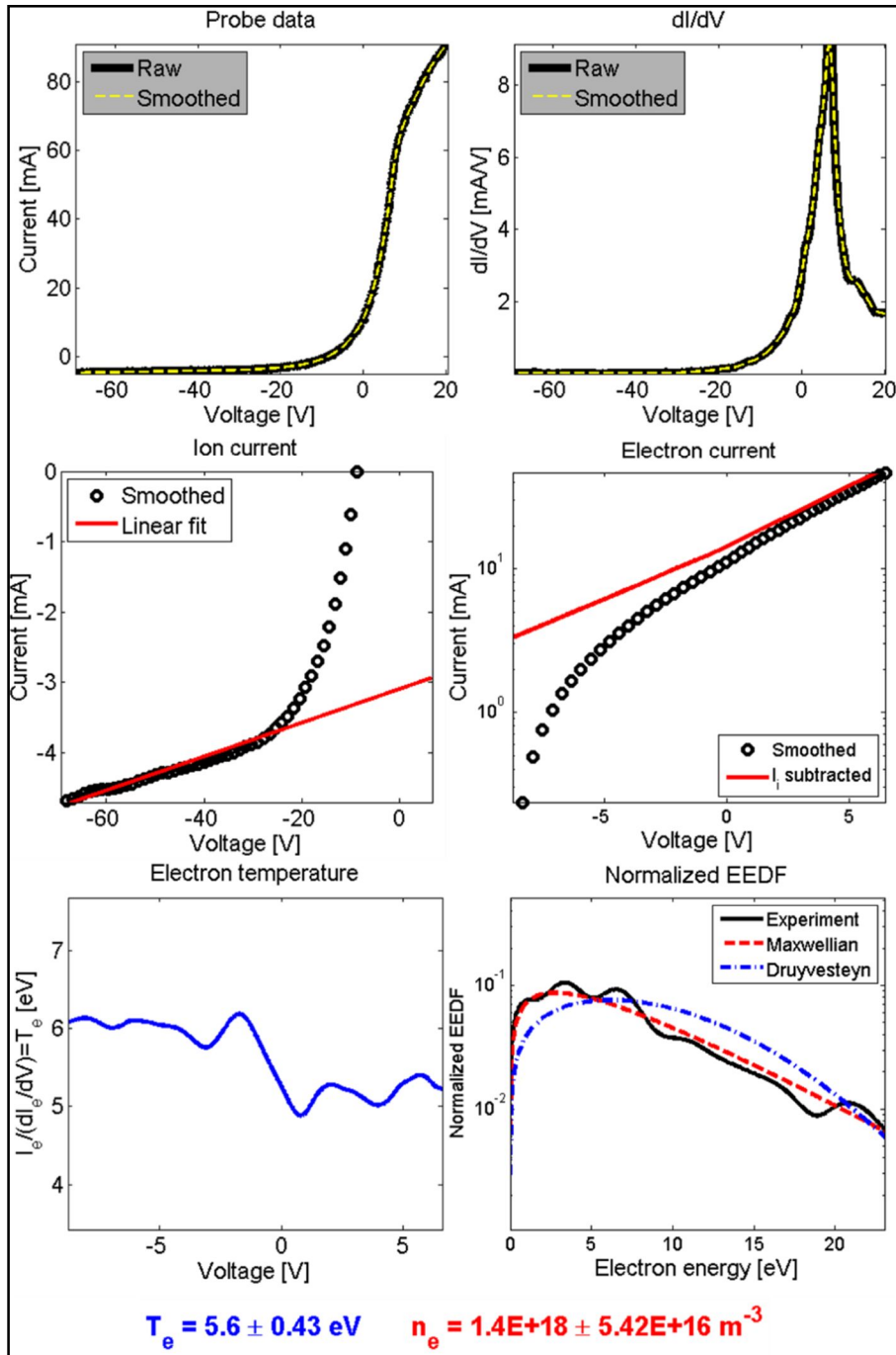


Figure 2.8. Example of I-V curve analysis results obtained from computer based analysis code

2.2.2. Plasma Parameters in Negative Ion Source

The electron temperature and density of the long and short chamber are depicted in Figure 2.9 and Figure 2.10, respectively.

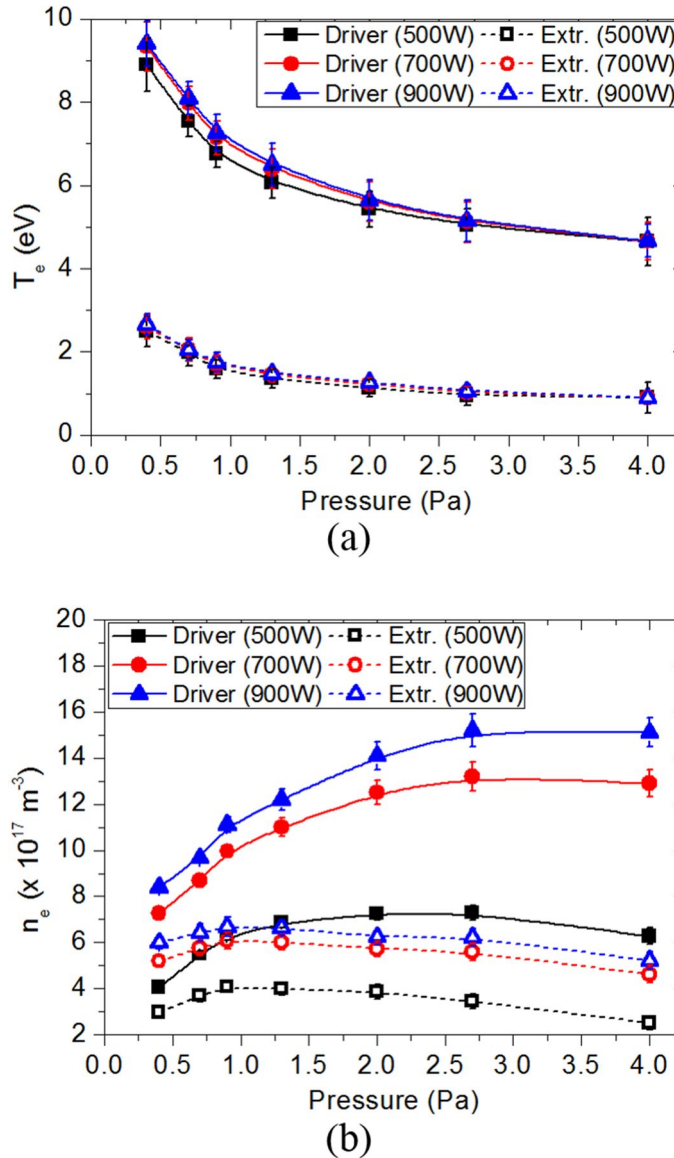
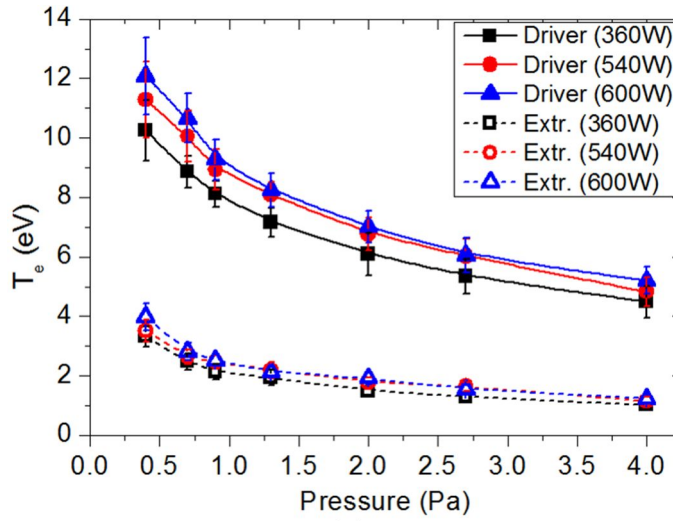
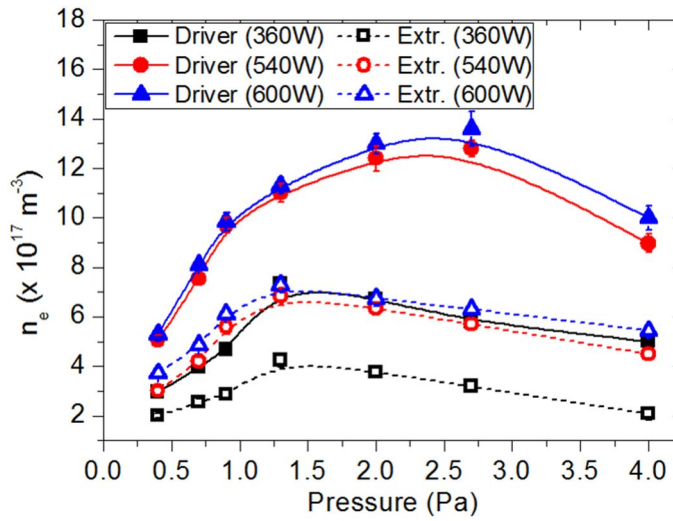


Figure 2.9. (a) Electron temperature and (b) density of the long chamber according to the operation pressure and RF power.



(a)



(b)

Figure 2.10. (a) Electron temperature and (b) density of the short chamber according to the operation pressure and RF power.

The electron temperature shows typical dependency on pressure, chamber length and RF power. The electron temperature decreases as pressure and chamber length increase, and interestingly it is almost independent on RF power. Also, the electron density strongly depends on RF power. The electron density increases as the

increase of pressure. The electron temperature at the extraction region is a fifth ~ a third of those at the driver region. For the electron density, there is a factor of 2 or 3 difference.

2.2.3. Profile of Plasma Parameters

Typical profiles of the electron temperature and density are measured for both long- and short-chamber ion sources as presented in Figure 2.11. The profiles of the plasma parameters are an important issue in the negative ion source [2, 33]. There were a lot of efforts to explain the diffusion of plasmas across the magnetic filter field [29, 34-36]. According to the previous work, the plasma transport in the magnetic filter was found to be complicate and determined by various phenomena.

To explain the plasma diffusion in the magnetic filter, the gyro frequency and the collision frequency of charged particles should be known for the determination of plasma magnetization. Gyro frequencies of electron and ion are 1.76 GHz and ~ 1 MHz, respectively. The electron-neutral collision frequency and the ion-neutral collision frequency are 10 ~ 40 MHz and ~ 1 MHz, respectively, at the ion source operation condition in this work. Thus, electron is treated as strongly magnetized and ion is treated as un-magnetized in following description.

Electrons are heated in a skin depth where the RF power is deposited. They diffuse to the extraction region. However, their diffusion coefficient across the magnetic field suddenly decrease since they are strongly magnetized near the extraction region. Though electron diffusion is restricted, ions can diffuse across the field line. Thus, the ambipolar field is generated, and then ions and electrons diffuse together restrained by the ambipolar field. If the magnetic field is infinitely long, the ambipolar diffusion coefficient is mathematically expressed as

$$D_{\perp a} = D_{\perp e} \left(1 + \frac{T_i}{T_e} \right) \quad (2.5)$$

where $D_{\perp e}$ is the electron diffusion coefficient perpendicular to the magnetic field. The perpendicular diffusion coefficient of the electron and the ion in the magnetic field is

$$D_{\perp s} = \frac{D_s}{1 + (\omega_s / \nu_s)^2}, \quad (s = e \text{ or } i) \quad (2.6)$$

where ω_s is the gyro frequency and ν_s is neutral the collision frequency of species s . The diffusion coefficient D_s is

$$D_s = \frac{k_B T_s}{m_s \nu_s}. \quad (2.7)$$

Thus, the perpendicular diffusion coefficient of the plasma can be approximated as $D_{\perp a} \approx D_{\perp e}$, when the electron temperature is sufficiently larger than the ion temperature. In this case, the diffusion across the magnetic field is significantly restricted because the diffusion coefficient is almost same with the magnetized electron diffusion coefficient. However, the filter field has a finite structure. Thus, magnetized electrons can escape the plasma along the field line to the wall. Under this circumstance, the electron flows along the field line and ion flows across the field line. That is, the flux congruence assumption ($\Gamma_e = \Gamma_i$) is broken and net electric current is generated at the chamber wall, as schematically presented in Figure 2.12. This phenomenon is called as ‘short circuit effect’ [34]. By this effect, the perpendicular diffusion coefficient is enhanced as follow [32]

$$D_{\perp a} = D_{\perp i} \frac{T_e}{T_i} \quad (2.8)$$

Thus, though the electron is strongly magnetized, the electron can diffuse across the filter field. After the electron diffuses into the magnetic filter region, the fast electrons whose temperature is higher than the plasma potential rapidly escape to the wall by its high mobility along the field line. The cold electron is confined by the magnetic field and the sheath potential. Finally, the cold electrons remain in the magnetic filter region, showing enhanced electron density with lower electron temperature in front of the extraction hole as shown in Figure 2.11.

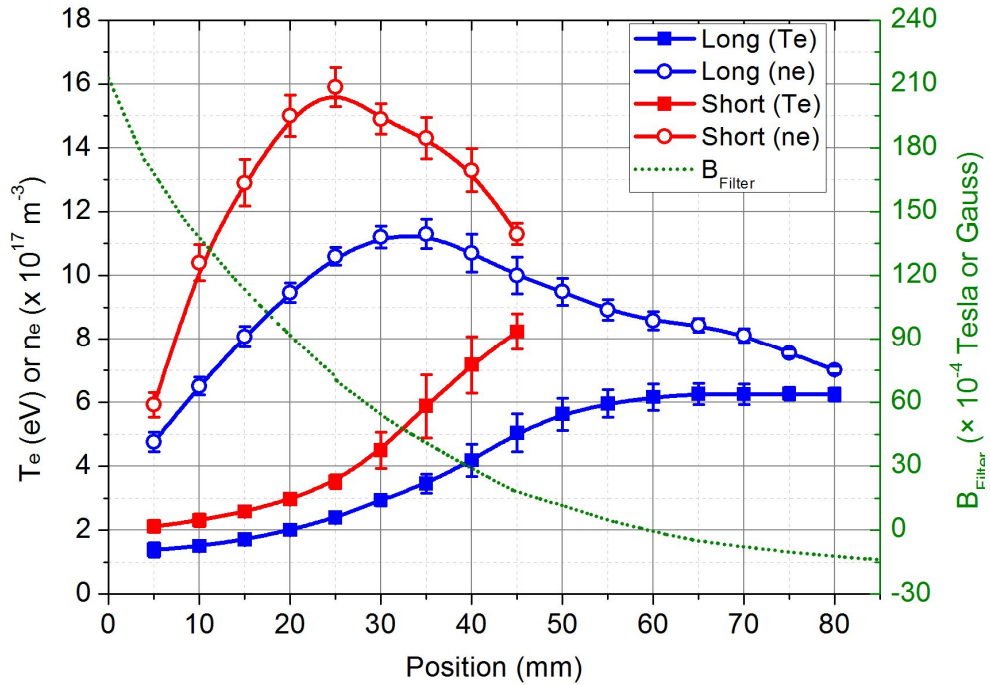


Figure 2.11. Typical plasma parameter profiles in negative ion source with different chamber length and the filter field strength.

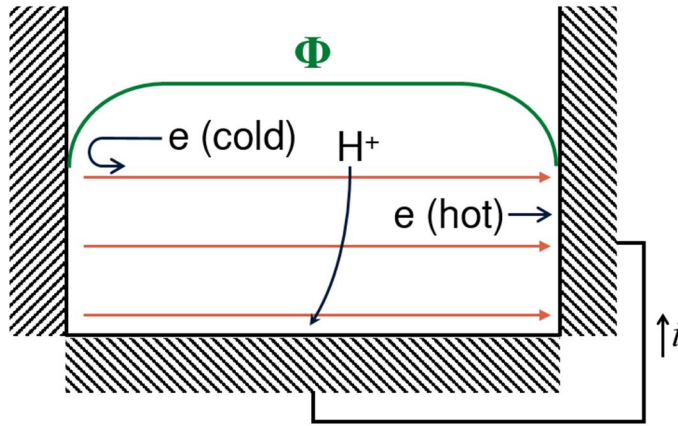


Figure 2.12. Diffusion of the electron and ion in the filter magnetic field. The electron flows along the field line and the ions flows across the field line. Thus, net current is generated at the wall.

2.3. Laser Photo-Detachment for the Negative Ion Density Measurement

Laser photo-detachment for the negative ion density determination was developed by Bacal *et al.* [37]. This technique can measure not only the negative ion density but also the negative ion temperature [38]. The related theory, analysis and application example of this method can be found in the same reference [38]. This diagnostics utilizes the photo-detachment reaction expressed as following



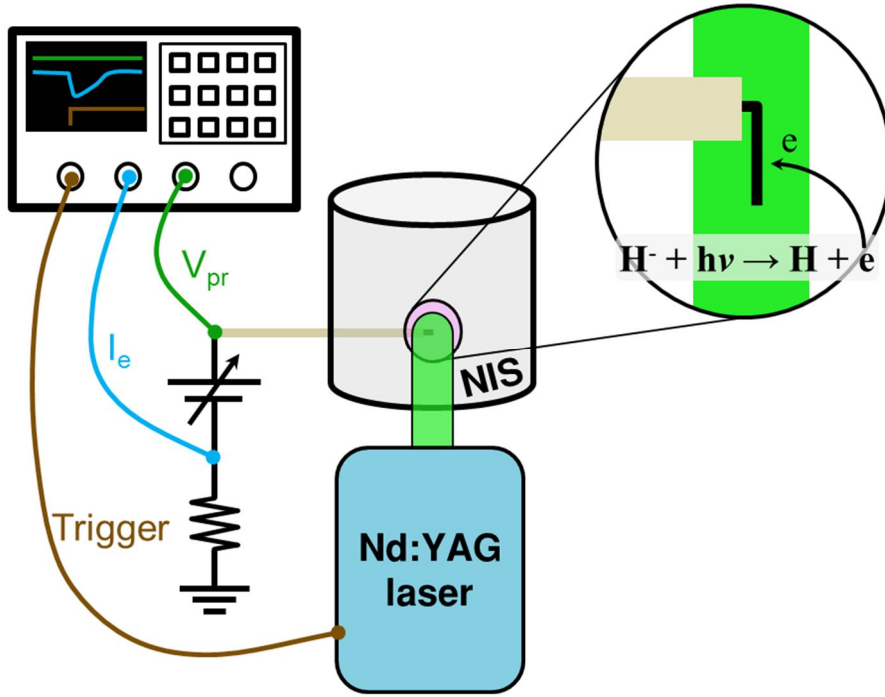


Figure 2.13. Schematic view of laser photo detachment system.

The laser photo-detachment system is schematically drawn in Figure 2.13. There is a probe biased higher than the plasma potential. Thus, the probe collects the electron saturation current. Then, if the laser is introduced into the plasma where negative ions and are generated, the photon detaches the electron of the H^- ion and the detached electron is collected by the nearby probe. The probe current rapidly increases and this current is proportional to the negative ion density. Amount of photo-detachment depends on the laser intensity and it is theoretically expected as following [37]

$$\frac{\Delta n^-}{n^-} = 1 - \exp\left(-\frac{E_L \sigma_{pd}}{S h\nu}\right) \quad (2.10)$$

where n^- and Δn^- are the negative ion density and the detached negative ion density, E_L is the laser energy per a single pulse, S is the cross section of the

laser beam, σ_{pd} is the photo detachment cross section, $h\nu$ is the photon energy. The laser photo-detachment current is expected to increase and become saturated according to the laser power. If the laser power is enough to detach every negative ion, the negative ion density is determined according to following relation:

$$\frac{n^-}{n_e} = \frac{\Delta I}{I_{es}}. \quad (2.11)$$

This pulsed current represents the negative ion density as long as following 3 conditions are satisfied.

1. The laser should detach only the hydrogen negative ion.
2. The diameter of the laser beam is larger than the electron sheath thickness of the laser probe.
3. The laser power is enough to detach all negative ions placed on the laser beam path.

If there are negative oxygen ions, the laser can detach the electron of the oxygen ions. The electron affinity of the negative oxygen ion species is 1.46 eV for O^- , 0.44 eV for O_2^- , and 2.1 eV for O_3^- [39]. The photon energy of a neodymium-doped yttrium aluminum garnet (Nd:YAG) laser is 1.17 eV for a fundamental mode (1064 nm) and 3.74 eV for a second harmonics (532 nm). Thus, if there are negative oxygen ions in the plasma, the detached electron current will be deviated from the equation 2.10 and the deviation depends on the photon energy. However, the detached currents obtained in this work are well matched with the theory, regardless of the laser wavelength, as shown in Figure 2.14. Thus, the plasma employed in this work is free from the oxygen negative ions.

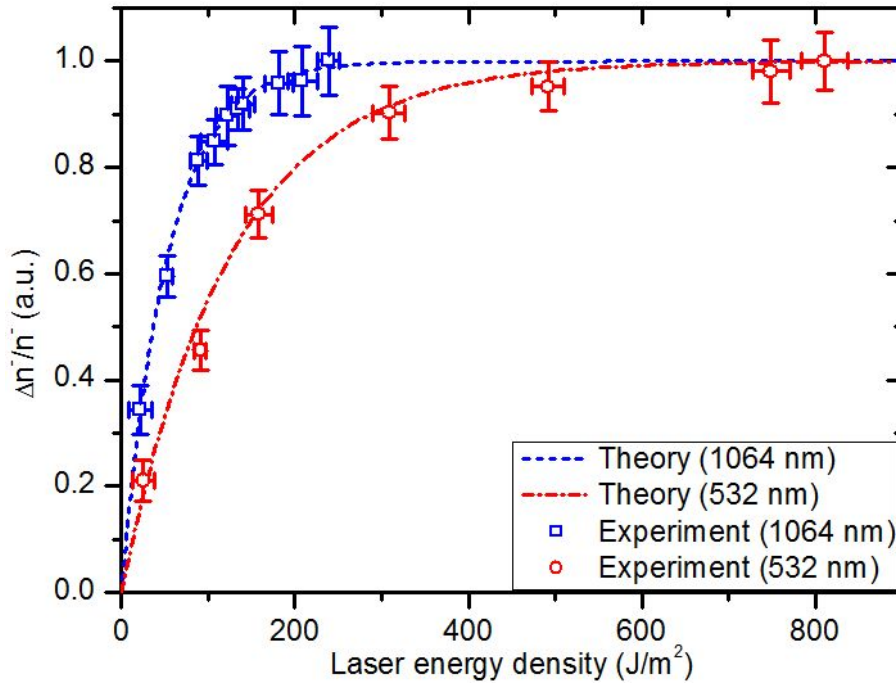


Figure 2.14. Dependence of the photo-detachment for the laser energy density and the laser wavelength.

The beam diameter of the Nd:YAG laser is about 1 cm. Thus, the laser beam is sufficiently larger than the sheath thickness of the plasma employed in this work.

Already shown in Figure 2.14, the laser energy density is enough to detach every negative hydrogen ion in the plasma. However, the laser power higher than depicted in Figure 2.14 is introduced, the laser ablates the probe surface. The ablated neutrals become ionized and increase the photo-detachment signal. Therefore, an upper limit of the laser power is determined by the ablation. As presented in Figure 2.15, the current induced by the laser ablation is about twenty folds higher than the photo detachment current. Thus, the laser power should be sustained as a proper value which can detach every negative ion but do not ablate.

As described above, the experimental condition of the laser photo-detachment is carefully examined and controlled. Also, the typical photo-detachment signal under the well fabricated experimental condition is depicted in Figure 2.16.

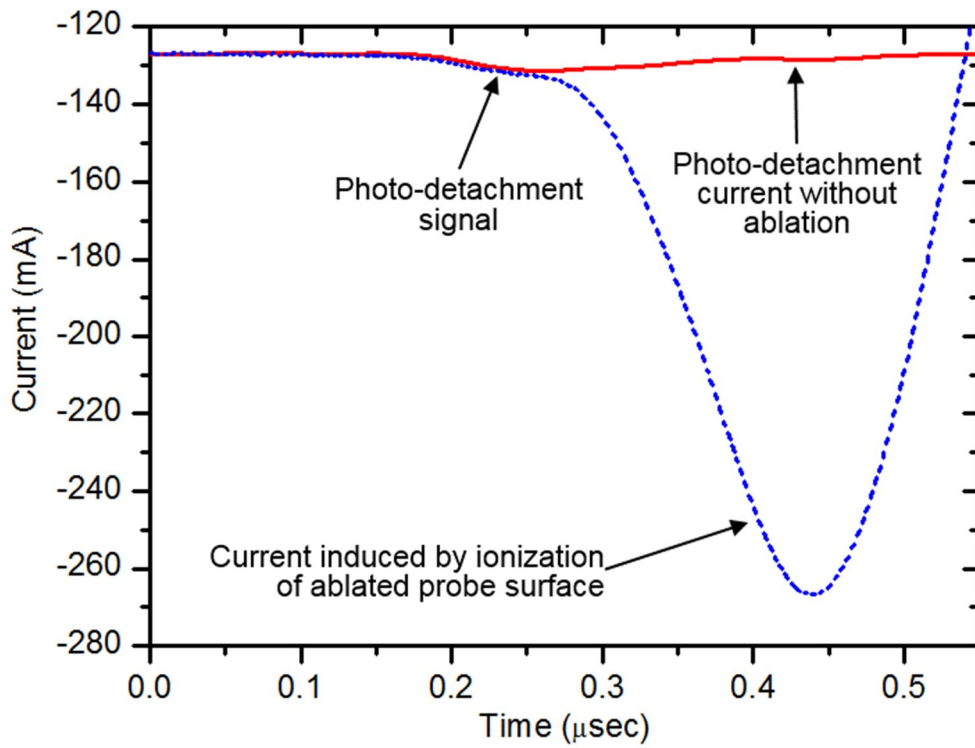


Figure 2.15. Photo-detachment current when laser ablates the probe surface.

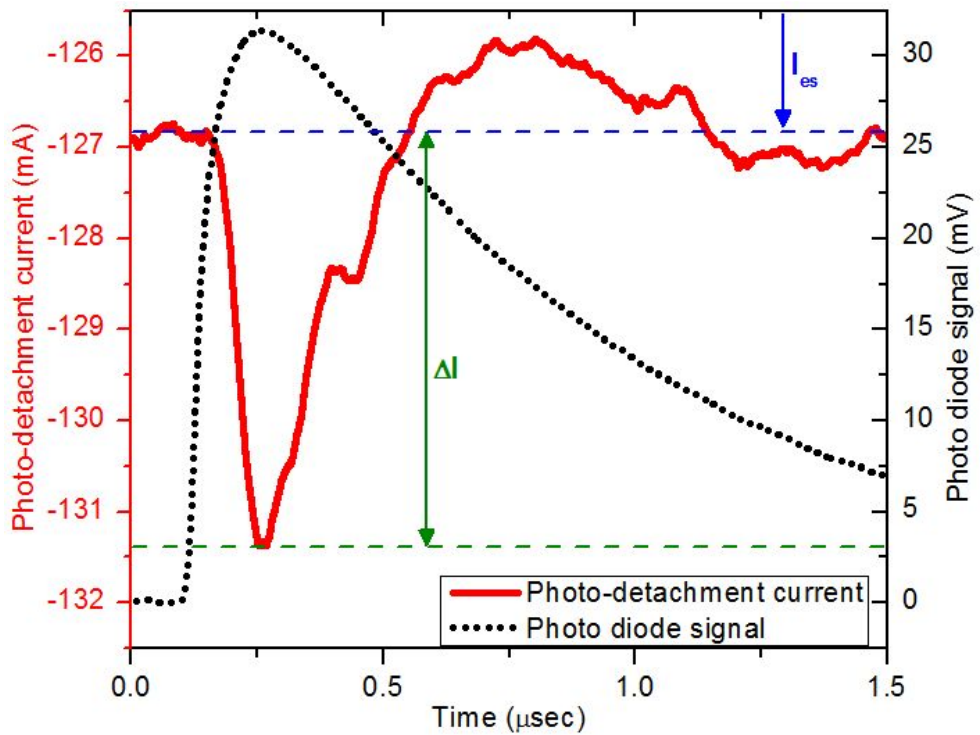


Figure 2.16. Typical laser photo-detachment signal and photo diode signal detecting laser pulse.

2.4. Fulcher- α Spectroscopy

The spectroscopic diagnostics utilizing molecular band spectra was first developed for nitrogen [40]. Later, many researchers developed the spectroscopic method for the Fulcher- α band spectrum of the hydrogen molecule [21, 41]. The Fulcher- α is a representative band spectrum accompanied with the radiative transition from the $d^3\Pi_u^-$ state (upper Fulcher state or briefly d-state) to $a^3\Sigma_g^+$ state (lower Fulcher state or briefly a-state) of the hydrogen molecule, as shown in energy level diagram Figure 2.17. The transition without a change in the vibrational number, v , is called as diagonal Fulcher- α band. Also, if a difference

of the rotational quantum number, J , between before and after the transition is zero, it is called as the Q-branch of the diagonal Fulcher- α band which is utilized in the spectroscopic diagnostics. There are also P- ($\Delta J = -1$) and R ($\Delta J = +1$)-branches. However, P- and R-branches are not utilized for the diagnostics because the radiative transition probabilities of these branches are not clearly defined. Upper state of P- and R-branches, $d^3\Pi_u^+$, is perturbed by $e^3\Sigma_g^+$ state.

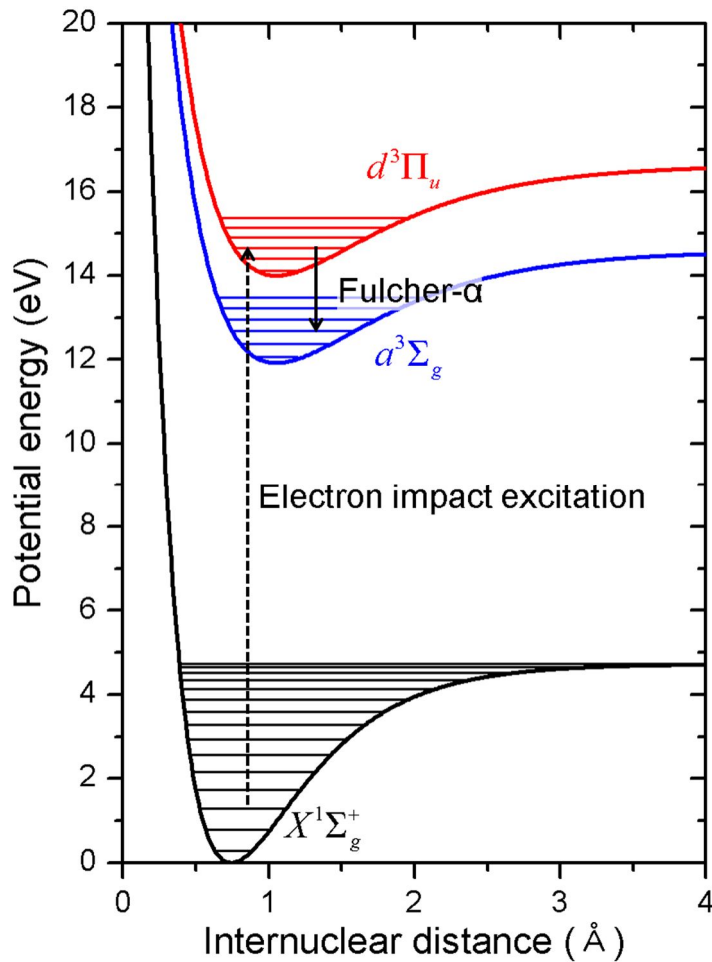


Figure 2.17. Energy level diagram for Fulcher- α spectrum related electronic and vibrational states of hydrogen molecule. The vibrational states of the lower and the upper Fulcher state are displayed only first 6 states ($\nu=0\sim 5$).

For the spectroscopic diagnostics, the high resolution spectrograph manufactured by Princeton instruments (model: SP-2500i) is employed. Focal length is 0.5 m, grating is 1800 grooves/mm, and instrumental broadening is ~ 0.07 nm. Its spectral sensitivity and the wavelength are calibrated by the tungsten lamp (LS-1-Cal, Ocean Optics Inc.) and Hg-Ar lamp (HG-1, Ocean Optics Inc.), respectively. Typical Fulcher- α spectrum measured by this experiment is depicted in Figure 2.18. The spectra from the first four vibrational and first five rotational states are depicted. The spectra of the higher vibrational and rotational states are difficult to identify from the measured spectrum. Thus, the Fulcher- α spectroscopy is limited to diagnose the higher vibrational states.

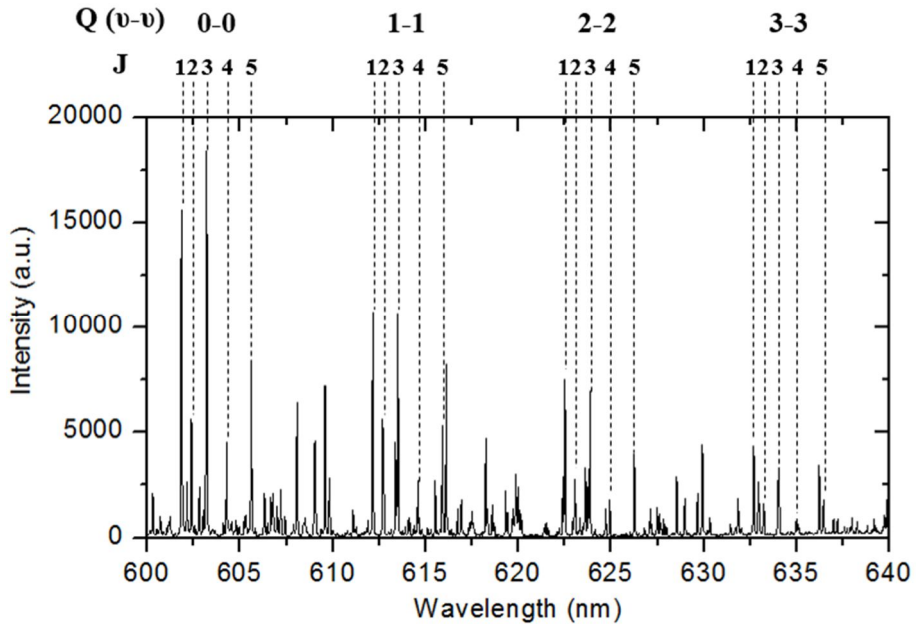


Figure 2.18. Typical Fulcher- α spectrum measured at negative ion source. The spectra from the first four vibrational and first five rotational states are depicted. Only these spectra are used in the diagnostics.

Many researches assume that the upper Fulcher state is populated by the electron collision with the electronic ground state, $X^1\Sigma_g^+$ (ground state or briefly X-state),

and depopulated by the spontaneous radiative decay [21, 41-43]. Thus, d-state reflects an information of X-state. For example, rotational temperature and vibrational temperature of X-state can be obtained. Furthermore, gas temperature and degree of dissociation can be determined by the physical relation and a spectroscopic model. The specific methodology and the physical condition, etc., are introduced in the following sections.

2.4.1. Rotational and Gas Temperature Determination by Fulcher- α Band Spectrum

To determine the rotational and translational temperature by the Fulcher- α spectroscopy, the rotational distribution function of X-state should be assumed as the Boltzmann distribution. Then the rotational temperature of d-state can be obtained from the Boltzmann fit of the Fulcher- α spectrum which obeys following equation [41-43]:

$$\ln \left(\frac{\lambda^4 I_{\nu\nu-J}}{S_{J,J} g_{as}} \right) = - \frac{hc}{kT_{rot}^{d,\nu}} F_{d,\nu}(J) + C \quad (2.12)$$

where λ is the wavelength of the corresponding transition. The degeneracy of nuclear spin, g_{as} , is 3 for odd J and 1 for even J -number. $S_{J,J}$ is a line strength calculated by the Hönl-London formula, $S_{J,J} = 0.5(2J+1)$. $hcF_{\nu}(J)$ is the rotational energy, where h and c are the Planck constant and the speed of light, respectively. The rotational term value, $F_{\nu}(J)$, is expressed as $B_{\nu}J(J+1)$, where B_{ν} is the rotational constant of (d, ν) -state. More detailed description on the molecular spectra, the Fulcher- α system and the related constants are well explained in the literature [44].

As shown in Figure 2.19, the respective rotational lines in the vibrational states, $0 \sim 3$, are well matched with the linear Boltzmann plot characterized corresponding rotational temperature. In general, the rotational temperature of the respective electronic state obeys following approximation [45]:

$$\frac{F_{d,v}(J)}{kT_{rot}^{d,v}} = \frac{F_{X,v}(J)}{kT_{rot}^{X,v}} \Rightarrow kT_{rot}^{X,v} = 2kT_{rot}^{d,v}. \quad (2.13)$$

Also, if the rotational-translation energy relaxation time is sufficiently shorter than a gas residence time in the chamber, the gas temperature and the rotational temperature of X-state are equilibrated [46]. The operating condition of the negative ion source in this experiment marginally satisfies this relation. Measured gas temperature is depicted in Figure 2.20. The gas temperature depends on the input RF power. Also, the gas temperature of the extraction region does not significantly change from that of the driver region. The gas temperature at the extraction region is sustained above 85% of that at the driver region, nevertheless the electron temperature and density at the extraction region are lower than a half of those at the drive region as shown in Figure 2.9 and Figure 2.10. This is important to understand the transport of molecules. Though plasma parameters change dramatically when the plasma passes through the magnetic filter region, the physical parameter of the molecule does not vary much. That is, the transport of the plasma is critically governed by the magnetic filter, but the hydrogen molecule may transport freely from the driver region to the extraction region. Thus, it is expected that the physical characteristics of the molecule in the extraction region mainly depends on that of the driver region.

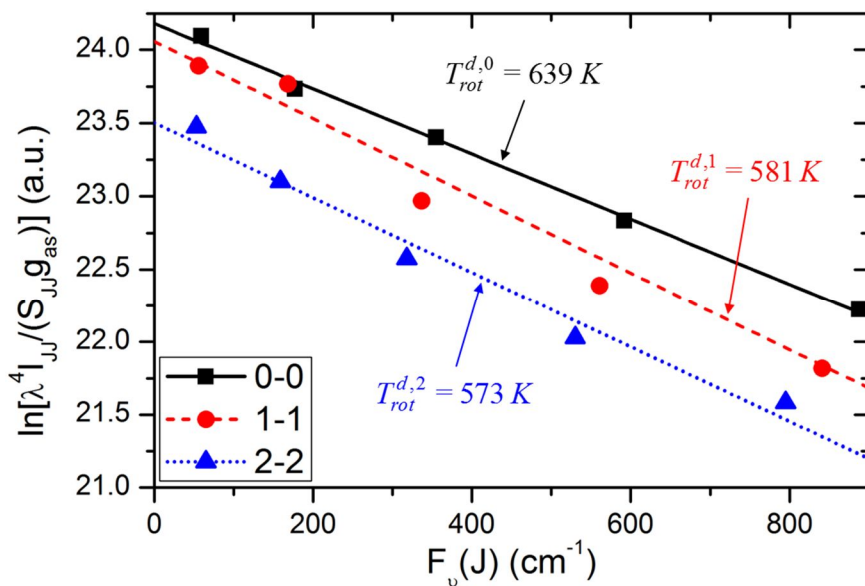


Figure 2.19. The Boltzmann plot of the rotational lines of (d, ν) -state. Each Boltzmann plots show good linearity and the rotational temperatures are matched within about 10% error.

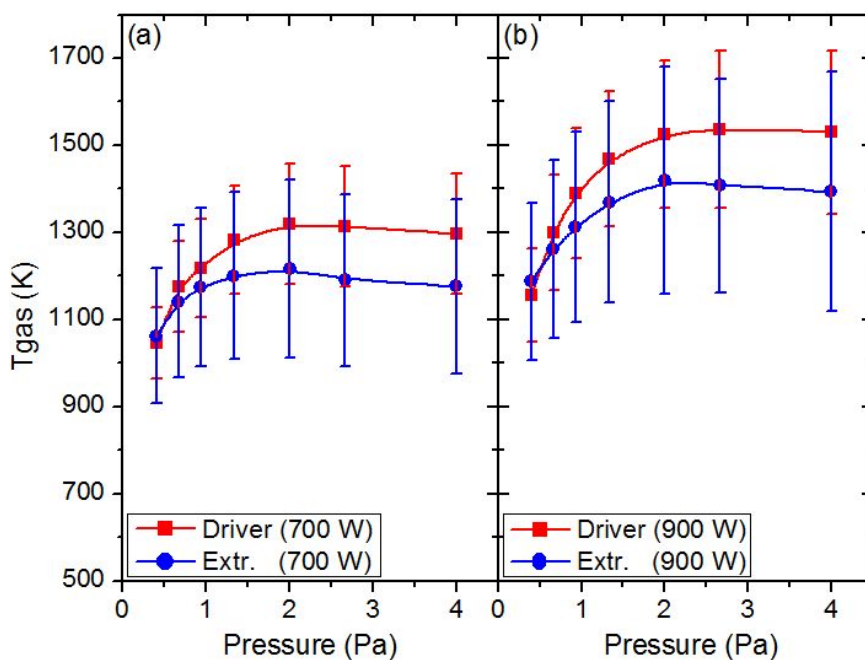


Figure 2.20. Gas temperature of the negative ion source (long chamber). Input RF power is (a) 700 W and (b) 900 W.

2.4.2. Vibrational Temperature Determination by Fulcher- α Spectroscopy

Fantz, *et al.*, improved the Fulcher- α spectroscopy by introducing vibrationally resolved excitation coefficients and Frank-Condon factors [21]. The vibrationally resolved population of the d-state can be obtained by the coronal model with the Boltzmann vibrational distribution function of the X-state, as follow:

$$\frac{I_{11}}{I_{00}} = \frac{\hbar\omega_{a,1}^{d,1} A_{a,1}^{d,1} \tau_{life,d,1}}{\hbar\omega_{a,0}^{d,0} A_{a,0}^{d,0} \tau_{life,d,0}} \frac{\sum_{v=0}^{14} \left[q_{X,v}^{d,1} \exp\{-G_X(v)/kT_{vib}^X\} \right]}{\sum_{v=0}^{14} \left[q_{X,v}^{d,0} \exp\{-G_X(v)/kT_{vib}^X\} \right]} = f(T_{vib}^X) \quad (2.14)$$

where I_{11} and I_{00} is the sum of the intensity of the respective rotational lines in the vibrational state 1 and 0, respectively. $\hbar\omega_{a,v'}^{d,v'}$ and $A_{a,v'}^{d,v'}$ are the photon energy and the transition probability corresponding transition where a subscript number is the vibrational number of the a-state and a superscript number is the vibrational number of the d-state. $\tau_{life,d,v'}$ is the radiative life time of (d, v') -state. $q_{X,v}^{d,v'}$ is the Franck-Condon factor corresponding the transition $(X, v) \rightarrow (d, v')$. $G_X(v)$ is the vibrational energy of the respective vibrational state in the electronic ground state. The result of the equation 2.14 is briefly explained as the Fulcher- α intensity ratio, I_{11}/I_{00} , is inversely proportional to the vibrational temperature, T_{vib}^X , up to 9,000 K. Detail description on the vibration temperature by the Fulcher- α spectroscopy could be found in the reference [21]. Also, the transition probabilities, the Franck-Condon factor and its explanation could be found in reference [47].

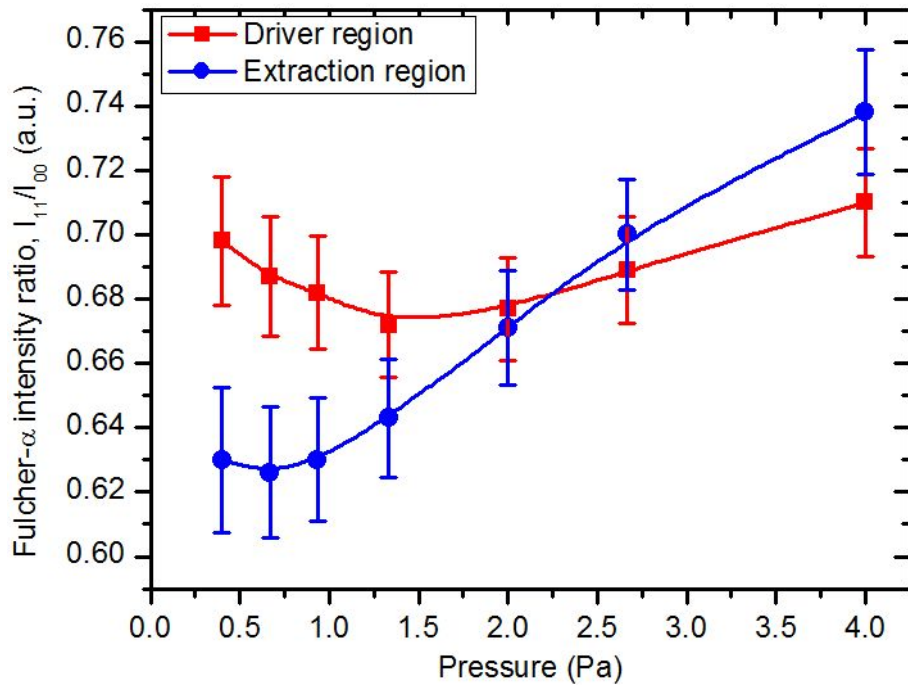


Figure 2.21. Fulcher- α intensity ratio obtained in negative ion source (long chamber). Input RF power is 700 W.

As mentioned in the previous section, the vibrational temperature is inversely proportional to the Fulcher- α intensity ratio. Then, the vibrational temperature of the extraction region looks higher than that of the driver region, in Figure 2.21. Also, the dependency of the vibrational temperature on the operating pressure is different from the dependency of the electron temperature. In addition, if the vibrational distribution function is in Boltzmann distribution characterized by the vibrational temperature, the negative ion density estimated by the Boltzmann VDF is largely deviated that of the laser photo-detachment diagnostics, as presented in Figure 2.22.*

The abnormal tendency of the Fulcher- α spectrum intensity ratio and large error of the negative ion density estimation are induced by the non-Boltzmann VDF

* Detail on the negative ion density estimation will be described in Chapter 3.

characteristics in the negative ion source. The non-Boltzmann VDF – or non-equilibrium VDF – is experimentally reported already, in other study on the negative ion source [18-20]. Thus, in order to complement the VDF diagnostics and improve the negative ion density estimation, a consideration on the non-Boltzmann VDF is required. Therefore, the 0-dimensional VDF model is developed by accounting the non-Boltzmann VDF in this study as described in chapter 3.

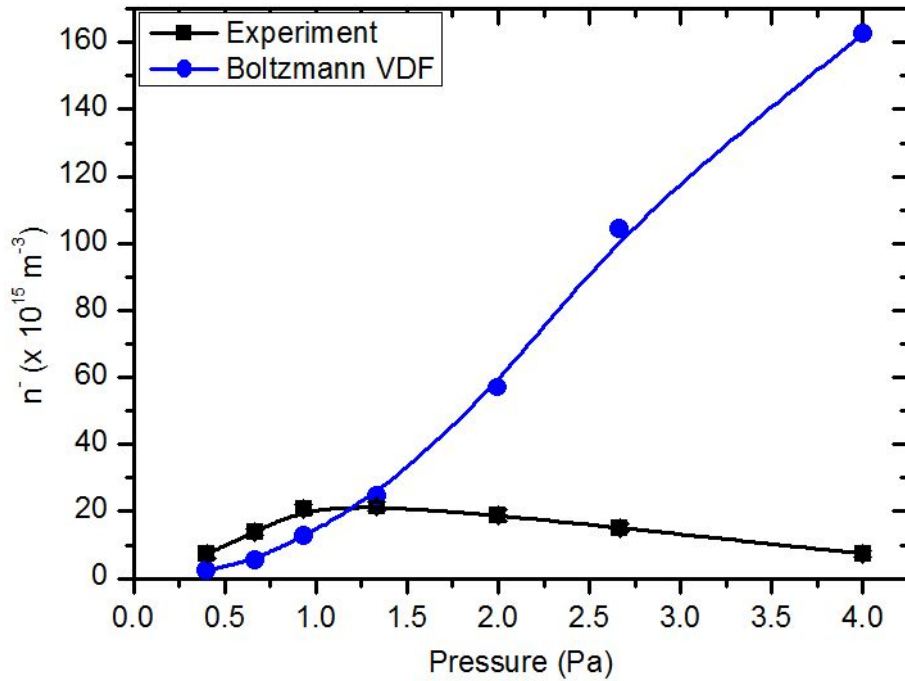


Figure 2.22. Negative ion density measured by the laser photo detachment and estimated by the Boltzmann VDF

Chapter 3. 0-D Model for Vibrational Distribution

Function of H₂

3.1. Particle Balance Model for VDF

As presented in Chapter 1, there are many 0-D model for the VDF in the negative ion source. Thus, this study fabricates the 0-D model referring the previous work [23-25, 48, 49]. However, there are difference in detailed feature. Xiao's work is conducted on the edge plasma simulator (MAP-II). This work mainly focused on a relative density of the vibrationally excited molecule and the Fulcher- α spectroscopy. The absolute value of the hydrogen molecule density and the negative ion density are not significant. Mosbach and Pagano's works include kinetic processes on other species such as H , H^+ , H_2^+ and H_3^+ . Mosbach's model accurately calculated the H^- density. This work was conducted based on a filament ion source and the VUV-LIF diagnostics. Pagano's work included cesium kinetics. These previous works reported non-Boltzmann characteristics of the VDF and high accuracy on H^- density calculation. However, the results of these models are difficult to be applied to the RF-driven cesium free negative ion source which is characterized as the H^- volume production. Therefore, in order to understand inter-relationship between the plasma parameter, the VDF, and the negative ion density, the VDF model should be developed based on RF-driven and magnetically filtered negative ion source with the consideration on the Fulcher- α spectroscopy. Also, the particle balance model already developed in Seoul national university [50, 51] became a foundation of this model.

3.1.1. Primary Description on the 0-D VDF Model

To solve the VDF, not only the vibrationally resolved density of H_2 but also as H , H^+ , H_2^+ , H_3^+ , and H^- should be included in the 0-D model. Thus, this model calculates the particle density of each ion and neutral species, at first. Total particle number density is constrained by the given operating pressure. Also, the summation of the densities of three positive ion species is set as the electron density measured by the Langmuir probe, to satisfy the quasi-neutrality. These two criteria can be expressed as

$$p/k_B T_g = \sum_{v=0}^{14} N_v + 0.5n_H + 0.5n_{H^+} + n_{H_2^+} + 1.5n_{H_3^+} \quad (3.1)$$

$$n_e = n_{H^+} + n_{H_2^+} + n_{H_3^+} \quad (3.2)$$

where, T_g is the gas temperature obtained from the Fulcher- α spectroscopy.

The reaction rate of the electron impact processes is obtained to integrate the product of the Maxwellian EEDF and the cross section of the respective processes. On the other hand, the reaction rate of heavy particle collision processes is defined as

$$K_{Heavy} = 4\pi \left(\frac{\mu}{2\pi k_B T_{eff}} \right) \int_0^{\infty} \sigma(v) v \left\{ v^2 \left(-\frac{\mu v^2}{2k_B T_{eff}} \right) \right\} dv \quad (3.3)$$

where μ is a reduced mass and T_{eff} is an effective temperature defined as

$$\mu = \frac{m_1 m_2}{m_1 + m_2}, \quad (3.4)$$

$$T_{eff} = \frac{m_1 T_1 + m_2 T_2}{m_1 + m_2}. \quad (3.5)$$

The temperature of H and H^+ is assumed as two folds of T_g [24, 52]. The temperature of H_2^+ and H_3^+ is set as T_g . The wall recombination factor (γ) of H atom is set as 0.1.

3.1.2. Collision Processes in 0-D VDF Model

The collision processes included in the 0-D model developed in this work are categorized as two groups. First one is the volumetric process which is the collision between the charged-charged, charged-neutral or neutral-neutral particles. Other one is the wall collision of the particles.

The volumetric processes included in VDF model are summarized in Table 3.1 and

Table 3.2. The kinetic processes are selected to refer the previous models. The reaction rates are mainly obtained from the reference [15]. Also, the descriptions in the Tables are originated from the same reference. The wall processes included in this model are listed in Table 3.3.

Table 3.1. List of volumetric collision processes of atom, ions and vibrationally unresolved molecule and descriptions.

Kinetic Process	Description	Ref.
$H + e \rightarrow H^+ + 2e$	Atomic ionization (Iz)	[15]
$H^+ + e \rightarrow H + h\nu$	Radiative recombination (Rr)	
$H^+ + 2e \rightarrow H + e$	Three-body recombination (Tr)	
$H_2^+ + e \rightarrow H + H^+ + e$	Dissociative excitation (De2)	
$H_2^+ + e \rightarrow 2H$	Dissociative recombination (Dr2)	
$H_2^+ + e \rightarrow 2H^+ + 2e$	Dissociative ionization (DIz)	
$H_3^+ + e \rightarrow H_2(v=0) + H \text{ or } 3H$	Dissociative recombination (Dr3-I, Dr3-II)	
$H_3^+ + e \rightarrow 2H + H^+ + e$	Dissociative excitation (De3)	
$H_2(v=0) + H_2^+ \rightarrow H + H_3^+$	H_3^+ formation (3F)	

Table 3.2. List of volumetric collision processes of vibrationally resolved molecule and description.

Kinetic Process	Description	Ref.
$H_2(v) + e \rightarrow H_2^- \rightarrow H_2(\omega) + e$	Vibrational excitation via H_2^- resonant states (e-V)	[48, 53]
$H_2(v) + e \rightarrow H_2(B^1\Sigma_u^+, C^1\Pi_u) + e$ $\rightarrow H_2(\omega) + e + h\nu$	Excitation-radiative decay vibrational excitation / de-excitation (E-V)	[54]
$H_2(v) + e \rightarrow H_2^- \rightarrow H + H^-$	Dissociative attachment (DA)	[15]
$H_2(v) + e \rightarrow 2H + e$	Dissociation (e-D)	[15, 53]
$H_2(v) + e \rightarrow H_2^+ + 2e$	Molecular ionization (e-I)	[15]
$H_2(v) + e \rightarrow H + H^+ + 2e$	Dissociative ionization (e-DI)	[55]
$H_2(v) + e$ $\rightarrow H_2(B, B', B'', C, D, D') + e$	Electronic excitation (e-E)	[15]
$H_2(v) + H^+ \rightarrow H_2(\omega) + H^+$	Proton impact excitation / de-excitation (p-V)	[56]
$H_2(v) + H^+ \rightarrow H + H_2^+$	Charge transfer (CTp)	[15]
$H + H_2^+ \rightarrow H_2(v) + H^+$	Charge transfer (CTm)	[56]
$H_2(v) + H \rightarrow H_2(v-1) + H$	Vibrational - Translational energy transfer (V-Ta)	[57]
$H_2(v) + H_2(\omega) \rightarrow H_2(v-1) + H_2(\omega)$	Vibrational - Translational energy transfer (V-Tm)	[58]
$H_2(v) + H_2(\omega) \rightarrow H_2(v+1) + H_2(\omega-1)$	Vibrational - Vibrational energy transfer (V-V)	[58]

Table 3.3. List and description on wall collision processes included in the model.

Wall Process	Description	Wall loss frequency [s ⁻¹]	Ref.
$H^+ + wall \rightarrow H$	H^+ neutralization	$1/\tau_{H^+}$	[50]
$H_2^+ + wall \rightarrow H_2(v=0)$	H_2^+ neutralization	$1/(\sqrt{2}\tau_{H^+})$	[50]
$H_3^+ + wall \rightarrow H_2(v=0) + H$	H_3^+ neutralization	$1/(\sqrt{3}\tau_{H^+})$	[50]
$H + wall \rightarrow 1/2 H_2(v=0)$	Associative recombination of H	$\gamma D_{eff}^H / \Lambda_{eff}^2$	[23]
$H_2(v) + wall \rightarrow H_2(\omega)$	Wall relaxation of vibrational state	$p_v D_{eff}^{H_2} / \Lambda_{eff}^2$	[23]

The wall processes of the ions are represented by the ion confinement time originated from the ion wall loss rate per unit plasma volume which is defined by the Bohm velocity, an effective plasma surface area and the plasma volume as follow [32, 59]

$$\frac{1}{\tau_i} = u_B \frac{A_{eff}}{V} = \sqrt{\frac{k_B T_e}{M_i}} \frac{A_{eff}}{V}. \quad (3.6)$$

A_{eff} is the effective surface area of the plasma enclosed by sheath edge. Thus ion confinement time of three ion species can be expressed as

$$\tau_{H^+} = \sqrt{\frac{m_p}{k_B T_e}} \frac{V}{A_{eff}}, \quad \tau_{H_2^+} = \sqrt{2}\tau_{H^+} \quad \text{and} \quad \tau_{H_3^+} = \sqrt{3}\tau_{H^+}. \quad (3.7)$$

In this 0-D model the ion confinement time is treated as the unknown parameter. That is, A_{eff} is calculated self-consistently satisfying the quasi-neutrality, based on the measured electron density.

The neutral wall loss is defined by the effective diffusion length and the effective

diffusion coefficient. For the cylindrical geometry of radius R and length L , the effective diffusion length is expressed as, [60],

$$\Lambda_{eff} = \left[\left(\frac{2.405}{R} \right)^2 + \left(\frac{\pi}{L} \right)^2 \right]^{-1/2}. \quad (3.8)$$

For the neutral particles, the model adopts the effective diffusion coefficients is expressed as [23]

$$\frac{1}{D_{eff}^X} = \frac{1}{D_{Kn}^X} + \frac{1}{D_{coll}^X}. \quad (3.9)$$

D_{Kn}^X is the Knudsen diffusion coefficient which can be approximated as follow [23]

$$D_{Kn}^X = \frac{\Lambda_{eff}}{3} \sqrt{\frac{8k_B T_X}{\pi M_X}} \quad (3.10)$$

where T_X and M_X are the temperature and the mass of corresponding atom or molecule. Also, a collisional diffusion coefficient is given by [23]

$$D_{coll}^X = \left(\sum_Y \frac{n_Y}{n} \frac{1}{D_{bi}^{X-Y}} \right)^{-1}. \quad (3.11)$$

where D_{bi}^{X-Y} is a binary diffusion coefficient can be calculated according to the Chapman-Enskog theory. Y is every collision partner, i.e., the hydrogen atom and molecule in this model. n is the summation of every Y particle density, n_Y . The binary diffusion coefficient is given by [60]

$$D_{bi}^{X-Y} = 0.0018583 \frac{\sqrt{T_{eff}^3 (1/M_X + 1/M_Y)}}{p_Y (\sigma_X/2 + \sigma_Y/2) \bar{\Omega}_{X-Y}^{(1,1)}} \quad (3.12)$$

where T_{eff} is the effective temperature in Kelvin, M_X and M_Y are mass in amu, P_Y is the partial pressure of particle Y in atm, σ is the collision cross section in angstrom ($\sigma_H = 1.1$ and $\sigma_{H_2} = 2.915$) and $\bar{\Omega}_{X-Y}^{(1,1)}$ is collisional integral of first order. The collisional integral can be obtained from following formula with the coefficients tabulated in Table 3.4 [61].

$$\bar{\Omega}_{X-Y}^{(1,1)} = \frac{a_1 + a_2 (T_{eff})^{a_3}}{a_4 + a_5 (T_{eff})^{a_6}}. \quad (3.13)$$

Table 3.4. Coefficients in the formula for the collisional integral.

	a ₁	a ₂	a ₃	a ₄	a ₅	a ₆
H-H	-6.1188e-1	5.8769	1.6199e-1	2.0103e-1	1.9714e-5	9.4241e-1
H-H ₂	-2.7945e-2	2.3506e-01	1.7072e-1	1.0823e-2	5.5119e-6	7.7910e-1
H ₂ -H ₂	2.4380e-5	2.4809e-03	1.4327	2.8742e-6	3.0371e-8	5.8695e-1

The hydrogen atom collided with the wall is recombined to the hydrogen molecule with a certainly probability called as the recombination factor (γ). In this work, the recombination factor is assumed as 0.1 [62].

The vibrational state of the molecule collided with the chamber wall is relaxed after the collision. In this work, the relaxation probability per a single wall collision is called as the wall relaxation coefficient, p_v . The wall relaxation coefficient, is referred in reference [23]. The vibrational state of the collided molecule is allowed to be transited to any lower state. At that time, the vibrational state after the collision depends on a re-populating probability, b_ω^v . The re-populating probability is referred in reference [63]. Thus, the transition probability from the vibrational

state v to state ω by the wall collision is $p_v b_\omega^v$ with

$$\sum_{\omega < v} b_\omega^v = 1. \quad (3.14)$$

p_v is listed in Table 3.5 and b_ω^v is depicted in Figure 3.1. The re-populating probabilities missed in reference are estimated by the interpolation or extrapolation.

Table 3.5. Coefficients for the vibrational relaxation by the wall collision [23].

v	1	2	3	4	5	6	7	8	9	10	11	12	13	14
p_v	0.1	0.2	0.3	0.4	0.4	0.4	0.4	0.4	0.4	0.5	0.5	0.5	0.5	1

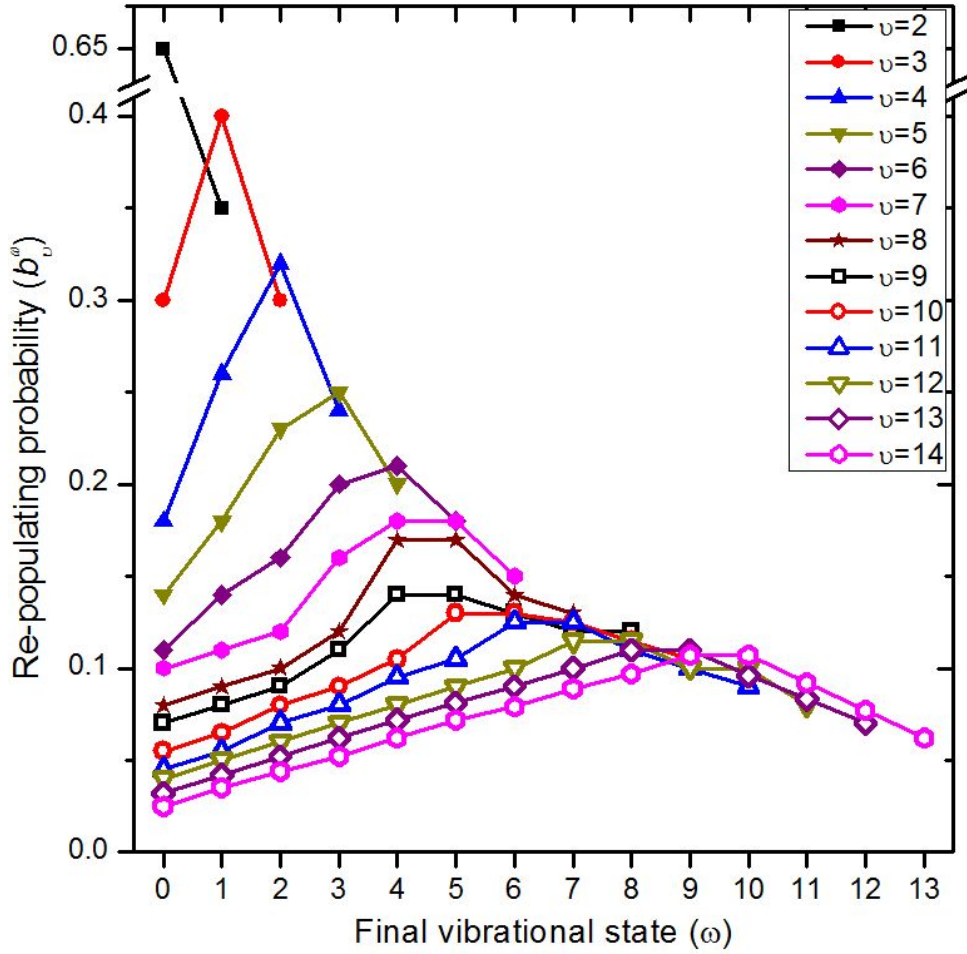


Figure 3.1. Re-populating probabilities by the wall collision [63].

The particle balance is equated by these collision processes. There are eighteen particle balance equations for 18 kinds of the particles ($H_2(v=1-14)$, H , H^+ , H_2^+ and H_3^+) in the model. The particle balance assumes the steady state. Also, the vibrationally ground state is solved by total particle conservation. An iterative solver scripted on MATLAB[®] is utilized to solve such series of nonlinear equations which are expressed as follows

$$\begin{aligned} \frac{\partial}{\partial t} n_{H^+} = n_e & \left[K_{Lz} n_{H^+} + (K_{De2} + 2K_{DLz}) n_{H_2^+} + K_{De3} n_{H_3^+} + \sum_v K_{e-DI}^v N_v \right] \\ & + \left(\sum_v K_{CTm}^v \right) n_{H_2^+} n_H - (K_{Rr} n_e + K_{Tr} n_e^2 + 1/\tau_{H^+}) n_{H^+} \end{aligned} \quad (3.15)$$

$$\begin{aligned} \frac{\partial}{\partial t} n_{H_2^+} = n_e & \sum_v (K_{e-I}^v N_v) + n_{H^+} \sum_v (K_{CTp}^v N_v) \\ & - \left[n_e (K_{De2} + K_{Dr2} + K_{DLz}) + \sum_v K_{CTm}^v n_H + K_{3F} N_{v=0} + \frac{1}{\sqrt{2}\tau_{H^+}} \right] n_{H_2^+} \end{aligned} \quad (3.16)$$

$$\frac{\partial}{\partial t} n_{H_3^+} = K_{3F} n_{H_2^+} N_{v=0} - \left[n_e (K_{Dr3-I} + K_{Dr3-II} + K_{De3}) + 1/\sqrt{3}\tau_{H^+} \right] n_{H_3^+} \quad (3.17)$$

$$\begin{aligned} \frac{\partial}{\partial t} n_H = n_e & \left[\sum_v \{ (K_{DA}^v + 2K_{e-D}^v + K_{e-DI}^v) N_v \} + (K_{Rr} + K_{Tr} n_e) n_{H^+} \right] \\ & + (K_{De2} + 2K_{Dr2}) n_{H_2^+} + (K_{Dr3-I} + 3K_{Dr3-II} + 2K_{De3}) n_{H_3^+} \\ & + K_{3F} n_{H_2^+} N_{v=0} + n_{H^+} \sum_v K_{CTp}^v N_v + \frac{n_{H^+}}{\tau_{H^+}} + \frac{n_{H_3^+}}{\sqrt{3}\tau_{H^+}} \\ & - \left(K_{Lz} n_e + \sum_v K_{CTm}^v n_{H_2^+} + \gamma \frac{D_{eff}^H}{\Lambda_{eff}^2} \right) n_H \end{aligned} \quad (3.18)$$

$$\begin{aligned}
\frac{\partial}{\partial t} N_v = & \sum_{\omega \neq v} \left[\left\{ \left(K_{e-V}^{\omega \rightarrow v} + K_{E-V}^{\omega \rightarrow v} \right) n_e + K_{p-V}^{\omega \rightarrow v} n_{H^+} \right\} N_\omega \right] \\
& + K_{CTM}^v n_H n_{H_2^+} + K_{V-Ta}^{v+1 \rightarrow v} n_H N_{v+1} + \left(\sum_{\omega} K_{V-Tm, \omega}^{v+1 \rightarrow v} N_\omega \right) N_{v+1} \\
& + \sum_{\omega} \left\{ \left(K_{V-V, \omega}^{v+1 \rightarrow v} N_{v+1} + K_{V-V, \omega}^{v-1 \rightarrow v} N_{v-1} \right) N_\omega \right\} \\
& + \frac{D_{eff}^{H_2}}{\Lambda_{eff}^2} \sum_{\omega > v} p_\omega b_v^\omega N_\omega \\
& - \left[\begin{aligned}
& n_e \left\{ \sum_{\omega \neq v} \left(K_{e-V}^{v \rightarrow \omega} + K_{E-V}^{v \rightarrow \omega} \right) \right. \\
& \left. + K_{DA}^v + K_{e-D}^v + K_{e-I}^v + K_{e-DI}^v + K_{e-E}^v \right\} \\
& + n_{H^+} \left\{ \left(\sum_{\omega \neq v} K_{p-V}^{v \rightarrow \omega} \right) + K_{CTP}^v \right\} + K_{V-Ta}^{v \rightarrow v-1} n_H \\
& + \sum_{\omega} \left(K_{V-Tm, \omega}^{v \rightarrow v-1} N_\omega \right) \\
& + \sum_{\omega} \left[\left(K_{V-V, \omega}^{v \rightarrow v-1} + K_{V-V, \omega}^{v \rightarrow v+1} \right) N_\omega \right] + \frac{D_{eff}^{H_2}}{\Lambda_{eff}^2} p_v
\end{aligned} \right] N_v \quad (\text{for } v = 1 \sim 14), \quad (3.19)
\end{aligned}$$

and

$$N_{v=0} = \frac{p}{k_B T_g} - 0.5 n_{H^+} - n_{H_2^+} - 0.5 n_{H_3^+} - 1.5 n_H - \sum_{v=1}^{14} N_v. \quad (3.20)$$

3.2. Corona Model for Fulcher- α Intensity Ratio

To examine the 0-D VDF model, the Fulcher- α spectrum intensity ratio is calculated and compared with the experiment. The Fulcher- α intensity ratio is calculated by the coronal model.

The coronal model is assumed that the upper Fulcher state is populated by the electron collisional excitation of the electronic state. Meanwhile, the upper Fulcher state is depopulated by the spontaneous radiative transition. Thus, the vibrational

distribution of the upper Fulcher state can be expressed as follow

$$\frac{dN_{d,v'}}{dt} = n_e \sum_{v=0}^{14} (N_v K_{X,v}^{d,v'}) - \frac{N_{d,v'}}{\tau_{life,d,v'}} = 0, \quad (3.21)$$

$$N_{d,v'} = \tau_{life,d,v'} n_e \sum_{v=0}^{14} (N_v K_{X,v}^{d,v'}), \quad (3.22)$$

where $N_{d,v'}$ is the density in (d, v') -state, $\tau_{life,d,v'}$ is life time of (d, v') -state and $K_{X,v}^{d,v'}$ is the reaction rate of the vibrationally resolved electronic excitation from (X, v) -state to (d, v') -state. According to Frank-Condon principle and a weighting factor considering the electron temperature effect on the excitation cross section [21], the $K_{X,v}^{d,v'}$ can be approximated as follow

$$K_{X,v}^{d,v'} = q_{X,v}^{d,v'} K_{X,v}^{d,0} = q_{X,v}^{d,v'} K_{X,0}^{d,0} \exp\left[\frac{\Delta G_X(v)}{kT_e}\right] \quad (3.23)$$

where $q_{X,v}^{d,v'}$ is Frank-Condon factor of the corresponding transition and $\Delta G_X(v)$ is the vibrational energy difference, i.e., $\Delta G_X(v) = G_X(v) - G_X(0)$. By the equation (3.22) and (3.23) the VDF of the upper Fulcher state can be obtained as the function of N_v and T_e .

$$N_{d,v'} = \tau_{life,d,v'} n_e K_{X,0}^{d,0} \sum_{v=0}^{14} \left[N_v q_{X,v}^{d,v'} \exp\left\{\frac{\Delta G_X(v)}{kT_e}\right\} \right]. \quad (3.24)$$

Since the Fulcher- α intensity is the product of the radiation energy, transition probability and $N_{d,v'}$, the Fulcher- α intensity can be calculated by

$$I_{v'v} = \hbar\omega_{a,v'}^{d,v'} A_{a,v'}^{d,v'} \tau_{life,d,v'} K_{X,0}^{d,0} \sum_{v=0}^{14} \left[N_{X,v} g_{X,v}^{d,v'} \exp\left\{ \frac{\Delta G_X(v)}{kT_e} \right\} \right]. \quad (3.25)$$

where $\hbar\omega_{a,v'}^{d,v'}$ is the radiation energy defined by the energy difference of the corresponding transition, i.e., $G_d(v') - G_a(v')$. The radiative transition probability, life time, Franck-Condon factor and vibrational energy of $X^1\Sigma_g^+$, $a^3\Sigma_g^+$ and $d^3\Pi_u^-$ state are reported in reference [47] and listed following tables.

Table 3.6. Radiative transition probability[s⁻¹] of the Fulcher-v transition for relevant vibrational number, ($d^3\Pi_u^-, v'$) - ($a^3\Sigma_g^+, v'$) transition.

	$v=0$	$v=1$	$v=2$	$v=3$	$v=4$	$v=5$
$v' = 0$	24077000	1655200	9274	0.0775	0.0562	2.16.E-05
$v' = 1$	1525800	20655000	3264900	29732	2.8248	0.1834
$v' = 2$	107120	2836900	17377000	4799300	62309	21.093
$v' = 3$	8395	318990	3887400	14317000	6236300	106330
$v' = 4$	586.95	36443	622330	4642000	11529000	7556300
$v' = 5$	38.977	3945	95638	989020	5084400	9065600

Table 3.7. Life time of $d^3\Pi_u^-$ state.

v'	$\tau_{life,d,v'}$ [sec]
0	3.88E-08
1	3.91E-08
2	3.91E-08
3	3.97E-08
4	4.00E-08
5	3.98E-08
6	4.02E-08
7	4.11E-08
8	4.22E-08
9	4.29E-08
10	4.37E-08
11	4.52E-08
12	4.78E-08
13	6.18E-08
14	9.59E-08
15	1.93E-07
16	4.11E-07
17	1.58E-07
18	9.33E-08
19	6.99E-08

Table 3.8. Frank-Condon factor for transition $(X^1\Sigma_g^+, v) - (d^3\Pi_u^-, v')$ with relevant vibrational number.

v	$v'=0$	$v'=0$	$v'=0$	$v'=0$	$v'=0$	$v'=0$
0	1.00E-01	1.71E-01	1.80E-01	1.54E-01	1.18E-01	8.44E-02
1	2.93E-01	1.63E-01	2.83E-02	7.75E-04	2.42E-02	5.02E-02
2	3.38E-01	3.03E-04	8.41E-02	1.09E-01	5.76E-02	1.35E-02
3	1.97E-01	1.62E-01	1.06E-01	3.13E-04	3.70E-02	6.89E-02
4	6.14E-02	2.96E-01	9.82E-03	1.22E-01	5.48E-02	8.65E-04
5	9.83E-03	1.66E-01	2.39E-01	2.41E-02	4.36E-02	8.33E-02
6	6.77E-04	3.79E-02	2.62E-01	1.22E-01	8.97E-02	5.74E-04
7	1.06E-05	3.03E-03	8.35E-02	3.17E-01	3.62E-02	1.14E-01
8	0	3.20E-05	7.22E-03	1.39E-01	3.34E-01	2.80E-03
9	0	1.30E-06	2.16E-05	1.14E-02	1.93E-01	3.37E-01
10	0	0	9.20E-06	1.61E-05	1.18E-02	2.36E-01
11	0	0	1.00E-07	2.41E-05	5.50E-04	5.43E-03
12	0	0	0	3.50E-06	3.60E-06	2.36E-03
13	0	0	0	4.00E-07	1.15E-05	1.88E-04
14	0	0	0	0	3.70E-06	9.00E-06

Table 3.9. Vibrational energy of $X^1\Sigma_g^+$, $a^3\Sigma_g^+$ and $d^3\Pi_u^-$ state.

v	$X^1\Sigma_g^+$	$a^3\Sigma_g^+$	$d^3\Pi_u^-$
0	0.27504	12.06523	14.12644
1	0.79104	12.37833	14.40462
2	1.27809	12.67453	14.66721
3	1.73664	12.95430	14.91472
4	2.16685	13.21802	15.14758
5	2.56873	13.46591	15.36612
6	2.94214	13.69804	15.57057
7	3.28667	13.91430	15.76107
8	3.60148	14.11432	15.93764
9	3.88512	14.29732	16.10011
10	4.13553	14.46207	16.24841
11	4.34985	14.60721	16.38227
12	4.52401	14.72997	16.50080
13	4.65343	14.82635	16.60306
14	4.72986	14.89177	16.68730
15	\	14.92531	16.75031
16		14.93754	16.78921
17		14.94376	16.81297
18		14.94789	16.82863
19		16.83768	
v max	14	18	19

3.3. Negative Ion Density Estimation

The negative ion density is estimated from the solved VDF. The negative ion produced via DA reaction is destructed by the electron detachment, mutual neutralization, associative and non-associative detachment by the atom listed in Table 3.10.

Then, the negative ion density in equilibrium is described as follow

$$\frac{\partial}{\partial t} n^- = n_e \sum_v K_{DA}^v N_v - \left[K_{ED} n_e + \sum_{i=1}^3 K_{MN-i} n_{H_i^+} + (K_{AD} + K_{NAD}) n_H \right] n^- = 0, \quad (3.26)$$

$$n^- = \frac{n_e \sum_v K_{DA}^v N_v}{K_{ED} n_e + \sum_{i=1}^3 K_{MN-i} n_{H_i^+} + (K_{AD} + K_{NAD}) n_H}, \quad (3.27)$$

The negative ion density in section 2.4.2 is also estimated by the equation 3.27 with the Boltzmann VDF defined as follow

$$N_v = N_0 \exp \left[-\frac{G_X(v)}{k_B T_{vb}^X} \right], \quad (3.28)$$

Table 3.10. List of negative ion destruction processes included in the model and description.

Destruction Process	Description	Ref.
$H^- + e \rightarrow H + 2e$	Electron detachment (ED)	[15]
$H^- + H^+ \rightarrow 2H$	Mutual neutralization (MN-1)	[64]
$H^- + H_2^+ \rightarrow H + H_2$	Mutual neutralization (MN-2)	[64]
$H^- + H_3^+ \rightarrow 2H + H_2$	Mutual neutralization (MN-3)	[64]
$H^- + H \rightarrow H_2 + e$	Associative detachment (AD)	[15]
$H^- + H \rightarrow 2H + e$	Non-associative detachment (NAD)	[15]

3.4. Result and Limitation of 0-D VDF Model

From the equation (3.25) and the constants in Table 3.6 ~ Table 3.9, the Fulcher-

α intensity ratio can be obtained. As shown in Figure 3.2, the Fulcher- α intensity ratio is well matched with the spectroscopic measurement. Also, the normalized VDF is depicted in Figure 3.3. The 0-D model shows the non-Boltzmann VDF like other researches [23-25, 48, 49]. The non-Boltzmann VDF is generated by the vibrational excitation mechanism which strongly depends on the electron temperature. As written in section 1.1.1, two vibrational excitation reactions show very different characteristics according to the electron temperature. The e-V reaction can contribute to the excitation of the lower states with the low electron temperature. However, the e-V reaction is not effective to excite the higher states. In contrast to the e-V reaction, the E-V reaction is efficient to excite the higher vibrational states with high electron temperature. Thus, the higher states are relatively over-populated than the lower states at the high electron temperature plasma. On the contrary, the higher states are less-populated than the lower states at the low electron temperature plasma. Therefore, these different tendency of the vibrational excitation processes induce the non-Boltzmann VDF.

Finally, it is confirmed that the 0-D model can simulate the population of the lower vibrational states, by the comparison of the Fulcher- α intensity ratio. Also, it is expected that the VDF of the negative ion source is in the non-Boltzmann distribution. However, since, the Fulcher- α spectrum is mainly sensitive to lower states of VDF, the negative ion density estimation is required to verify the higher states result.

The calculation result of the negative ion density determined by the equation 3.27 and the VDF obtained by the 0-D model is depicted in Figure 3.4. The result of the 0-D model looks like improving the accuracy of the negative ion density estimation at the low pressure, because the 0-D model corrects the higher vibrational states which are under-estimated by the Boltzmann VDF determined by the conventional analysis on the Fulcher- α spectrum. However, the 0-D model still over-estimates the negative ion density at high pressure regime. It means that the 0-

D model does not reflect a physical situation at high pressure regime in the negative ion source. A physical phenomenon guessed to become significant at the high pressure is the collision between the hydrogen molecule and the molecule or the atom. Since, the vibrational-translational energy transfer reaction by the atom or other molecule works to only decay the vibrational state, a possibility of the VDF relaxation will increase at the high pressure during the vibrationally excited hydrogen molecule is transported from the driver region to the extraction region. Thus, a multi-dimensional model is required to consider a variation of the VDF during the transport. In this work, 1 dimensional model is developed and presented in Chapter 4.

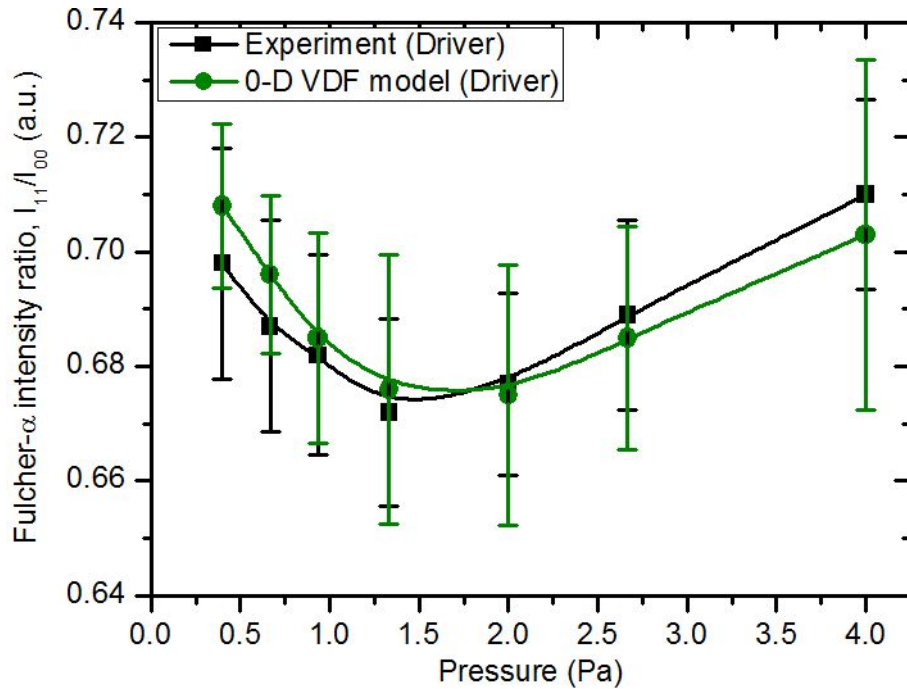


Figure 3.2. Comparison of the Fulcher- α intensity ratio determined by the experiment and the 0-D VDF model at the driver region of the long chamber and 700 W RF input power.

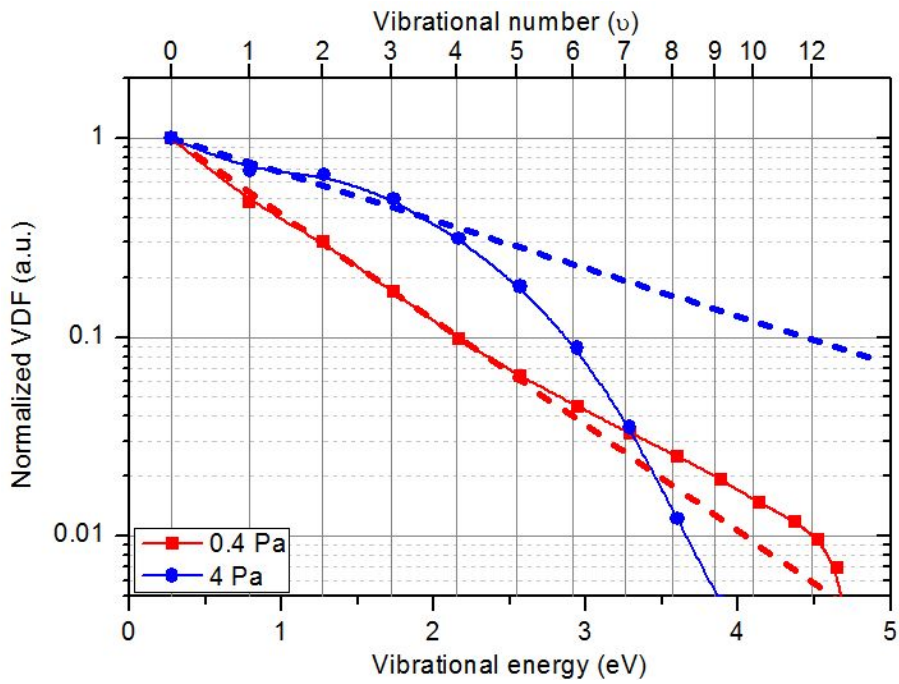


Figure 3.3. VDF obtained by 0-D model at the long chamber with RF input power 700 W. Dashed line is the Boltzmann distribution estimated from the lower vibrational states.

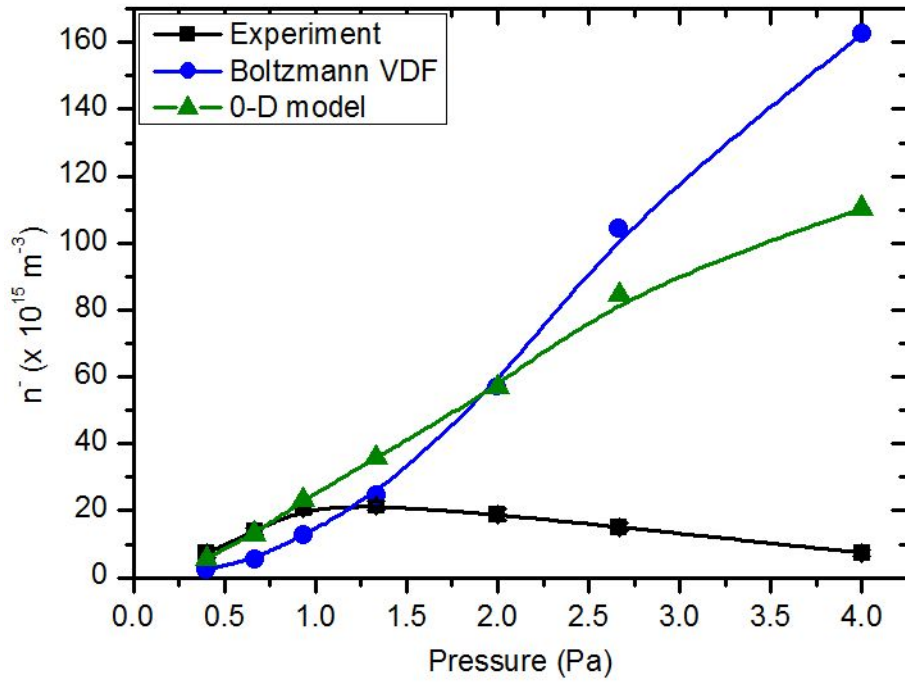


Figure 3.4. The negative ion density obtained by the experiment, Boltzmann VDF and 0-D VDF model at the long chamber discharged by 700 RF power.

Chapter 4. 1-Dimensional Transport Model to Describe the Relaxation of the Vibrational Distribution Function of the Hydrogen Molecule in Negative Ion Source

4.1. Structure of 1-D Transport Model for VDF of H₂

To consider the effect by the transport, the multi-dimensional transport model should be developed. It is started from the steady-state continuity equation.

$$\frac{\partial}{\partial t} N_v + \nabla \cdot \bar{\Gamma} = \nabla \cdot \bar{\Gamma} = \left(\frac{\partial}{\partial t} N_v \right)_{Coll.} \quad (4.1)$$

In principle, the continuity equation should be solved three-dimensionally. However, this study mainly concerns the transport from the diver region to the extraction region. Thus, to reduce the dimension and solve 1-dimensionally, the continuity equation is integrated on a disk geometry which is serially compose the cylindrical chamber, as schematically presented in Figure 4.1.

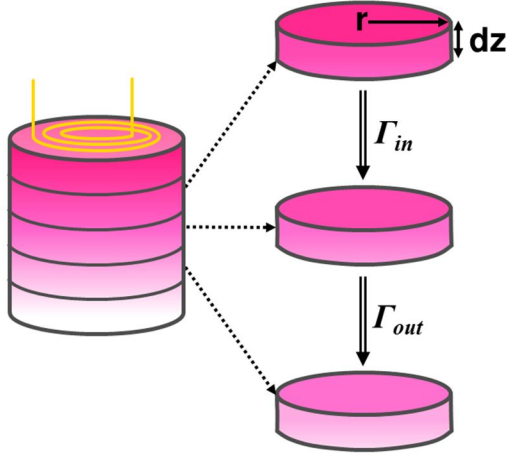


Figure 4.1. Discretized chamber by the disk elements.

If the equation (4.1) is integrated with assumptions that there is no radial flux and no spatial distribution of the all physical parameters inside the integrated volume, the integration is converted as 1-dimensional continuity equation:

$$\int_V \nabla \cdot \bar{\Gamma} dV = \int_A \bar{\Gamma} \cdot d\bar{A} = \int_V \left(\frac{\partial}{\partial t} N_v \right)_{Coll.} dV, \quad (4.2)$$

$$(-\Gamma_{in} + \Gamma_{out}) \pi r^2 = \left(\frac{\partial}{\partial t} N_v \right)_{Coll.} \pi r^2 dz, \quad (4.3)$$

$$\frac{d}{dz} \Gamma_z = \left(\frac{\partial}{\partial t} N_v \right)_{Coll.}. \quad (4.4)$$

There are two kinds of the flux in the negative ion source. The flux is generated by the diffusion and the advection. If the diffusive flux is sufficiently larger than the advective flux, the flux in equation (4.4) can be substituted as $\Gamma = -D \nabla_z N_v$. Then, the left-hand side of the equation (4.4) can be approximated as follow

$$\frac{d}{dz} \Gamma_z = \frac{d}{dz} \left(-D \frac{d}{dz} N_v + N_v u_{Adv.} \right) = \frac{d}{dz} \left(-D \frac{d}{dz} N_v \right). \quad (4.5)$$

The equation (4.5) is second order differential equation for the N_v . Thus, two initial condition is required to solve equation (4.5). However, there is only one initial condition for N_v . It is difficult to establish the initial condition for the flux, Γ . Thus, to reduce order of the differential equation, other assumption is introduced. Let the diffusion flux is defined as follow

$$-D \frac{d}{dz} N_v = N_v u_{Diff}. \quad (4.6)$$

where u_{Diff} is the diffusive velocity defined as follow

$$u_{Diff} = -D \frac{dN_v/dz}{N_v}. \quad (4.7)$$

If $|u_{Diff} \nabla_z N_v| \ll |N_v \nabla_z u_{Diff}|$ is satisfied, the equation (4.5) can be converted as follows

$$\frac{d}{dz} \Gamma_z = u_{Diff} \frac{d}{dz} N_v = \left(\frac{\partial}{\partial t} N_v \right)_{Coll.} = \left(\sum_{\omega \neq v} \nu_{k-1}^{\omega \rightarrow v} N_\omega - \sum_{\omega \neq v} \nu_{k-1}^{v \rightarrow \omega} N_v \right). \quad (4.8)$$

The first order differential equation (4.8) can be solved with the single initial condition. The initial condition is the VDF calculated by the 0-D model. The discretization of this equation is schematically presented in Figure 4.2.

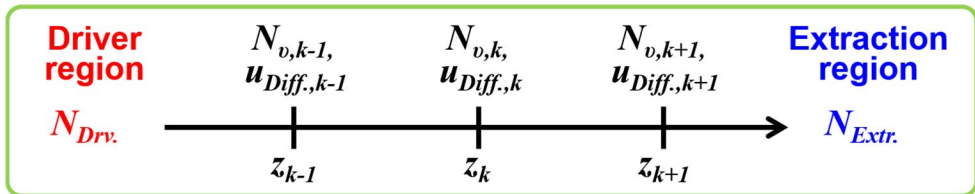


Figure 4.2. Discretization of equation (4.8).

$$N_{v,k} = N_{v,k-1} + \frac{\Delta z}{u_{Diff.}} \left(\sum_{\omega \neq v} v_{k-1}^{\omega \rightarrow v} N_{\omega,k-1} - \sum_{\omega \neq v} v_{k-1}^{v \rightarrow \omega} N_{v,k-1} \right). \quad (4.9)$$

Equation (4.9) is discretized expression of the 1-D continuity equation. The physical meaning of this equation is that the hydrogen molecule density in the vibrational state v at position z_k is determined by the hydrogen molecule density in vibrational state v at position z_{k-1} and the variation induced by the collision during the molecule travels Δz with the speed $u_{Diff.}$. The collision processes included in equation (4.9) are all processes in

Table 3.2 and the wall process of the hydrogen molecule in Table 3.3.

In equation (4.9), the source collision frequency, $\nu_{k-1}^{\omega \rightarrow v}$, and the loss collision frequency, $\nu_{k-1}^{v \rightarrow \omega}$, are specifically expressed as follow

$$\begin{aligned} \nu_{k-1}^{\omega \rightarrow v} = & \sum_{\omega \neq v} \left[(K_{e-V}^{\omega \rightarrow v} + K_{E-V}^{\omega \rightarrow v}) n_e + K_{p-V}^{\omega \rightarrow v} n_{H^+} \right] + K_{V-Ta}^{v+1 \rightarrow v} n_H \\ & + \left(\sum_{\omega} K_{V-Tm, \omega}^{v+1 \rightarrow v} N_{\omega, k-1} \right) + \sum_{\omega} (K_{V-V, \omega}^{v+1 \rightarrow v} N_{v+1, k-1} + K_{V-V, \omega}^{v-1 \rightarrow v} N_{v-1, k-1}), \quad (4.11) \\ & + \frac{D_{eff}^{H_2}}{\Lambda_{eff}^2} \sum_{\omega > v} p_{\omega} b_v^{\omega} \end{aligned}$$

$$\begin{aligned} \nu_{k-1}^{v \rightarrow \omega} = & n_e \left\{ \sum_{\omega \neq v} (K_{e-V}^{v \rightarrow \omega} + K_{E-V}^{v \rightarrow \omega}) \right. \\ & \left. + K_{DA}^v + K_{e-D}^v + K_{e-I}^v + K_{e-DI}^v + K_{e-E}^v \right\} \\ & + n_{H^+} \left\{ \left(\sum_{\omega \neq v} K_{p-V}^{v \rightarrow \omega} \right) + K_{CTp}^v \right\} + K_{V-Ta}^{v \rightarrow v-1} n_H \quad (4.12) \\ & + \sum_{\omega} (K_{V-Tm, \omega}^{v \rightarrow v-1} N_{\omega, k-1}) + \sum_{\omega} \left[(K_{V-V, \omega}^{v \rightarrow v-1} + K_{V-V, \omega}^{v \rightarrow v+1}) N_{\omega, k-1} \right] + \frac{D_{eff}^{H_2}}{\Lambda_{eff}^2} p_v \end{aligned}$$

The reaction rate, K , of the electron impact processes are determined by an averaged electron temperature and the density in a transport region. Also, it is assumed that fractions of each ion species are conserved. Furthermore, the hydrogen atom density and total density of the hydrogen molecule are same with those of the 0-D model. The transport region is started from the center of the driver region, where the electron temperature becomes to decrease, and ended at the center of the extraction region, where the negative ion density measurement is conducted, as depicted in Figure 4.3.

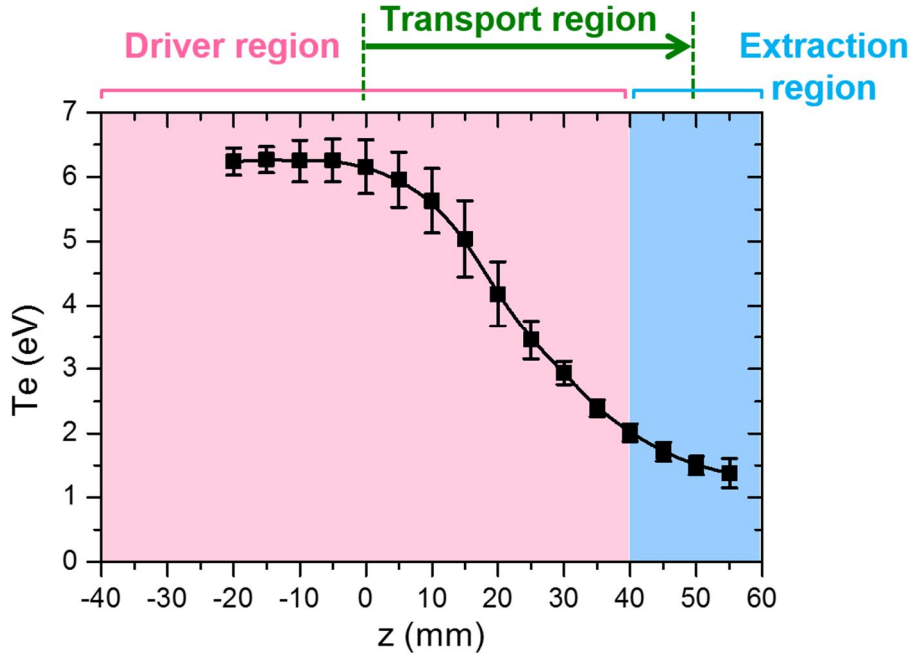


Figure 4.3. Transport region and the electron temperature profile.

Before introducing the 1-D model result, it should be examined that the assumptions which are utilized in the reduction of the order of the differential equation.

The first assumption is that the diffusive flux is sufficiently larger than the advective flux determined by the gas flow rate. The advection flow is defined as follow

$$u_{Adv.} = \frac{q[m^3/s] \times 101325[Pa]}{A[m^2] \times p[Pa]} \quad (4.11)$$

where $q[m^3/s]$ is the flow rate measured by the mass flow controller, $p[Pa]$ is pressure in the negative ion source and $A[m^2]$ is cross sectional area of the chamber. The diffusive speed obtained from the 1-D model is almost 3 orders of the magnitude faster than the advective speed. Thus, the first assumption is valid in

the model.

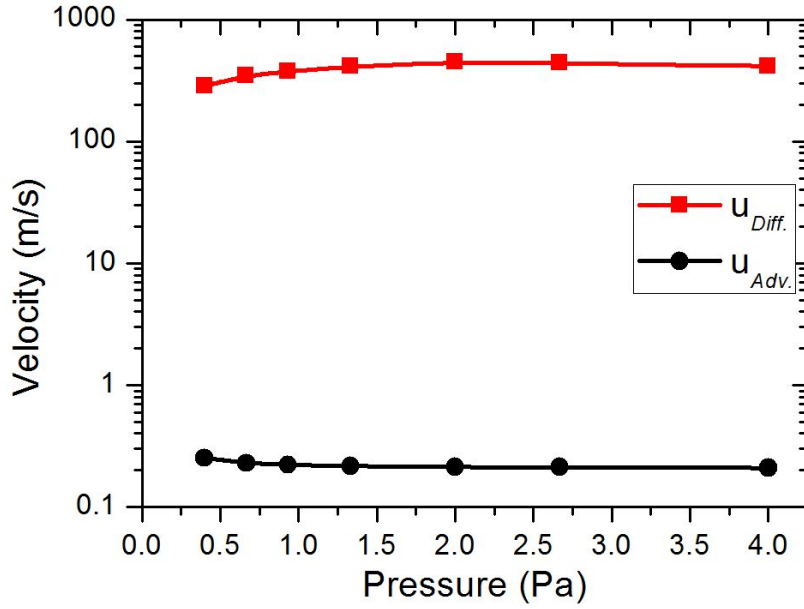


Figure 4.4. Comparison of the diffusive and advective speed.

The other assumption is $|u_{Diff} \cdot \nabla_z N_v| \ll |N_v \nabla_z u_{Diff}|$. This assumption can be converted as follow

$$|\nabla_z L_{N,v}| \ll 1 \quad (4.12)$$

where the L_N is a hydrogen molecule density scale length which is defined as

$$L_{N,v} = \frac{N_v}{\nabla N_v} \quad (4.13)$$

As depicted in Figure 4.5, after ~ 1.5 cm the gradient of the scale length becomes larger than 1. Thus, the equation (4.8) is invalid after the 1.5 cm. However, it is expected that the invalid region is not significant to solve the continuity equation for the hydrogen molecule. The gradient of the hydrogen molecule density

is reduced faster than a reduction of the hydrogen molecule density, when the gradient of the scale length is larger than 1. That is, the hydrogen molecule density is saturated. Thus, there is no significant problem when the equation (4.8) is utilized to solve the transport in the negative ion source, in spite of the second assumption is partially invalid.

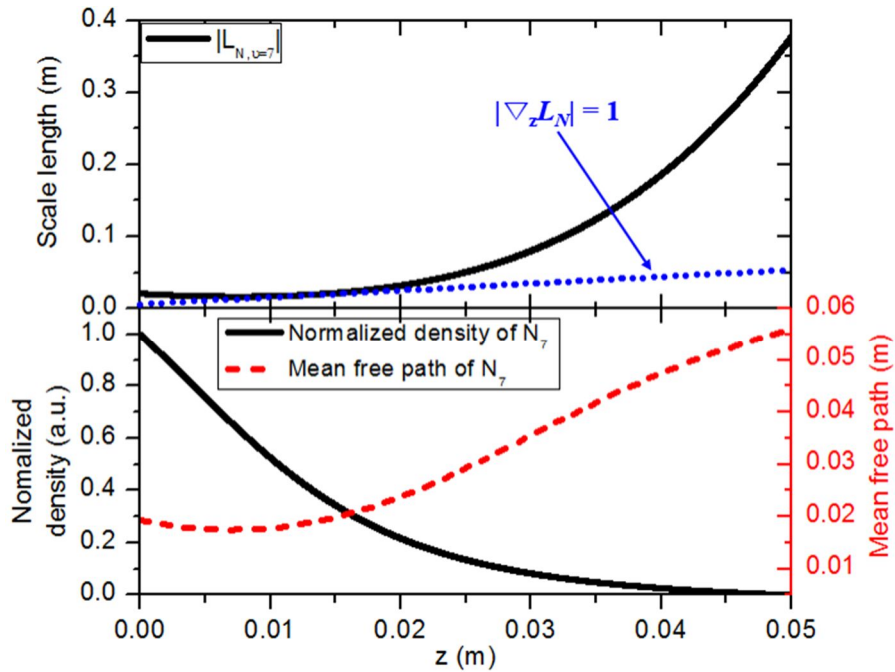


Figure 4.5. Scale length, normalized density and mean free path of the hydrogen molecule in vibrational state 7.

4.2. Main Result of the 1-D Model

Utilizing the VDF calculated by the 1-D transport model, the Fulcher- α spectrum intensity ratio at the extraction region and the negative ion density are calculated and compared with the experimental results. The Fulcher- α spectrum intensity ratio obtained from the 1-D neutral particle transport shows a fairly good agreement with the measurement conducted at the extraction region, as depicted in Figure 4.6. When the 0-D model is only applied while ignoring neutral particle transport, the calculated Fulcher- α spectrum intensity ratio cannot reproduce the experimental result. Thus, Figure 4.6 clearly shows the influence of the transport of neutral particles in the analysis of the Fulcher- α spectrum intensity ratio measured at the extraction region.

According to the numerical model, the higher states of the VDF decay to the lower states during the transport so that the VDF calculated at the extraction region is greatly different from that calculated at the driver region, as shown in Figure 4.7. It should be noted that the vibrational temperature, which is conventionally determined from the 4 lower states [22], cannot be a representative of the VDF. Indeed, conventional method gives a much higher vibrational temperature for the extraction region depicted as a dashed line in Figure 4.7. This means that the Fulcher- α spectrum is not sufficient to diagnose the highly excited vibrational states. Thus, the negative ion density calculation should be verified.

Figure 4.8 shows the negative ion density measured and evaluated by three models. The accuracy of the negative ion density estimation by 1-D model is significantly improved, at high pressure. It is expected that this improvement is induced by the consideration on the variation of the VDF during the transport of the hydrogen molecule. In specific, the higher states which plays the key role in the negative ion production decay to the lower states, as shown in Figure 4.7.

Thus, it is confirmed that the relaxation of the higher states is the important physics in the magnetically filtered negative ion source which divided into the driver and the extraction region. They are specifically described that factors determining the relaxation of the VDF, in the next chapter.

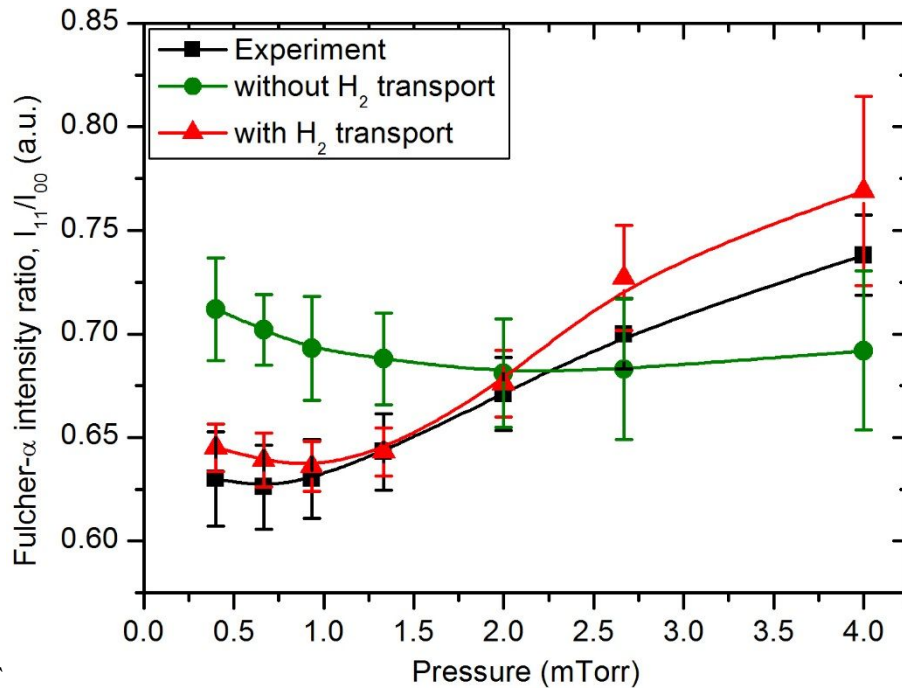


Figure 4.6. Fulcher- α spectrum intensity ratio calculated by the 1-D model and measured by the spectrometer at the extraction region.

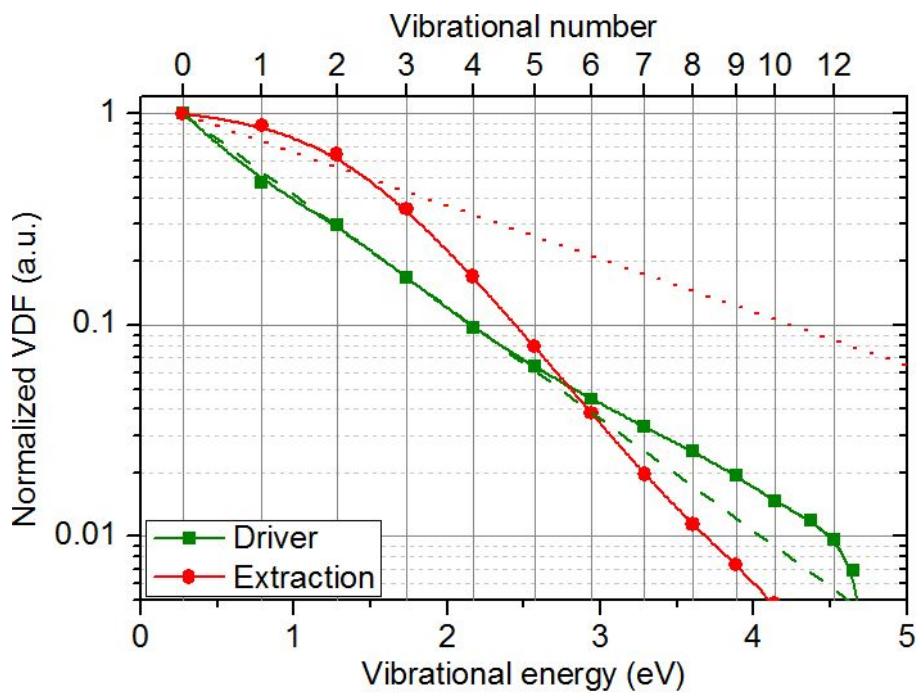


Figure 4.7. VDF calculated by the 1-D model with 4 Pa and 700 W discharge condition at the long chamber. The Boltzmann VDF estimated by the lower states (dashed line: driver region, dotted line: extraction region).

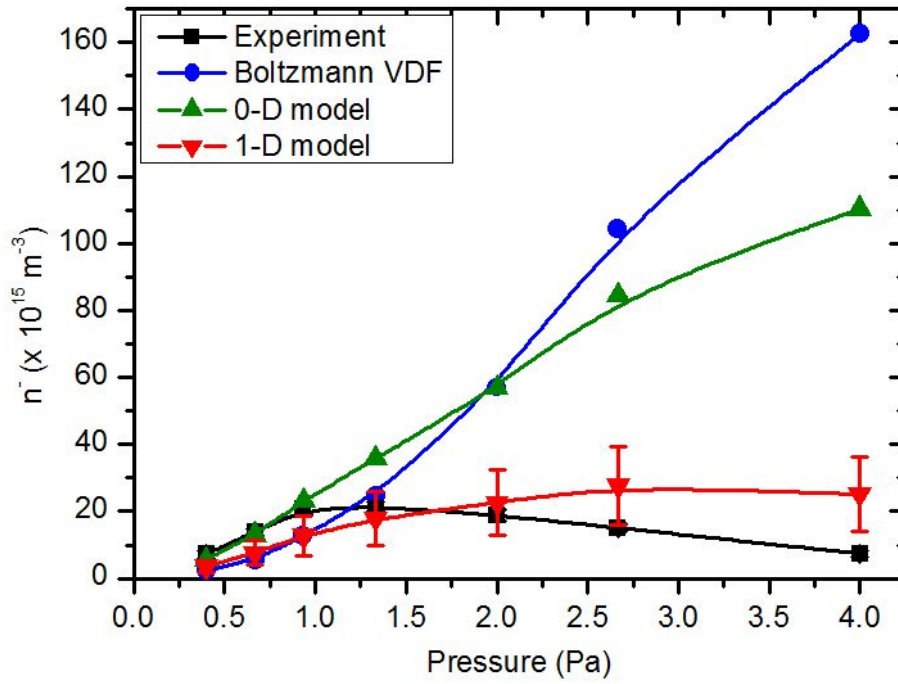


Figure 4.8. Comparison of the negative ion density obtained by the experiment, Boltzmann VDF, the 0-D VDF model, and the 1-D model.

Chapter 5. Analysis of Kinetics of Vibrational Distribution Function of Hydrogen Molecule in Negative Ion Source

5.1. Vibrational Relaxation and Negative Ion Density

5.1.1. Vibrational Relaxation and Effective Mean Free Path

It is identified that the relaxation of the highly excited vibrational states is important phenomenon in the negative ion source. In specific, the effect of the vibrational-translation (V-T) energy transfer increases at the high pressure. Since the neutral particle density is directly proportional to the pressure, the V-T reaction severely affects the higher states of the VDF. The mean free path of the relevant reactions which affect VDF is shown in Figure 5.1. At first, at the low operating pressure, the E-V reaction is dominant, because the electron temperature is sustained high. Since the E-V reaction can excite the vibrational state, the vibrational relaxation by the wall can be compensated. Thus, the decay of the vibrational state is weakly occurred at the low pressure. However, at the high pressure, the e-V reaction is occurred instead of the E-V reaction. Also, the V-T reaction dominantly induces the vibrational relaxation. The vibrational relaxation of the higher states could not be compensated by the e-V reaction, because the e-V reaction is effective to excite the only lower vibrational state. Thus, the vibrational relaxation becomes important at high operating pressure.

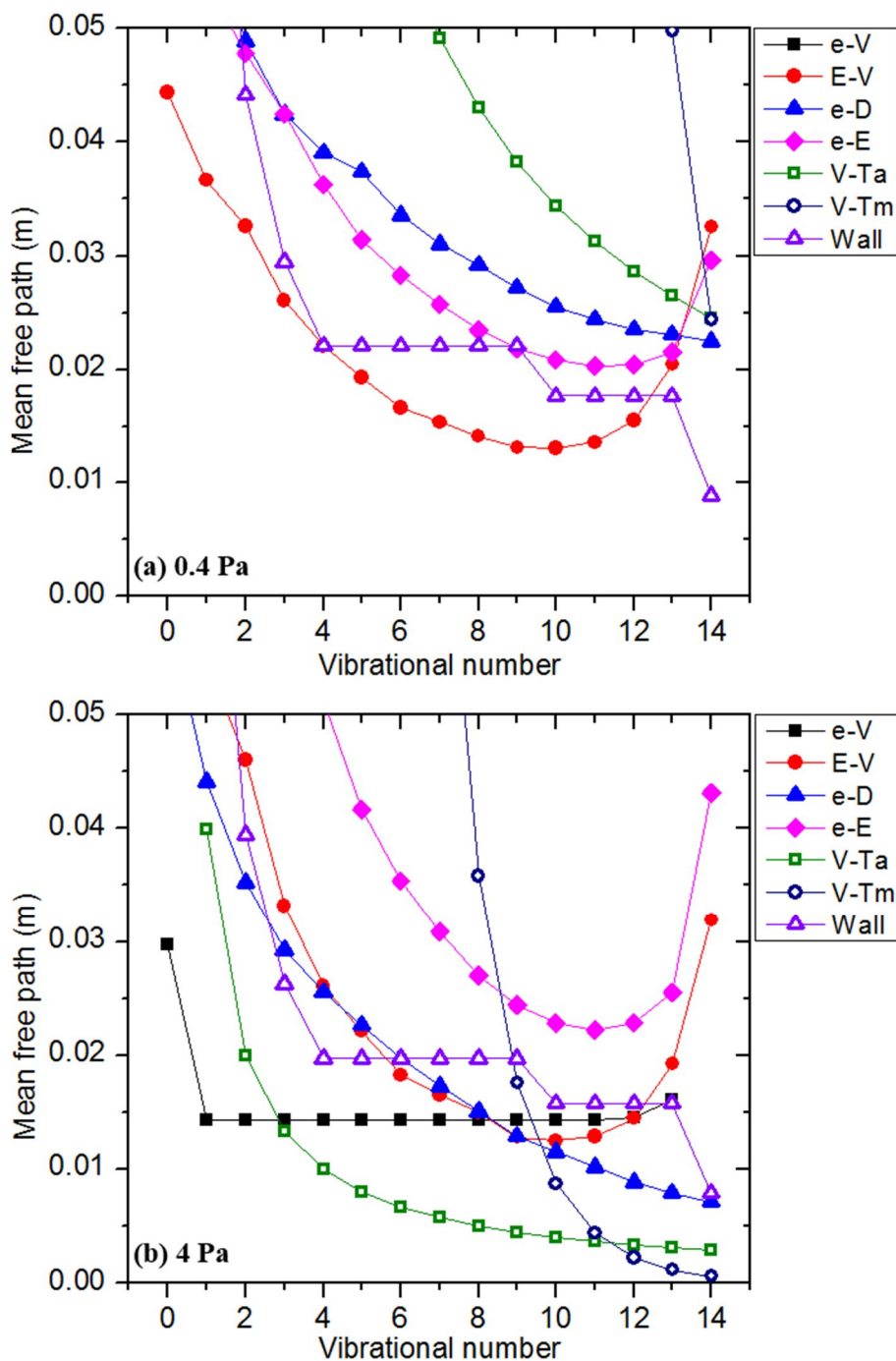


Figure 5.1. Mean free path for the relevant processes affecting VDF. The mean free paths of V-T with atom and molecule are strongly depends on the operating pressure, (a) 0.4 Pa and (b) 4 Pa.

For the more quantitative analysis, the equation (4.8) is converted as follow

$$u_{Diff} \cdot \frac{d}{dz} N_v = \left(\sum_{\omega \neq v} v_{k-1}^{\omega \rightarrow v} N_\omega - \sum_{\omega \neq v} v_{k-1}^{v \rightarrow \omega} N_v \right) \equiv v_v^{eff} N_v \quad (5.1)$$

where v_v^{eff} is an effective collision frequency of the hydrogen molecule in vibrational state v . The effective collision frequency is introduced to simplify the equation and be helpful for understanding. Also, the effective collision frequency has a positive sign when the source term is larger than the loss term in the parenthesis of the equation (5.1) and a negative sign when the loss term is larger. The equation (5.1) can be re-arranged as follow

$$L_{N,v} \equiv \frac{N_v}{dN_v/dz} = \frac{u_{Diff}}{v_v^{eff}} \equiv \lambda_v^{eff} \quad (5.2)$$

That is, the density scale length, $L_{N,v}$, defined in equation (4.13), is mathematically same as an effective mean free path, λ_v^{eff} , of the hydrogen molecule in the vibrational state v . The physical meaning of the effective mean free path can be the rate of decay with the travel distance. That is, the effective mean free path becomes shorter when the effective collision frequency becomes larger. As depicted in Figure 5.2, the effective mean free path decreases according to the increase of the operating pressure, because the collision by the neutrals increases. Thus, it can be expected that the VDF is relaxed by the V-T transfer at the high pressure. Also, the higher states decay faster, because the effective mean free paths of the higher states are shorter than lower states, as depicted in Figure 5.3. Consequently, the consideration on the vibrational relaxation during the transport of the hydrogen molecule improves the negative ion density estimation at the high operating pressure.

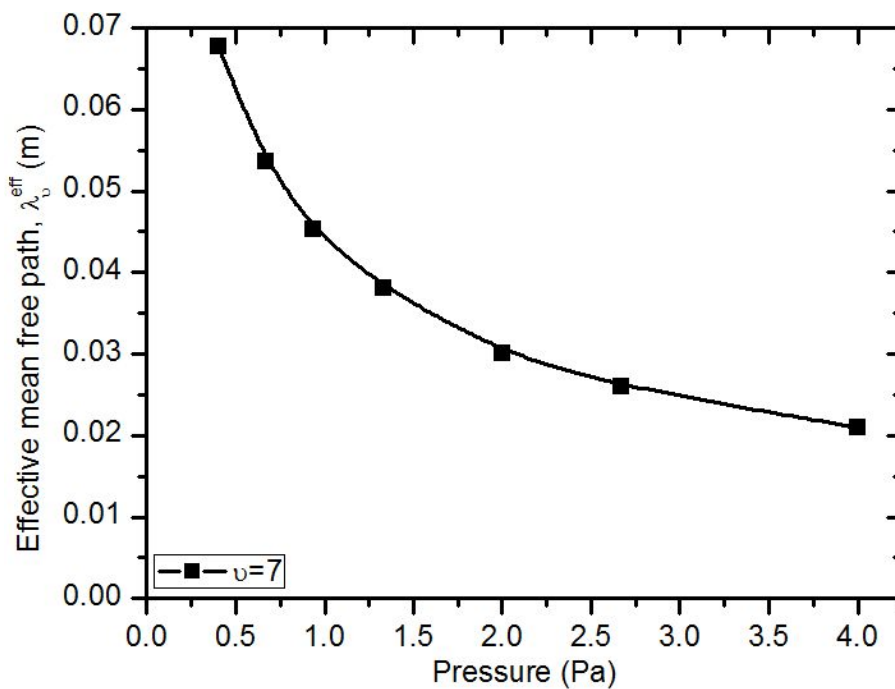


Figure 5.2. Pressure dependence of the absolute value of the effective mean free path of hydrogen molecule in vibrational state 7. The effective mean free path has the negative sign, because the vibrational state 7 decays.

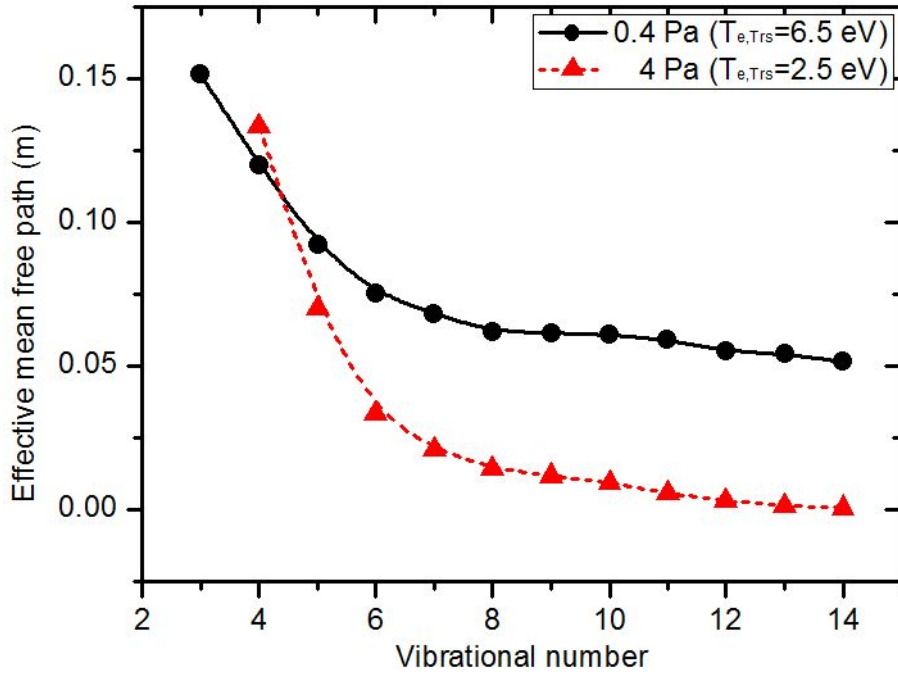


Figure 5.3. The effective mean free paths of the respective vibrational states. The effective mean free paths of the higher states are shorter than the lower states. The effective mean free paths of the lower states are elongated, because the depopulation of the higher states populates the lower states.

5.1.2. Vibrational Relaxation and Transport Length

The density profile of the vibrationally excited states are presented in Figure 5.4, according to the position. The density of the vibrationally excited molecule decreased and is saturated. Thus, it can be expected that a length between the driver and the extraction region may affect the vibrational relaxation. The length between two regions is called as a transport length, $L_{Trs.}$, from now. Thus, to examine the effect by the transport length, the negative ion density measured at the short chamber is compared with the 1-D model result.

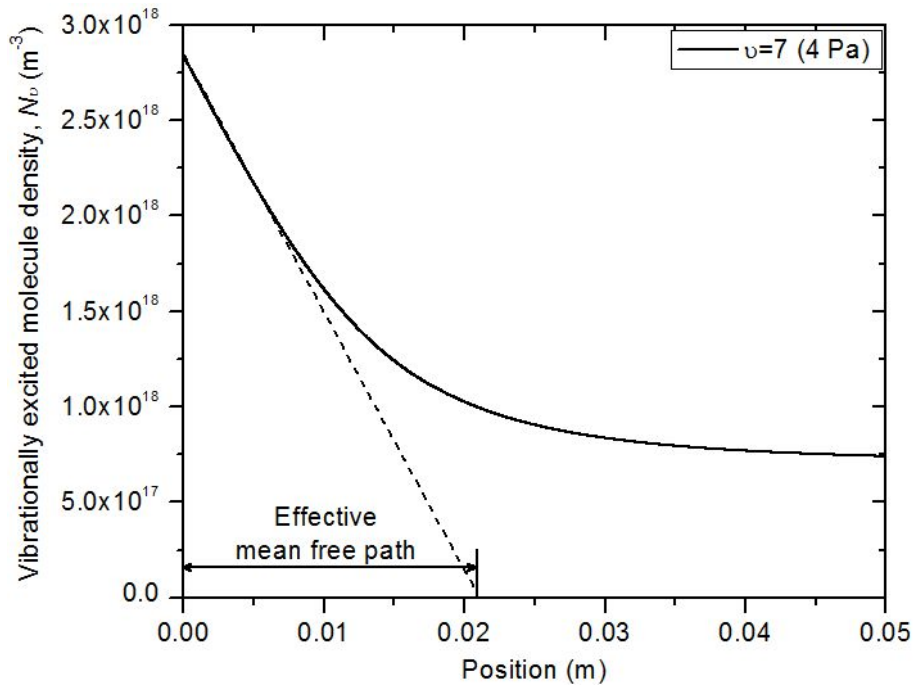


Figure 5.4. Density profile obtained by the 1-D model, according to the position.

If the chamber length does not change the transport length, 1-D model has to solve on the same transport length with the long chamber. However, 1-D model with 5 cm transport length severely under-estimates the negative ion density, as shown in Figure 5.5. The result for 3 cm is similar with the experiment. The 1-D model with 5 cm transport length calculates like that the hydrogen molecule travels the longer distance than a real situation. Then, the VDF is more relaxed and the negative ion density is under-estimated. Therefore, the transport length is affected by the chamber length and it determines the hydrogen molecule traveling length.

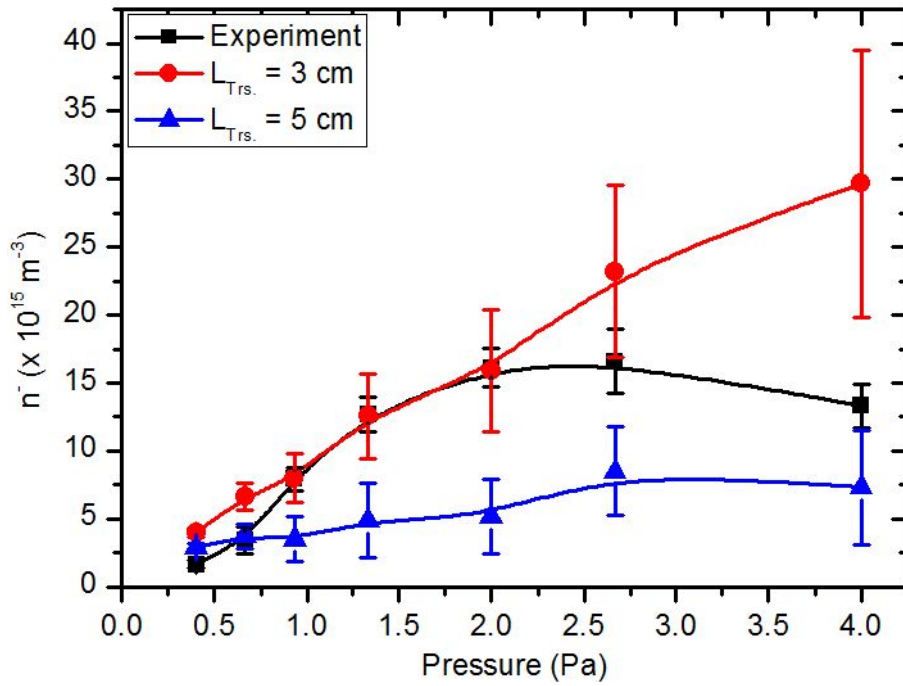


Figure 5.5. The negative ion density calculation in the short chamber with different transport length.

Strictly, the transport length depends not only the chamber length but also the plasma profile. The point, where the electron temperature starts to decrease, moves to the antenna side as increase of the pressure, as depicted in Figure 5.6. Thus, the 1-D model calculates the VDF transport with the transport length set as the function of the pressure. As shown in Figure 5.7, the transport length set as depending on the pressure improves the negative ion density estimation at the high pressure.

Thus, the transport length is important parameter to determine the VDF at the extraction region.

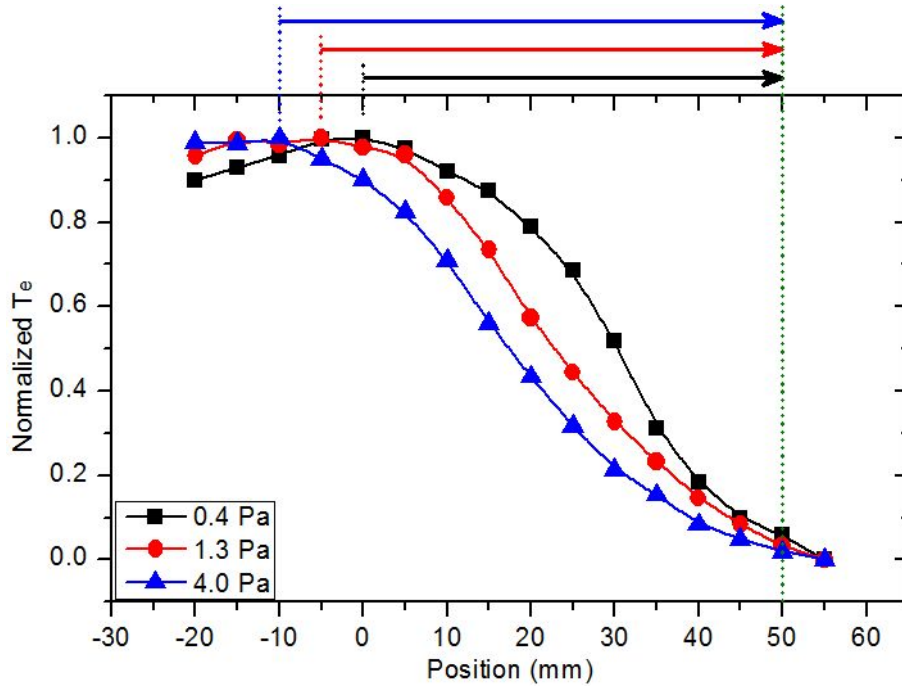


Figure 5.6. Variation of the transport length according to the pressure.

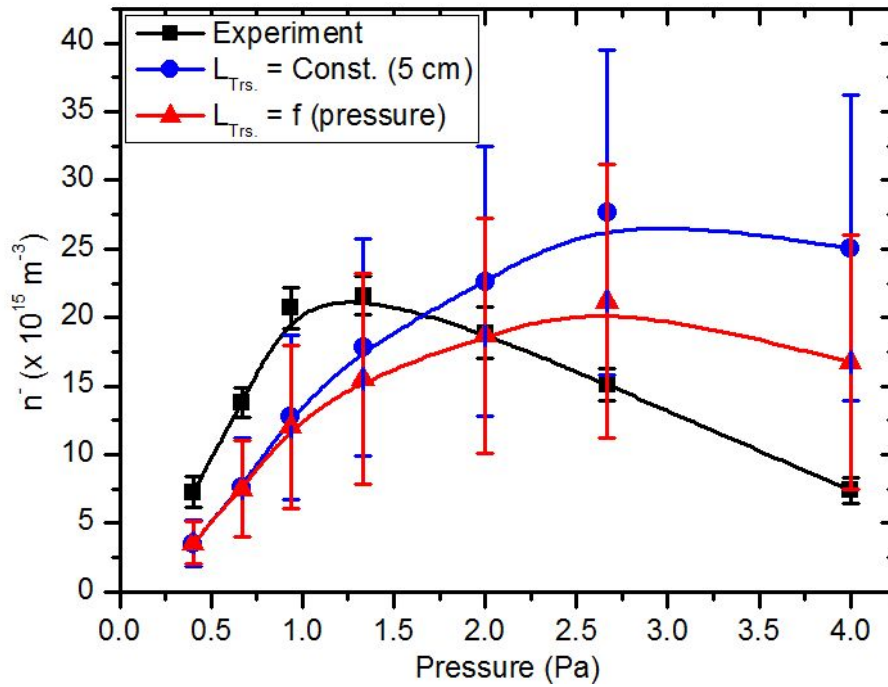


Figure 5.7. The negative ion density calculation with constant transport length and the transport length depending on the pressure.

Finally, the electron temperature and density are set as function of the position in the 1-D model, to reflect more realistic circumstance of the negative ion source. The electron temperature is fitted by an exponential function and the density is fitted by a polynomial function. The calculation is conducted on the two pressure cases which are 1.3 and 4 Pa. The calculation results shift close to the experimental value at both cases.

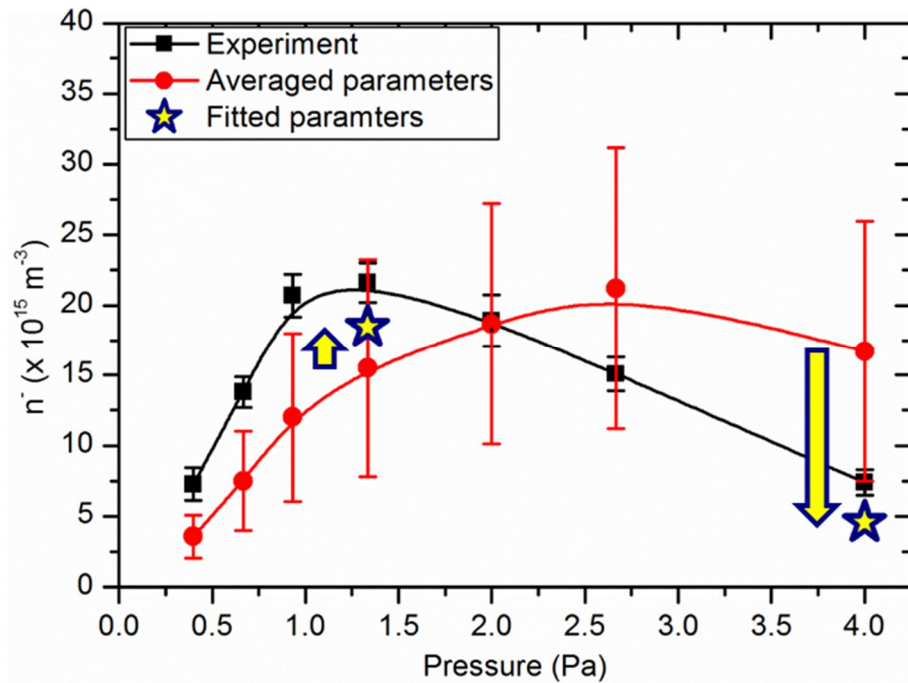


Figure 5.8. The negative ion density calculation with the fitted plasma parameters.

Therefore, 1-D model can surely estimate the negative ion density with properly set parameters such as the transport length and the plasma parameters. Main variables determine the VDF at the extraction region are the effective mean free path and the transport length. The effective mean free path is determined by the plasma parameters. Another important variable is the transport length which is mainly determined by the plasma source geometry and adjusted by the plasma parameter profile. The VDF should be arrived at the extraction region before too

relaxed, because the aim of the negative ion source is the enhancement of the negative ion production. In order to transfer the vibrationally excited molecule efficiently, the effective mean free path should be elongated and the transport length should be shortened. In order to elongate the effective mean free path, the negative ion source should be operated at the low pressure with high electron temperature. However, the electron temperature at extraction region is too raised at low operating pressure. Thus the magnetic filter becomes important to reduce the electron temperature at the extraction region. There are two methods to enhance the magnetic field filtering effect. If the product of the filter strength and filter thickness, $\int Bdl$, is sustained as the constant, it is possible to enhance the filter strength with short filter thickness or broaden the filter thickness with weak filter strength. However, if the filter thickness is broadened, it elongates the transport length. Thus, it is efficient that the magnetic field is strongly generated with the short thickness. The experiment to show the effect of the magnetic filter structure was conducted on the ion source of TRIUMF at Canada [65]. They tried several types of the filter magnet arrangement to find optimized filter structure. The representative arrangements are shown in Figure 5.9.

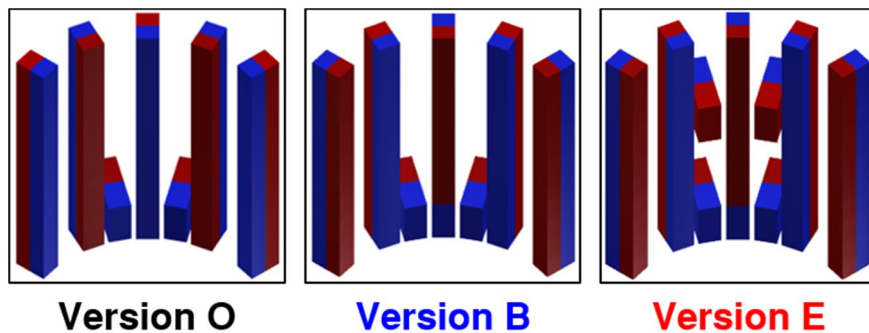


Figure 5.9. Filter magnet arrangement fabricated at TRIUMF.

The version B was designed to enhance the filter magnetic field instead of the

version O. In the version B, the 5 magnets have same polarity at the extraction region including the cusp magnets. In addition, they employed the version E to reduce the thickness of the filter. In the version E, anti-polar magnets are allocated above the filter magnet and between the cusp magnets. The negative ion current is introduced in Figure 5.10.

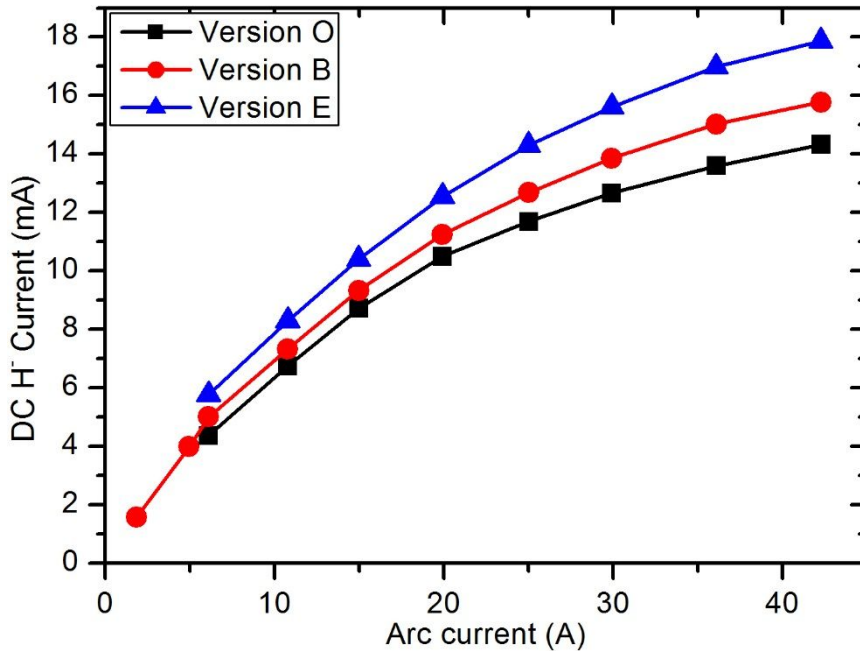


Figure 5.10. Dependence of the negative ion current on the filter magnet structure [65].

The negative ion current increased as the filter is strengthened. Also, the strong field with thin magnetic filter was most efficient. That is, the magnetic field should be generated right strength in the short region. This experiment result was introduced but was not clearly explained in reference [65]. However, this work surely explains the dependency of the negative ion density on the magnetic filter structure, utilizing the vibrational relaxation determined by the effective mean free path and transport length.

5.2. Degree of Dissociation and Negative Ion Density

As of now, the kinetics on the hydrogen molecule is described focused on the vibrationally excited molecule. However, there is an important and basic parameter related with the hydrogen molecule. This is a degree of dissociation. The hydrogen atom is main source of the V-T relaxation and the destruction of the negative ion, while the hydrogen molecule is source material of the negative ion production. Thus, the low degree of dissociation is favored in the negative ion source.

The degree of dissociation can be measured by the optical diagnostics [22]. The H- γ and Fulcher- α are representative spectrum emitted by the hydrogen atom and the molecule, respectively. Thus, the intensity ratio of these spectrum reflects the density ratio of the hydrogen atom and the molecule. The mathematical relation between the intensity ratio and the density ratio is proposed in the reference [22], as follow

$$\frac{I_{\gamma}}{I_{Ful.}} = \frac{X_{\gamma}^{eff}}{X_{Ful.}^{eff}} \frac{n_H}{n_{H_2}}. \quad (5.3)$$

where I_{γ} is the intensity of H- γ and $X_{\gamma}^{eff} / X_{Ful.}^{eff}$ is the ratio between the effective emission rates for the H- γ and Fulcher- α band, which is calculated to be ~ 1.3 [22]. $I_{Ful.}$ is the intensity of the Fulcher band spectrum is defined as

$$I_{Ful.} = \sum_{v=0}^3 \sum_{J=1}^5 I_{a,v,J}^{d,v,J}. \quad (5.4)$$

The relationship between the neutral particle density ratio and the degree of dissociation is expressed as

$$(\text{Degree of dissociation}) = \frac{0.5n_H/n_{H_2}}{1+0.5n_H/n_{H_2}}. \quad (5.5)$$

However, since the difference in the wavelengths of H- γ (434.05 nm) and Fulcher- α band spectrum (600-640 nm) is quite large, a wide-range spectrometer covering over ~ 200 nm is required for this measurement. However, it is recognized that most of wide-range spectrometers have too low spectral resolution to identify the individual line spectra of Fulcher- α band. Thus, it is developed that a new method for determining the degree of dissociation in hydrogen plasmas using wide-range spectrum covering from an atomic H- γ line to molecular Fulcher- α band [66]. In order to resolve the inaccuracy of intensity measurement of the Fulcher- α band induced by the low spectral resolution, a synthetic spectrum technique is introduced. Detail of this method is introduced in Appendix A.

The degree of dissociations measured by the optical method and calculated by the developed model are compared in Figure 5.11. The degree of dissociation decrease as increase of the pressure. Because the dissociation of the hydrogen molecule strongly depends on the electron temperature at the electron temperature range sustained in the present negative ion source.

In previous section, it is mentioned that the negative ion source should be operated with the low pressure and the proper magnetic filter. However, the negative ion density cannot increase unlimitedly as decrease of the pressure, because the high dissociation degree restricts the negative ion production at the low pressure with the high electron temperature. Thus, there should be an optimum pressure maximizing the negative ion density. It was already reported that the optimum pressure of the negative ion source depended the ion source type and operating condition such as the pressure and discharge power [2, 67, 68]. However, the clear explanation was not in these references, except that a short comment on a relation between vibrationally excited molecule and negative ion density. Thus, this

work explains clearly the reason why the optimum pressure exists.

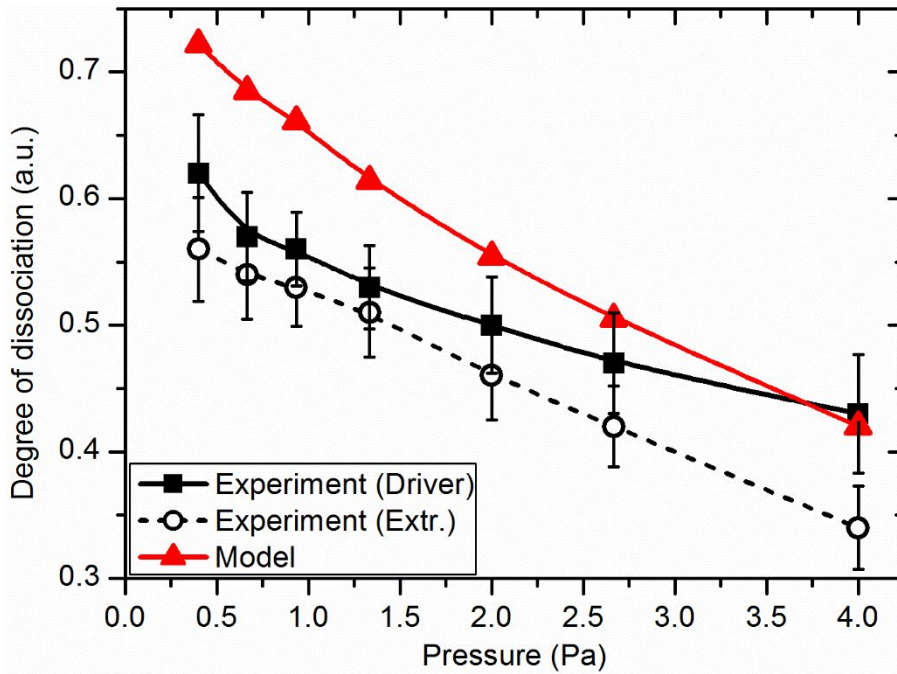


Figure 5.11. Degree of dissociation in long chamber negative ion source discharged by 700 W RF power.

Also, the degree of dissociation depends on the electron density. In order to investigate the effect of the electron density, a variation of the negative ion density and degree of dissociation are compared according to the RF power with the fixed pressure at the optimum pressure, 1.3 Pa. As depicted in Figure 5.12, in spite of the increase of the electron density according to the RF power, the negative ion density increases and becomes saturated. This tendency of the negative ion on the RF power is similar with other work [67, 69]. That is, an optimum RF power efficiency for the negative ion production exists, because the degree of dissociation increases according to the RF power. Therefore, it is verified that the negative ion density is closely related with the degree of dissociation.

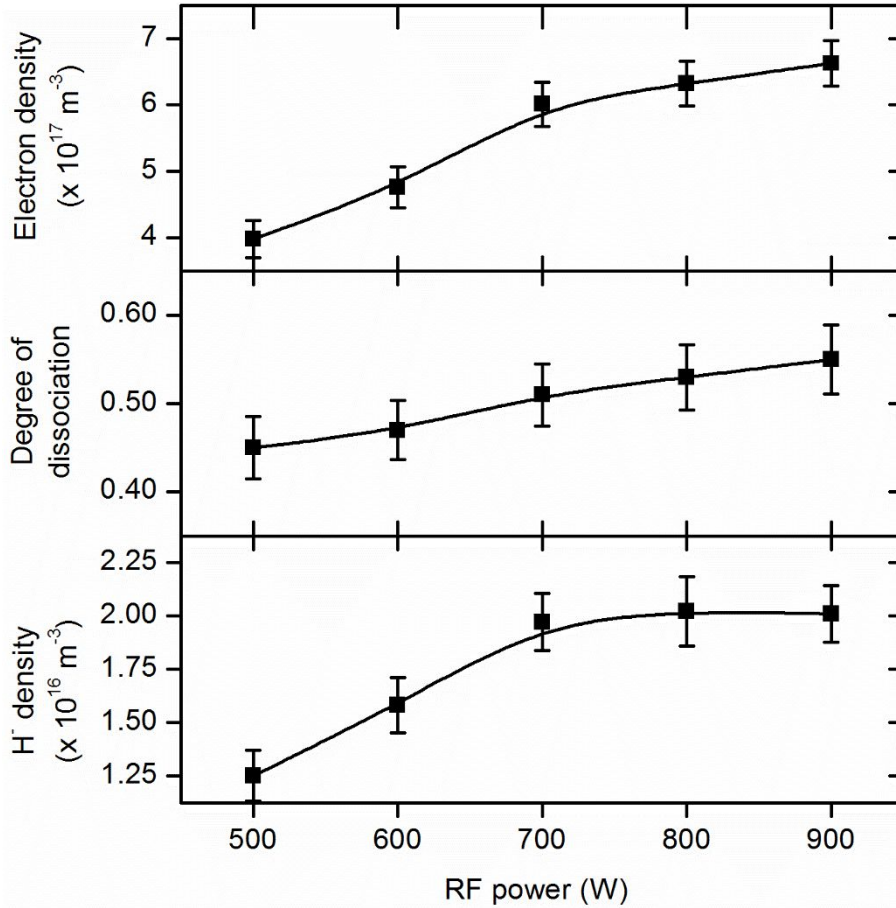


Figure 5.12. Dependency of the electron density, degree of dissociation and negative ion density on the RF power. In spite of the increase of the electron density, the negative ion density increases and becomes saturated. Thus, the ion source has the optimum RF power efficiency, because the degree of dissociation increases too.

Chapter 6. Conclusion

The negative ion source in Seoul National University has been developed and improved over ten years. A feature of this negative ion source is that it adopts the volume production mechanism which produces the negative ion via a dissociative electron attachment (DA) reaction with a vibrationally excited hydrogen molecule and a low energy electron. Thus, in order to enhance efficiency of the volume production, it is important to produce vibrationally excited molecules by high energy electron and then negative ions by low energy electron in a single ion source. It requires a magnetic filter field perpendicular to the axis of the ion source to generate a large gradient of the electron temperature between a driver region and an extraction region. High energy electrons in the driver region maintain a discharge and efficiently excite vibrational states of the molecule. Subsequently, low energy electrons at the extraction region generate negative ions from the vibrationally excited molecules via DA reaction and prevent destruction of the negative ion by an electron impact detachment. This study is devoted to analyze the kinetics of the vibrationally excited molecule in the magnetically filtered hydrogen negative ion source.

Study on vibrationally excited hydrogen molecule is a key element to understand the negative ion source, because highly excited molecules mainly contribute the negative ion production via dissociative electron attachment reaction. However, diagnostics such as Fulcher- α spectroscopy could not give direct information on the higher vibrational states. In order to complement the limitation of the VDF diagnostics, zero-dimensional VDF model has been developed. From the zero-D model, it is confirmed that the VDF in the present negative ion source is in a non-Boltzmann distribution which requires a special treatment of the Fulcher- α spectroscopy for the VDF determination. Also, the estimated Fulcher- α spectrum

by the lower vibrational states of the non-Boltzmann distribution is well matched with the measured spectrum. Though the zero-D VDF model successfully identifies the relationship between the VDF and the Fulcher- α spectrum, the negative ion density estimation from the zero-D model is still deviated from that of the laser photo-detachment diagnostics. Thus, this work extends the zero-D model to one-dimensional model, to account for the transport of the hydrogen molecule and variation of VDF during the transport.

The 1-D model is verified by comparison with the diagnostic results obtained from the Fulcher- α spectroscopy and laser photo-detachment. It is confirmed that 1-D model can improve the accuracy of the negative ion density estimation by including the consideration on the vibrational relaxation of hydrogen molecule in the magnetically filtered ion source. The vibrational relaxation is affected by the operating pressure and the chamber geometry which determine the effective mean free path and the transport length, respectively. Thus, in order to enhance the negative ion production, the negative ion source should be operated under the condition satisfying that the effective mean free path is sustained longer than the transport length. One of the solution satisfying this condition is that the negative ion source should be operated at the lower pressure and equipped with strong and thin magnetic field. Also, even in this case, it is identified that the negative ion production can be affected by the degree of dissociation.

Thus, this study contributes to the characterization of the negative ion source by understanding the kinetics of the hydrogen molecule.

Appendix

A. Determination of Degree of Dissociation with Wide-Range Spectrograph

There are some kinds of diagnostic methods for the degree of dissociation in hydrogen plasmas. An actinometry utilizing noble gases as a tracer has been widely utilized to measure the number density of ground-state hydrogen atoms. However, this method can be applicable to only limited plasma conditions due to the difficulties in choice of the trace gas and the contamination to the plasma source [70]. A laser absorption spectroscopy has been also used to measure the number density of ground-state hydrogen atoms. However, the laser-aided diagnostic system is quite complicated and expensive so that it is unfavorable for monitoring of plasma sources in a simple way. The simplest and easiest way to measure the degree of dissociation is to use a passive optical emission spectroscopy (OES) method [22]. In this method, a collisional-radiative (CR) model which correlates the emission spectrum with the plasma parameters is necessary. Using their CR model, Fantz *et al.* showed that the intensity ratio of H- γ and the Fulcher- α band spectrum is the most suitable for the determination of the degree of dissociation. Since the difference in the wavelengths of H- γ (434.05 nm) and Fulcher- α band spectrum (600-640 nm) is quite large, a wide-range spectrometer covering over \sim 200 nm is required for this measurement. Thus, in this work, the wide-range spectrometer manufactured by Ocean optics Inc. (model: HR4000CG-UV-NIR) is employed. This spectrometer can measure a spectrum from 200 to 1100 nm. The spectrum measured by the wide-range spectrometer is presented in 오류! 참조 원본을 찾을 수 없습니다. and Figure A.2. It can be seen that the wavelength

coverage is good enough to measure the intensities of H- γ and Fulcher- α band spectrum at the same time. However, the problem is that the spectrum of the Fulcher- α band cannot be resolved sufficiently for analyzing each spectral line. As shown in Figure A.2, the spectra measured by the wide-range miniature spectrometer (denoted as ‘WR-spectrometer’) for each vibrational state are much less resolved than those obtained by the high resolution spectrometer (denoted as ‘HR-spectrometer’) which was introduced in section 2.4. The instrumental broadening of the wide-range spectrometer is ~ 0.6 nm by a mercury-argon light source (579 nm, mercury line and 696.5 nm argon line), and this broadening is about ten times larger than that of the high resolution spectrometer. Thus, the intensity of the respective rotational line cannot be clearly defined from the wide-range spectrum and it is difficult to determine the Fulcher- α band spectrum intensity which is expressed as equation 5.4 and an essential parameter to determine the degree of dissociation.

Consequently, in this work, it is developed that a new method for determining the degree of dissociation in hydrogen plasmas using wide-range spectrum covering from an atomic H- γ line to molecular Fulcher- α band [66]. In order to resolve the inaccuracy of intensity measurement of the Fulcher- α band induced by the low spectral resolution, a synthetic spectrum technique is introduced. Also, the rotational temperature determined from the synthesized 0-0 Fulcher transition is used to estimate the intensities of vibrationally-excited states so as to improve the accuracy of Fulcher- α intensity. They are introduced in here that the newly proposed method and its verification by comparing with the experimental results obtained from a high resolution spectrometer.

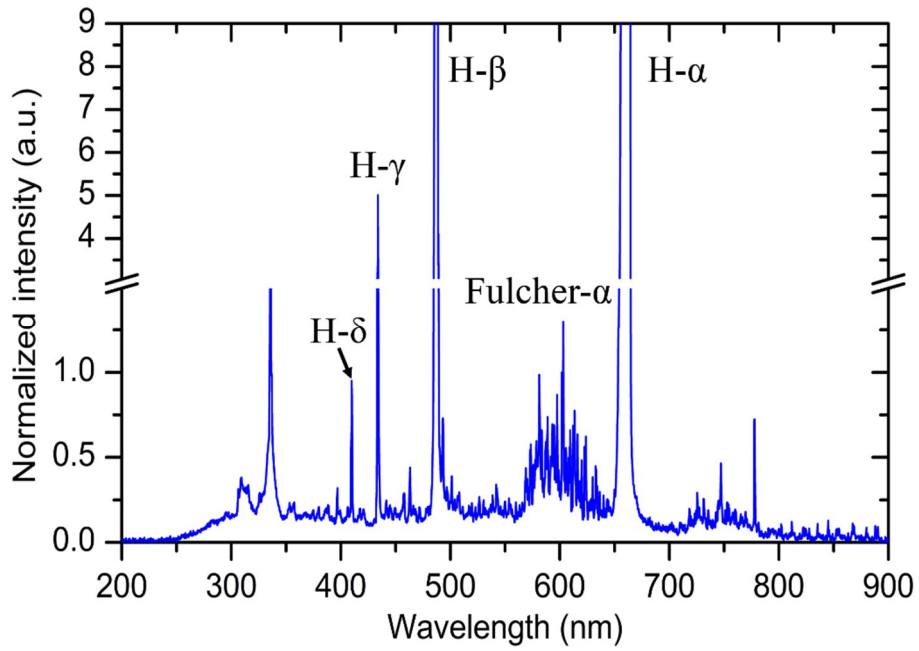


Figure A.1. Full range spectrum of the hydrogen plasma measured by wide-range spectrometer.

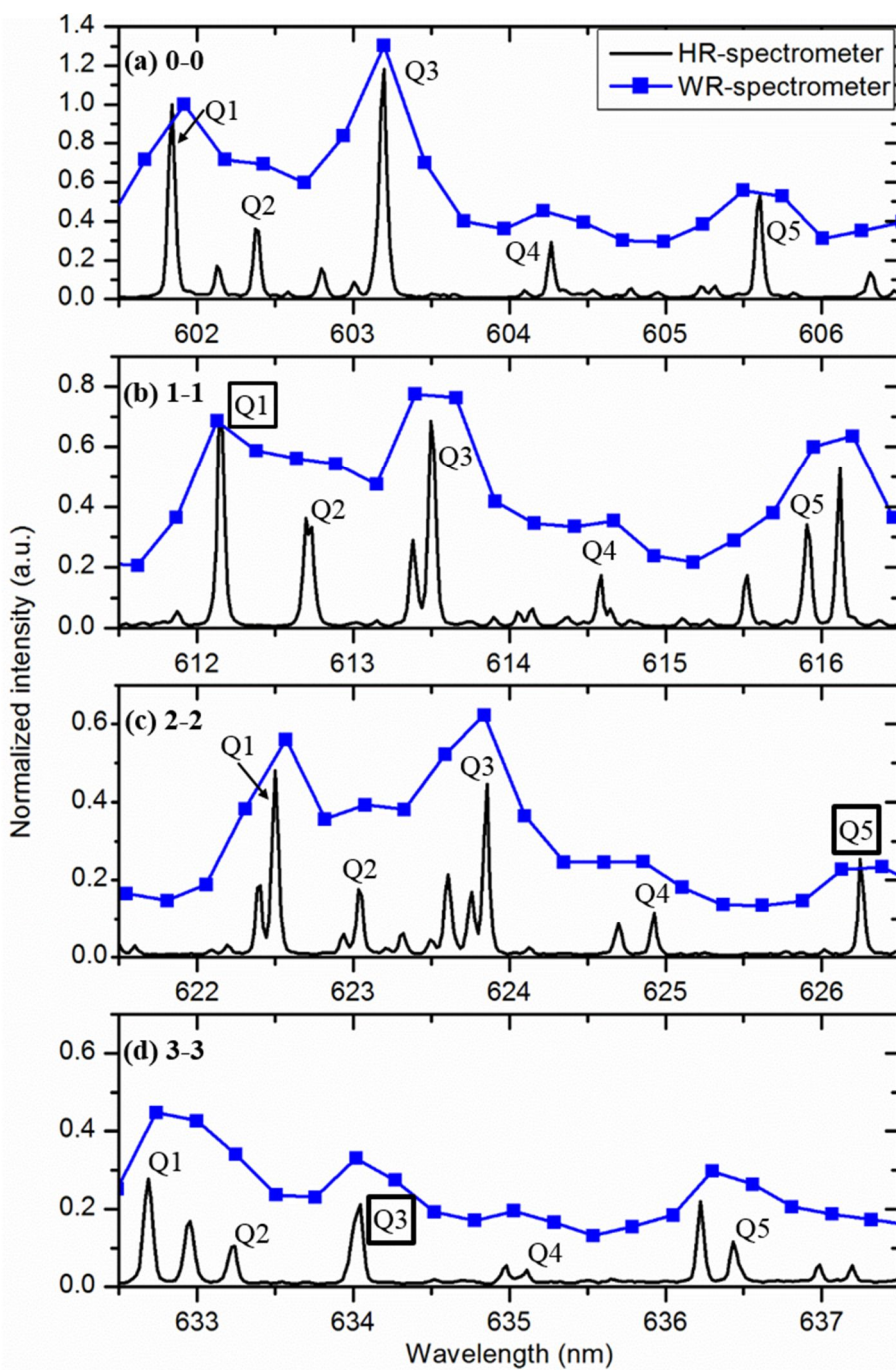


Figure A.2. Rescaled graphs of each vibrational states (a: 0-0, b: 1-1, c: 2-2, d: 3-3) spectra of Fulcher- α transition. For comparison, the high resolution spectrometer data are also plotted

If following assumptions are satisfied, a synthetic spectrum method can be utilized in the determination of the degree of dissociation.

Assumption:

1. The respective rotational lines are in the Boltzmann distribution.
2. There is only the instrumental broadening.
3. The instrumental broadenings of every rotational lines are same.

The synthetic spectrum method is a numerical method estimating a convoluted and superposed spectrum in consideration with an instrumental broadening and a theoretical spectrum. A single spectral line with the broadening is fitted with a normalized Gaussian profile [71],

$$G(\lambda) = \frac{2}{\Delta\sqrt{\pi}} \exp\left\{-\left(\frac{\lambda - \lambda_0}{\Delta/2}\right)^2\right\}, \quad (\text{A.1})$$

where Δ is the full width at 1/e of the maximum intensity at a wavelength λ_0 . The Δ is determined by the value measured from the Hg-Ar lamp. The Fulcher band spectrum of each vibrational state can be synthesized as the superposition of the respective rotational lines whose spectral line shapes are expressed as equation A.1 and intensity distribution is calculated by equation 2.11. Finally, the rotational temperature is determined by the least squared fitting of the synthetic spectrum and the spectrometer signal. In order to fit the synthesized spectrum to the spectrum of the wide-range spectrometer, the synthesized spectrum is adjusted to have the same spectral resolution of the wide-range spectrometer. Also, a background of the spectrum of the spectrometer is eliminated before the fitting. Thus, the broadened and superposed spectrum like Figure A.2(a) can be fitted. A spectrum fitting program is established on the MATLAB[®]. The example of the fitting is presented in Figure A.3.

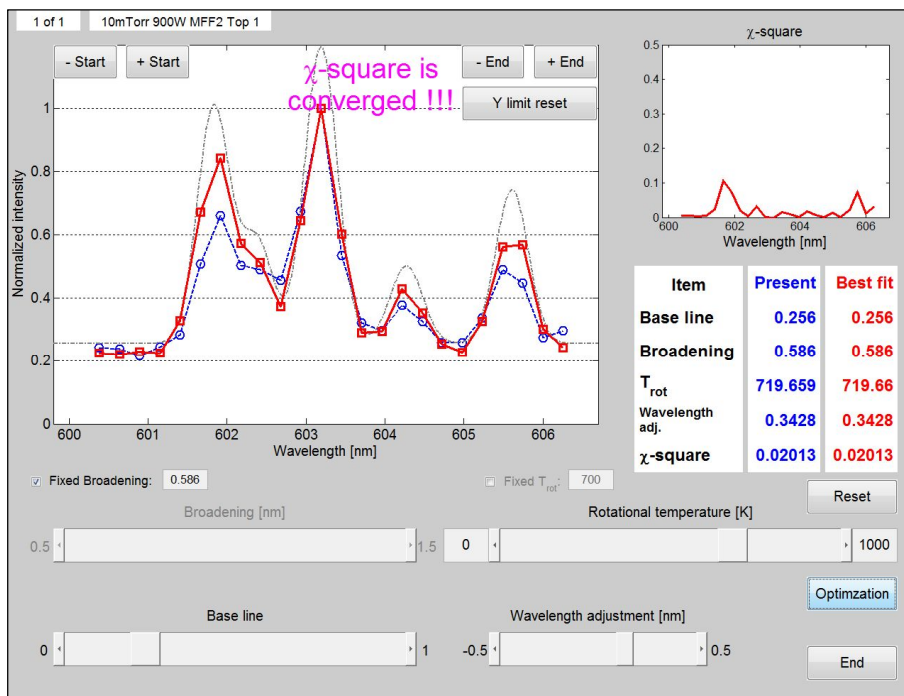


Figure A.3. Example of synthesizing the broadened and superposed spectrum by homemade MATLAB[®] code.

The Boltzmann plot and the rotational temperature determined by the synthetic spectrum method is depicted in Figure A.4, and the rotational temperature determined by the high resolution spectrometer and the wide-range spectrometer without the synthetic spectrum method are compared. In Figure A.2(a), it is observed that the low-resolution spectrum obtained from the miniature spectrometer is considerably deviated from the actual spectrum. Hence, its Boltzmann plot not only underestimates the rotational temperature by 20%, but also does not show a good linearity, as shown Figure A.4. This poor accuracy in determining the rotational temperature can be greatly improved by using the synthetic spectrum method. Since the synthetic spectrum method is based on the Boltzmann equilibrium for Fulcher band spectrum, the optimized spectrum (denoted as ‘*Synth. spectrum*’) shows a perfect linearity, as shown in Figure A.4. In addition, the accuracy in determining the rotational temperature is greatly

improved, showing an error less than 5%. Such improvements in the determination of rotational temperature are confirmed in all experimental data obtained for our experimental conditions. Therefore, it is concluded that the rotational temperature can be determined with an error less than 5% by applying the synthetic spectrum method to the broadened and superposed 0-0 Fulcher band spectrum.

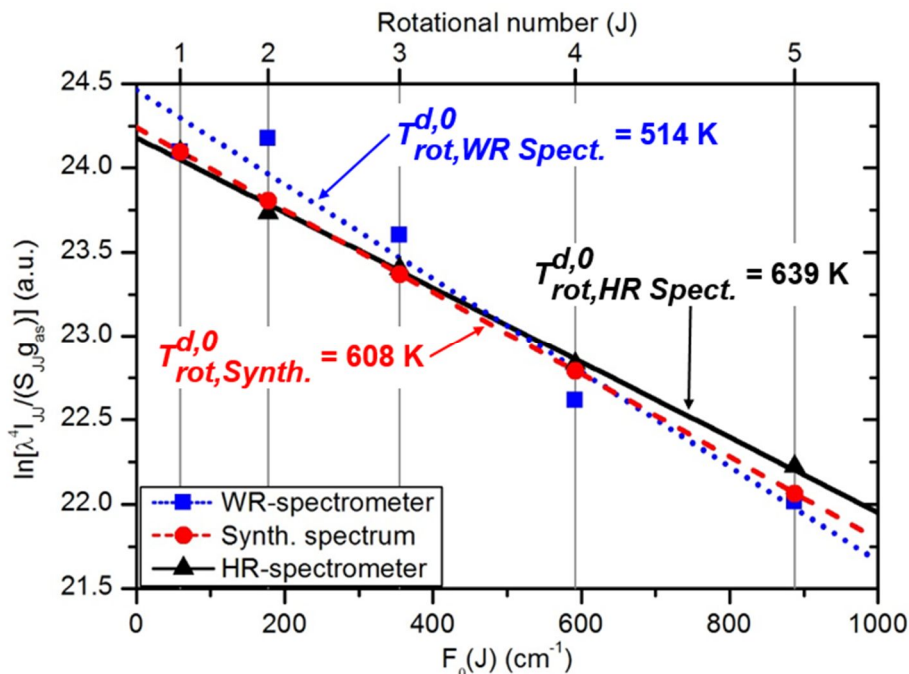


Figure A.4. Boltzmann plot and Rotational temperature of Fulcher- α 0-0 band spectrum.

However, it is found that the synthetic spectrum method is not useful to determine the rotational temperatures of vibrationally-excited states ($v \geq 1$), because the synthesized Fulcher band spectra of the excited states are severely distorted by adjacent lines. For example, as shown in Figure A.5, the Q3 line is superposed on other Q1 line of $g^3\Sigma_g^+ \rightarrow c^3\Pi_u$ transition and the Q5 line is also greatly affected by the adjacent lines of R3 and P5. The effects of the adjacent lines result in a large error for the determination of rotational temperature from the synthesized spectrum. As depicted in Figure A.6, the rotational temperature

estimated by the Fulcher 1-1 spectrum with the synthetic spectrum method shows an error of 50% compared to the value measured by the high resolution spectrometer. Such a tendency is also found for higher vibrational states of 2-2 and 3-3 Fulcher band spectra. From the above consideration on the accuracy of rotational temperatures obtained from Fulcher band spectra, it is obvious that the synthetic spectrum method is only applicable to determine the rotational temperature of the 0-0 Fulcher- α spectrum.

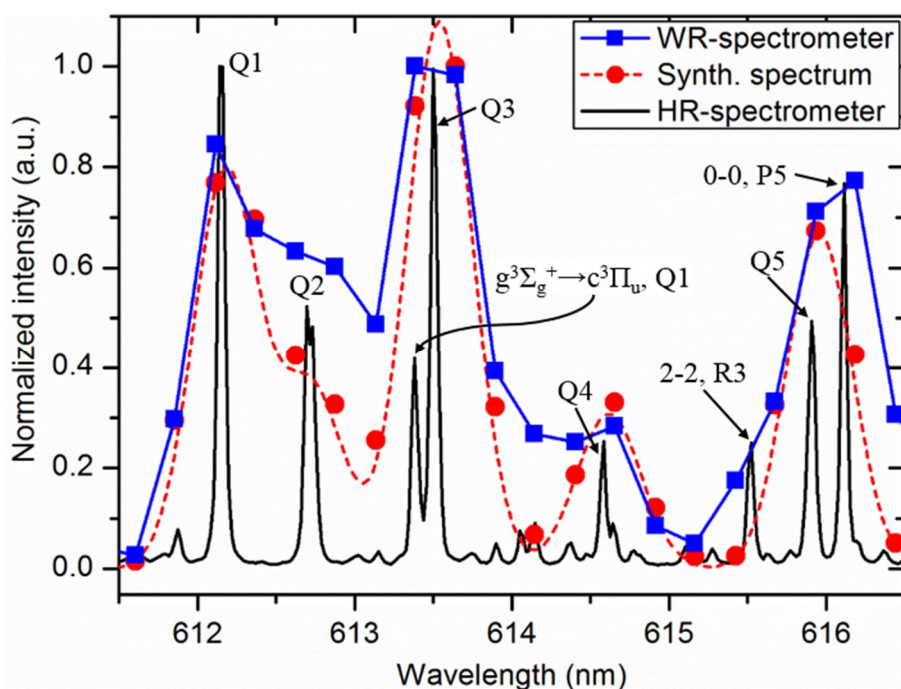


Figure A.5. Fulcher- α 1-1 band spectrum.

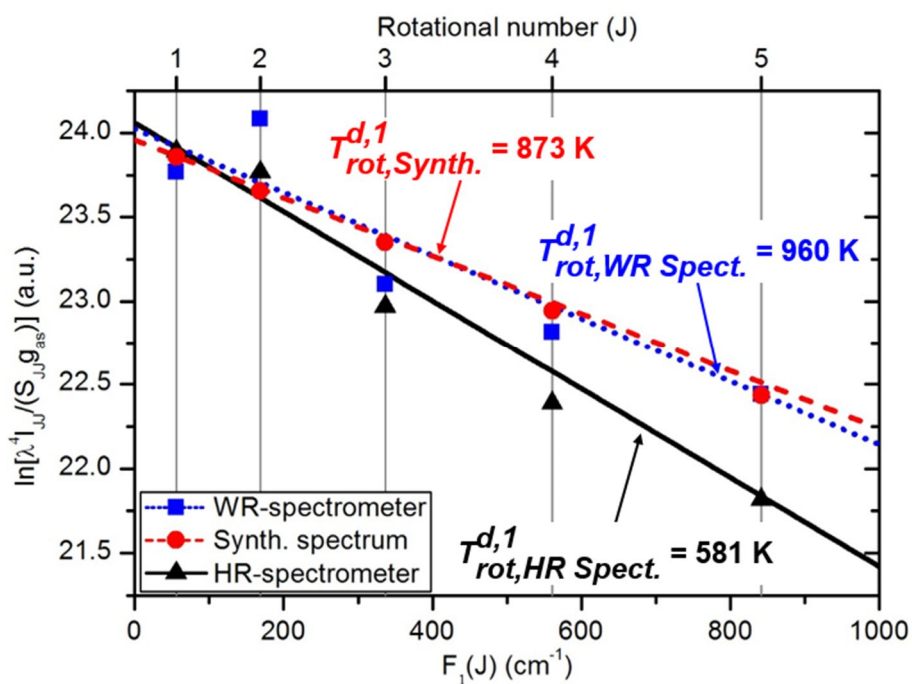


Figure A.6. Boltzmann plot and Rotational temperature of Fulcher- α 1-1 band spectrum.

However, the rotational temperatures for vibrationally-excited states can be substituted to the rotational temperature determined by the 0-0 Fulcher transition, if the rotational temperatures obtained from vibrationally-excited states are the same as that from the ground state. In Figure A.7, they are compared that the Boltzmann plots and the rotational temperatures for vibrational states $\nu = 0 - 3$ measured by the high resolution spectrometer. It is revealed that the rotational temperatures determined from the vibrationally-excited states are well matched to that from the ground-state within an error of 15% for our experimental conditions except for $\nu = 3$ state. Although this error is still large, this method is much better than utilizing rotational temperatures directly obtained from vibrationally-excited Fulcher band spectra. Note that the error from the $\nu = 3$ state is reduced considerably in the intensity estimation because the intensity of 3-3 transition is the weakest in the

whole Fulcher band spectra.

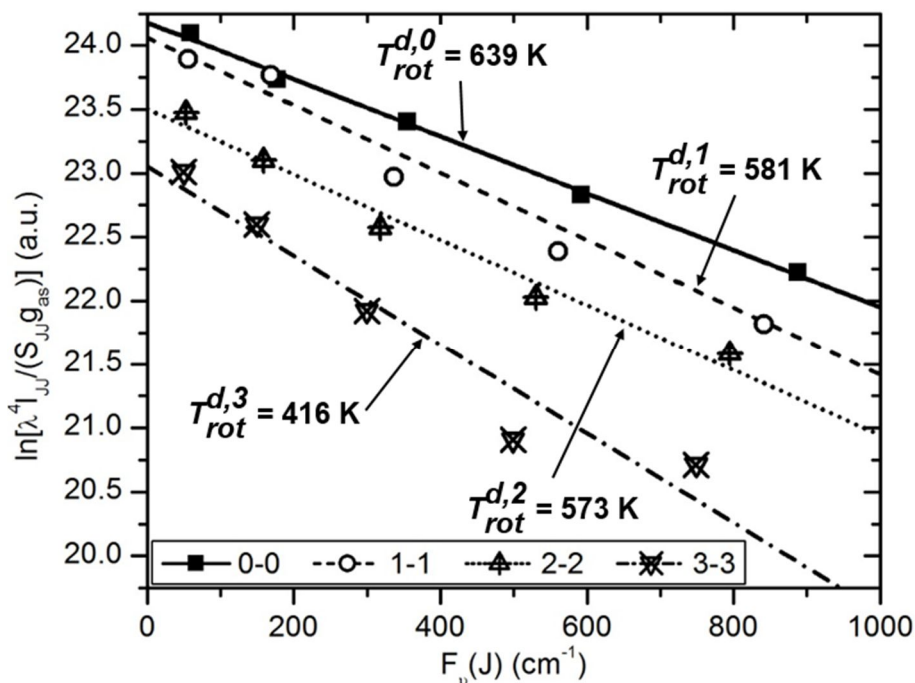


Figure A.7. Boltzmann plots for vibrationally-excited Fulcher- α spectra measured by the high resolution spectrometer.

Thus, in order to obtain more reasonable intensity, the rotational temperature determined by the 0-0 spectrum, $T_{rot}^{d,0}$, is introduced into the intensity estimation. Provided that the rotational temperature is the same for every vibrational states and there is a rotational line which are less affected by other spectra in 1-1, 2-2 and 3-3 bands, the intensity of the remained lines can be calculated by equation 2.11 and the synthetic spectrum method. The remained lines are synthesized by the given rotational temperature and the known intensity of the reference line. The Q1, Q5 and Q3 lines in 1-1, 2-2 and 3-3 Fulcher transition, respectively, are less affected by other spectra. These reference lines are depicted as square text boxes in Figure A.2(b) – Figure A.2(d). Therefore, the Fulcher- α spectrum intensity can be determined, although the low resolution spectrometer cannot resolve the individual

rotational lines in the Fulcher- α band spectrum. This new method is simple but powerful because this method can determine the degree of dissociation and the rotational temperature simultaneously from poorly-resolved spectra obtained by a simple and cost-effective optical diagnostics system.

The procedure of the new method for degree of dissociation measurement is summarized as followings:

1. The spectrum from H- γ to Fulcher- α band is measured by the wide wavelength range spectrometer.
2. The rotational temperature of ($d^3\Pi_u^-, v=0$)-state is determined from the 5 rotational lines ($J=1\sim 5$) in Fulcher 0-0 band whose spectral resolution is improved by the synthetic spectrum method.
3. The intensities of 5 rotational lines in respective vibrational bands, 1-1, 2-2 and 3-3, are calculated by equation 2.11, the synthetic spectrum method using the rotational temperature obtained in the step (2) and the measured intensity of the reference line which are Q1, Q5 and Q3 line in 1-1, 2-2 and 3-3 band, respectively.
4. The degree of dissociation is obtained by the intensity ratio between H- γ and the Fulcher- α spectrum.

In Figure A.8, the rotational temperatures determined from the synthesized spectra of the broadened 0-0 Fulcher bands are compared with those obtained from the high resolution spectrum for various operating pressures depending on RF power. For all experimental conditions, the rotational temperatures determined from the synthesized spectra agree well with those from the high resolution spectrometer within the error of 10%. It is noted that the error range increases with RF power and gas pressure because the actual spectrum is more influenced by the lines excluded from the synthetic spectrum method. This increases the fitting error of the synthetic spectrum method and thus reduces the accuracy of rotational

temperature. Based on the rotational temperatures of 0-0 transition shown in Figure A.8 and the intensities of the reference lines of each state, the intensity of the Fulcher- α band spectrum is estimated from equation 5.4. Then, the degrees of dissociation are determined from equation 5.3 and 5.5 for various experimental conditions, as shown in Figure A.9. It is clearly observed that the degree of dissociation increases with increasing the RF power and decreasing the gas pressure, as previously reported by Fantz *et al* [22]. When compared to the degrees of dissociation determined directly from the miniature spectrometer, it is obvious that the accuracy of dissociation degree measurement is greatly improved by the new method developed in this work. Some discrepancies in data between the high resolution spectrometer and the synthetic method are induced by the measurement accuracy on the intensity of the lines which is set as the reference line. Note that this discrepancy cannot be diminished as long as unless all the branches of the Fulcher transition and other electronic transitions are synthesized.

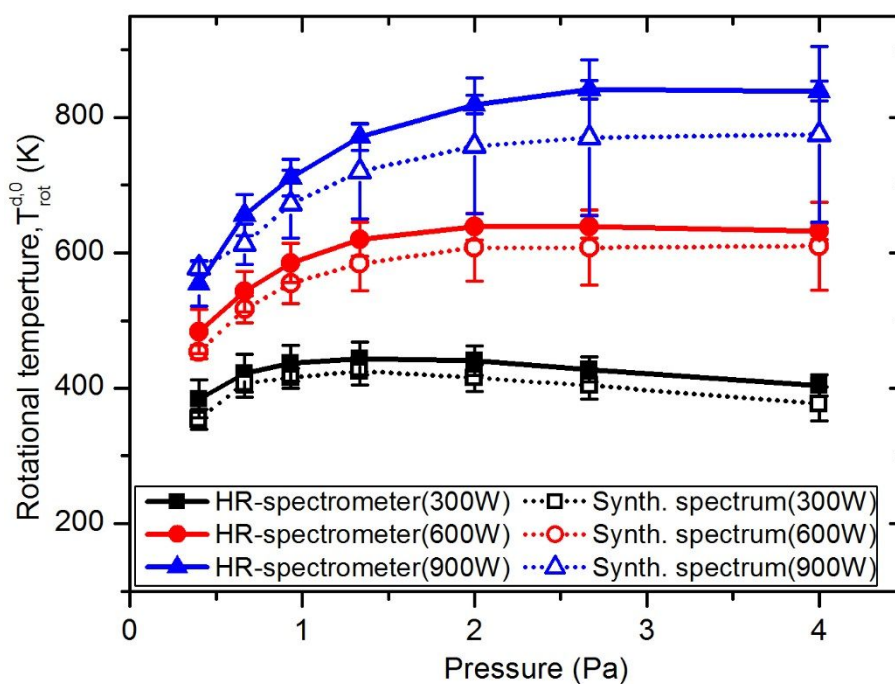


Figure A.8. Rotational temperatures determined from the 0-0 Fulcher band

spectra measured by the high resolution spectrometer and the low resolution spectrometer improved by the synthetic spectrum method.

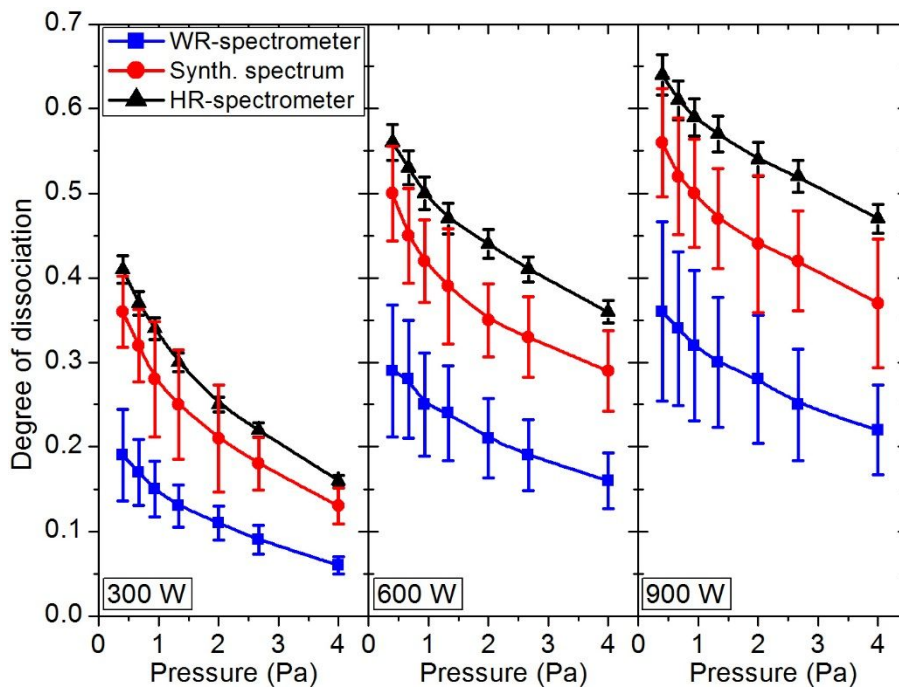


Figure A.9. Degree of dissociation determined by the wide-range spectrum, synthetic spectrum method, and high resolution spectrum.

Bibliography

- [1] R. S. Hemsworth, J. H. Feist, M. Hanada, B. Heinemann, T. Inoue, E. Kussel, A. Krylov, P. Lotte, K. Miyamoto, N. Miyamoto, D. Murdoch, A. Nagase, Y. Ohara, Y. Okumura, J. Paméla, A. Panasenkov, K. Shibata, M. Tanii, and M. Watson, "Neutral beams for ITER," *Review of Scientific Instruments* **67** (3), 1120-1125 (1996).
- [2] M. Bacal and M. Wada, "Negative hydrogen ion production mechanisms," *Applied Physics Reviews* **2** (2), 021305 (2015).
- [3] C. F. Barnett, "*Collisions of H, H₂, He and Li atoms and ions with atoms and molecules*," ORNL, Oak Ridge, ORNL-6086, 1990.
- [4] C. D. Moak, H. E. Banta, J. N. Thurston, J. W. Johnson, and R. F. King, "Duo Plasmatron ion source for use in accelerators," *Review of Scientific Instruments* **30** (8), 694-699 (1959).
- [5] G. P. Lawrence, R. K. Beauchamp, and J. L. McKibben, "Direct extraction of negative ion beams of good intensity from a duoplasmatron," *Nuclear Instruments and Methods* **32** (2), 357-359 (1965).
- [6] K. W. Ehlers and K. N. Leung, "Multicusp negative ion source," *Review of Scientific Instruments* **51** (6), 721-727 (1980).
- [7] E. Nicolopoulou, M. Bacal, and H. J. Doucet, "Equilibrium density of H⁻ in a low-pressure hydrogen plasma," *Journal De Physique* **38** (11), 1399-1404 (1977).
- [8] T. F. O'Malley, "Theory of dissociative attachment," *Physical Review* **150** (1), 14-29 (1966).

- [9] J. N. Bardsley, "Configuration interaction in the continuum states of molecules," *Journal of Physics B: Atomic and Molecular Physics* **1** (3), 349-364 (1968).
- [10] G. J. Schulz, "Resonances in electron impact on diatomic molecules," *Reviews of Modern Physics* **45** (3), 423-486 (1973).
- [11] J. M. Wadehra and J. N. Bardsley, "Vibrational- and rotational-state dependence of dissociative attachment in e-H₂ collisions," *Physical Review Letters* **41** (26), 1795-1798 (1978).
- [12] M. Allan and S. F. Wong, "Effect of vibrational and rotational excitation on dissociative attachment in hydrogen," *Physical Review Letters* **41** (26), 1791-1794 (1978).
- [13] T. E. Sharp, "Potential-energy curves for molecular hydrogen and its ions," *Atomic Data and Nuclear Data Tables* **2**, 119-169 (1970).
- [14] D. Rapp, T. E. Sharp, and D. D. Briglia, "Large isotope effect in the formation of H⁻ or D⁻ by electron impact on H₂, HD, and D₂," *Physical Review Letters* **14** (14), 533-535 (1965).
- [15] R. K. Janev, D. Reiter, and U. Samm, "*Collision processes in low-temperature hydrogen plasmas*," Forschungszentrum Jülich, Jülich, Jül-4105, 2003.
- [16] A. Fridman and L. A. Kennedy, *Plasma physics and engineering*, Taylor & Francis, New York, (2004).
- [17] M. Péalat, J. P. E. Taran, M. Bacal, and F. Hillion, "Rovibrational molecular populations, atoms, and negative ions in H₂ and D₂ magnetic multicusp discharges," *The Journal of Chemical Physics* **82** (11), 4943-4953 (1985).

- [18] P. J. Eenshuistra, A. W. Kleyn, and H. J. Hopman, "Plateau formation in the measured vibrational distribution of hydrogen in a volume source," *Europhysics Letters* **8** (5), 423-427 (1989).
- [19] D. Wagner, B. Dikmen, and H. F. Döbele, "Comparison of atomic and molecular densities and temperatures of deuterium and hydrogen plasmas in a magnetic multipole source," *Plasma Sources Science and Technology* **7** (4), 462-470 (1998).
- [20] T. Mosbach, H. M. Katsch, and H. F. Döbele, "*In-situ* diagnostics in plasmas of electronic-ground-state hydrogen molecules in high vibrational and rotational states by laser-induced fluorescence with vacuum-ultraviolet radiation," *Physical Review Letters* **85** (16), 3420-3423 (2000).
- [21] U. Fantz and B. Heger, "Spectroscopic diagnostics of the vibrational population in the ground state of H₂ and D₂ molecules," *Plasma Physics and Controlled Fusion* **40** (12), 2023-2032 (1998).
- [22] U. Fantz, H. Falter, P. Franzen, D. Wunderlich, M. Berger, A. Lorenz, W. Kraus, P. McNeely, R. Riedl, and E. Speth, "Spectroscopy—a powerful diagnostic tool in source development," *Nuclear Fusion* **46** (6), S297-S306 (2006).
- [23] T. Mosbach, "Population dynamics of molecular hydrogen and formation of negative hydrogen ions in a magnetically confined low temperature plasma," *Plasma Sources Science and Technology* **14** (3), 610-622 (2005).
- [24] D. Pagano, C. Gorse, and M. Capitelli, "Modeling multicusp negative-ion sources," *IEEE Transactions on Plasma Science* **35** (5), 1247-1259 (2007).
- [25] S. R. Huh, N. K. Kim, B. K. Jung, K. J. Chung, Y. S. Hwang, and G. H. Kim, "Global model analysis of negative ion generation in low-pressure inductively coupled hydrogen plasmas with bi-Maxwellian electron energy distributions,"

- Physics of Plasmas* **22** (3), 033506 (2015).
- [26] Z. Kiss'ovski, S. Kolev, A. Shivarova, and T. Tsankov, "Expanding plasma region of an inductively driven hydrogen discharge," *IEEE Transactions on Plasma Science* **35** (4), 1149-1155 (2007).
- [27] G. J. M. Hagelaar, G. Fubiani, and J. P. Boeuf, "Model of an inductively coupled negative ion source: I. General model description," *Plasma Sources Science and Technology* **20** (1), 015001 (2011).
- [28] J. P. Boeuf, G. J. M. Hagelaar, P. Sarrailh, G. Fubiani, and N. Kohen, "Model of an inductively coupled negative ion source: II. Application to an ITER type source," *Plasma Sources Science and Technology* **20** (1), 015002 (2011).
- [29] S. Lishev, L. Schiesko, D. Wunderlich, and U. Fantz, "Spatial distribution of the plasma parameters in the RF negative ion source prototype for fusion," *AIP Conference Proceedings* **1655** (1), 040010 (2015).
- [30] B. K. Jung, J. J. Dang, Y. H. An, K. J. Chung, and Y. S. Hwang, "Development of a novel radio-frequency negative hydrogen ion source in conically converging configuration," *Review of Scientific Instruments* **85** (2), 02B112 (2014).
- [31] F. F. Chen, "Langmuir probe analysis for high density plasmas," *Physics of Plasmas* **8** (6), 3029-3041 (2001).
- [32] M. A. Lieberman and A. J. Lichtenberg, *Principles of plasma discharges and materials processing*, (Ed. 2nd), John Wiley & Sons, Hoboken, (2005).
- [33] M. Bacal, "Physics aspects of negative ion sources," *Nuclear Fusion* **46** (6), S250-S259 (2006).
- [34] A. Simon, "Ambipolar diffusion in a magnetic field," *Physical Review* **98** (2),

317-318 (1955).

- [35] L. Schiesko, P. McNeely, P. Franzen, U. Fantz, and N. T. the, "Magnetic field dependence of the plasma properties in a negative hydrogen ion source for fusion," *Plasma Physics and Controlled Fusion* **54** (10), 105002 (2012).
- [36] C. Davide and F. F. Chen, "Cross-field diffusion in low-temperature plasma discharges of finite length," *Plasma Sources Science and Technology* **23** (6), 064001 (2014).
- [37] M. Bacal and G. W. Hamilton, "H⁻ and D⁻ Production in Plasmas," *Physical Review Letters* **42** (23), 1538-1540 (1979).
- [38] M. Bacal, "Photodetachment diagnostic techniques for measuring negative ion densities and temperatures in plasmas," *Review of Scientific Instruments* **71** (11), 3981-4006 (2000).
- [39] M. Nishiura, M. Sasao, and M. Bacal, "H⁻ laser photodetachment at 1064, 532, and 355 nm in plasma," *Journal of Applied Physics* **83** (6), 2944-2949 (1998).
- [40] R. Bleekrode, "A study of the spontaneous emission from CO₂-N₂-He-H₂ laser discharges C³Π_u⁻-B³Π_g emission bands of N₂," *IEEE Journal of Quantum Electronics* **5** (2), 57-60 (1969).
- [41] Z. Qing, D. K. Otorbaev, G. J. H. Brussaard, M. C. M. van de Sanden, and D. C. Schram, "Diagnostics of the magnetized low-pressure hydrogen plasma jet: Molecular regime," *Journal of Applied Physics* **80** (3), 1312-1324 (1996).
- [42] X. Bingjia, K. Shinichiro, K. Shin, and Y. Daisuke, "Rovibrational distribution determination of H₂ in low temperature plasmas by Fulcher-α band spectroscopy," *Plasma Physics and Controlled Fusion* **46** (4), 653-668 (2004).

- [43] D. R. Farley, D. P. Stotler, D. P. Lundberg, and S. A. Cohen, "Modeling of hydrogen ground state rotational and vibrational temperatures in kinetic plasmas," *Journal of Quantitative Spectroscopy and Radiative Transfer* **112** (5), 800-819 (2011).
- [44] G. Herzberg, *Molecular spectra and molecular structure: I. Spectra of diatomic molecules*, (Ed. 2nd), Van Nostrand Reinhold Company, New York, (1950).
- [45] B. P. Lavrov, M. Osiac, A. V. Pipa, and J. Röpcke, "On the spectroscopic detection of neutral species in a low-pressure plasma containing boron and hydrogen," *Plasma Sources Science and Technology* **12** (4), 576-589 (2003).
- [46] S. A. Astashkevich, M. Käning, E. Käning, N. V. Kokina, B. P. Lavrov, A. Ohl, and J. Röpcke, "Radiative characteristics of $3p \Sigma$, Π ; $3d \Pi$, Δ^- states of H_2 and determination of gas temperature of low pressure hydrogen containing plasmas," *Journal of Quantitative Spectroscopy and Radiative Transfer* **56** (5), 725-751 (1996).
- [47] U. Fantz and D. Wunderlich, "Franck–Condon factors, transition probabilities, and radiative lifetimes for hydrogen molecules and their isotopomers," *Atomic Data and Nuclear Data Tables* **92** (6), 853-973 (2006).
- [48] C. Gorse, M. Capitelli, M. Bacal, J. Bretagne, and A. Laganà, "Progress in the non-equilibrium vibrational kinetics of hydrogen in magnetic multicusp H^- ion sources," *Chemical Physics* **117** (2), 177-195 (1987).
- [49] B. Xiao, S. Kado, S. Kajita, D. Yamasaki, and S. Tanaka, "Rovibrational distribution of H_2 in low temperature plasma: the dependence on the plasma parameters," *Journal of Nuclear Materials* **337–339**, 1082-1086 (2005).

- [50] M. J. Park, "A study on a compact hydrogen ion source using helicon plasma," Ph. D. dissertation, Department of nuclear engineering, Seoul national university, Seoul, 2005.
- [51] H. D. Jung, J. Y. Park, K. J. Chung, and Y. S. Hwang, "Development of a high-current helicon ion source with high monatomic fraction for the application of neutron generators," *IEEE Transactions on Plasma Science* **35** (5), 1476-1479 (2007).
- [52] S. Iordanova, T. Paunskas, and A. Pashov, "Spectroscopic study of neutral species in a planar-coil inductive discharge in hydrogen," *Journal of Physics D: Applied Physics* **48** (48), 485204 (2015).
- [53] M. Capitelli, R. Celiberto, F. Esposito, A. Laricchiuta, K. Hassouni, and S. Longo, "Elementary processes and kinetics of H₂ plasmas for different technological applications," *Plasma Sources Science and Technology* **11** (3A), A7 (2002).
- [54] R. Celiberto, R. K. Janev, A. Laricchiuta, M. Capitelli, J. M. Wadehra, and D. E. Atems, "Cross section data for electron-impact inelastic processes of vibrationally excited molecules of hydrogen and its isotopes," *Atomic Data and Nuclear Data Tables* **77** (2), 161-213 (2001).
- [55] R. Celiberto, M. Capitelli, and A. Laricchiuta, "Towards a Cross Section Database of Excited Atomic and Molecular Hydrogen," *Physica Scripta* **T96**, 32-44 (2002).
- [56] *Vibrationally resolved excitation and charge transfer for collisions among vibrationally excited H₂ with H⁺ and vibrationally excited H₂⁺ with H.* ORNL-Controlled fusion atomic data center. Available: <http://www-cfadc.phy.ornl.gov/h2mol/homeh.html>
- [57] M. E. Mandy and P. G. Martin, "State-to-state rate coefficients for H+H₂," *The*

- [58] A. A. Matveyev and V. P. Silakov, "Kinetic processes in a highly-ionized non-equilibrium hydrogen plasma," *Plasma Sources Science and Technology* **4** (4), 606-617 (1995).
- [59] K. J. Chung, B. K. Jung, Y. An, J. J. Dang, and Y. S. Hwang, "Effects of discharge chamber length on the negative ion generation in volume-produced negative hydrogen ion source," *Review of Scientific Instruments* **85** (2), 02B119 (2014).
- [60] R. B. Bird, W. E. Stewart, and E. N. Lightfoot, *Transport Phenomena*, (Ed. 2nd), John Wiley & Sons, New York, (2002).
- [61] C. Gorse and M. Capitelli, "Collision integrals of high temperature hydrogen species," in *Atomic and Plasma-material Interaction Data for fusion (APID series)* **9**, Vienna International Atomic Energy Agency, 75-82, (2001).
- [62] R. Zorat and D. Vender, "Global model for an rf hydrogen inductive plasma discharge in the deuterium negative ion source experiment including negative ions," *Journal of Physics D: Applied Physics* **33** (14), 1728-1735 (2000).
- [63] J. R. Hiskes and A. M. Karo, "Analysis of the H₂ vibrational distribution in a hydrogen discharge," *Applied Physics Letters* **54** (6), 508-510 (1989).
- [64] T. Mosbach, "Effects of foreign gases on H⁻ formation in a magnetic multipole hydrogen plasma source," *Plasma Sources Science and Technology* **14** (2), 351-362 (2005).
- [65] T. Kuo, D. Yuan, K. Jayamanna, M. McDonald, R. Baartman, P. Schmor, and G. Dutto, "On the development of a 15 mA direct current H⁻ multicusp

source," *Review of Scientific Instruments* **67** (3), 1314-1316 (1996).

[66] J. J. Dang, K. J. Chung, and Y. S. Hwang, "A simple spectroscopic method to determine the degree of dissociation in hydrogen plasmas with wide-range spectrometer," *Review of Scientific Instruments* **87** (5), 053503 (2016).

[67] P. J. Eenshuistra, M. Gochitashvili, R. Becker, A. W. Kleyn, and H. J. Hopman, "Negative hydrogen ion densities and drift velocities in a multicusp ion source," *Journal of Applied Physics* **67** (1), 85-96 (1990).

[68] P. Svarnas, J. Breton, M. Bacal, and T. Mosbach, "Pressure optimization for H^- ion production in an electron cyclotron resonance-driven and a filamented source," *Review of Scientific Instruments* **77** (3), 03A532 (2006).

[69] E. Speth, M. Ciric, J. H. Feist, P. Frank, B. Heinemann, W. Kraus, F. Probst, R. Riedl, R. Trainham, O. Vollmer, and R. Wilhelm, "Rf ion sources for fusion applications: design, development and performance," *Fusion Engineering and Design* **46** (2-4), 383-388 (1999).

[70] M. Abdel-Rahman, V. S. v. d. Gathen, T. Gans, K. Niemi, and H. F. Döbele, "Determination of the degree of dissociation in an inductively coupled hydrogen plasma using optical emission spectroscopy and laser diagnostics," *Plasma Sources Science and Technology* **15** (4), 620-626 (2006).

[71] I. Charles de, "UV OH spectrum used as a molecular pyrometer," *Journal of Physics D: Applied Physics* **33** (14), 1697-1704 (2000).

Abstract in Korean

수소 음이온원에서 진동 여기 수소 분자의 거동에 대한 연구

수소 플라즈마 음이온 원은 핵융합로의 대표적 가열 및 전류 구동 장치인 중성 빔 입사 장치와 양성자 가속기의 이온원으로써 사용된다. 음이온의 높은 중성화 효율 때문에 위의 장치 들에서 선호되고 있다. 이러한 음이온의 생성 방식은 진동 여기 분자와 낮은 온도의 전자가 충돌하면 발생하는 전자 부착 해리 반응을 이용하는 체적 생성 방식과 세슘 등으로 도포된 표면과 충돌한 수소 원자나 이온이 전자를 얻어 음이온을 생성하는 표면 생성 방식으로 크게 구분된다. 서울대학교 음이온 원은 체적 생성 방식을 채택하고 있다. 그리고 음이온 생성의 효율성을 높이기 위하여, 원통형 음이온 원의 상부에는 평판형 고주파 안테나가 존재하며, 안테나 반대편에 위치하는 인출 전극 근처에는 이온 원의 축 방향에 수직한 필터 자기장을 인가하는 구조를 가지고 있다. 이에 따라 안테나와 필터 자기장 사이에서 주로 방전이 야기되고, 높은 전자 온도를 갖는 부분을 구동 영역이라고 칭하고 있다. 반대로 필터 자기장이 존재하는 인출 영역은 구동 영역에 비해 낮은 전자 온도를 갖는다. 구동 영역의 높은 전자 온도는 진동 여기 분자 생성에 효율적이며, 인출 영역의 낮은 전자 온도는 전자 부착 해리 반응에 효율적이면서, 동시에 음이온의 전자 해리 반응에 따른 손실을 줄일 수

있다.

이와 같은 설계에 따라서 이온 원의 플라즈마 물리를 이해하고, 특성을 파악하기 위해서 여러가지 진단 실험을 수행하였다. 기본적인 플라즈마 변수를 측정하기 위하여 랭뮤어 탐침 진단을 이온 원의 축 방향으로 이동하며 수행하였으며, 인출 영역에서 음이온의 밀도를 측정하기 위하여 Nd:YAG 레이저를 이용한 음이온 광 해리 진단 실험을 수행하였다. 본 연구에서 핵심이 되는 수소 분자의 진동 여기 상태를 진단하기 위하여 수소 분자의 방출광 중 하나인 Fulcher- α 띠 스펙트럼을 이용한 진단법을 도입하였는데, 낮은 여기 상태($v \leq 4$)의 분자는 진단이 가능하지만, 음이온 생성과 밀접한 관련이 있는 높은 여기 상태($v > 4$)의 수소 분자 진단에는 한계가 있었다. 따라서 입자 균형 방정식을 바탕으로 한 진동 여기 분포 함수의 전산 모사를 통해 진동 여기 분포 함수를 계산하고, 분광 실험 결과와 비교하였다. 그 결과 기존의 Fulcher- α 분광법은 진동 여기 분포 함수(vibrational distribution function, VDF)가 볼츠만 분포를 이루고 있다는 가정에 이루어지는데, 이 가정이 본 실험 장치에서는 적절하지 않음을 확인하였다. 이를 통해 개발된 무차원 모델을 이용하여 분광 진단의 한계를 보완하였다.

무차원 모델이 VDF와 분광 진단 사이의 관계를 규명하였음에도 불구하고, 음이온 밀도 계산 결과는 광 해리 실험 결과와 큰 차이를 보이고 있었다. 따라서 진동 여기 분자의 1차원 수송 현상을 추가적으로 고려하여, 구동 영역과 인출 영역이 분리되어 있는 서울대학교 음이온 원에 적합한 형태로 전산 모사를 개선하였다. 이로부터 진동 여기 된 수소 분자의 수송 과정에서 일어나는 분자 또는 원자와의 충돌에 의해 진동 여기 분포 함수의 완화가 발생함을

확인하였다. 구동 영역의 높은 전자 온도로 인하여 진동 여기 된 수소 분자는 확산 현상에 의하여 인출 영역으로 이동하게 되는데, 이 때 높은 여기 상태의 분자들은 충돌을 통해 낮은 여기 상태로 천이하게 됨을 확인할 수 있었다. 이러한 1 차원 모델은 음이온 밀도 계산에 있어서 큰 향상을 나타내었다. 특히 높은 운전 압력하에서 중성 입자들과의 진동-병진 운동 에너지 교환 반응이 증가하여 진동 여기 분포 함수의 완화가 중요해지고, 기존의 볼츠만 분포 모델 또는 무 차원 모델에서 보여지는 음이온 밀도의 과대 평가가 보정 될 수 있었다. 또한 개발 된 1 차원 모델을 짧은 길이의 이온 원 조건에 적용하였다. 그 결과 수송 거리를 짧게 설정하여 음이온 밀도를 계산한 결과가 수송 거리가 변하지 않는다는 가정에 따른 결과보다 정확하다는 것을 알 수 있었다. 즉, 진동 여기 분자의 수송이 이온 원의 길이에 의존하고 있음을 확인할 수 있었다.

위의 계산 및 실험 결과를 바탕으로 볼 때, 진동 여기 된 수소 분자의 수송 현상은 유효 평균 자유 행정 거리와 수송 거리라는 2 개의 특성 거리 값으로 대표될 수 있다. 유효 평균 자유 행정 거리는 확산 수송 속력을 유효 충돌 주파수로 나눈 값으로써, 구동 영역에서부터 인출 영역으로 진동 여기 분자가 이동하면서 완화가 일어나는 정도를 나타내는 값이다. 진동 여기 상태의 완화는 주로 진동-병진 운동 에너지의 교환 반응에 의해서 일어나기 때문에 유효 평균 자유 행정은 운전 압력에 크게 의존하게 된다. 수송 거리는 진동 여기 된 분자가 구동 영역에서 인출 영역까지 이동해야 하는 거리를 나타내는 값으로써 이온 원 길이에 의해 주로 결정되며, 플라즈마 변수 분포에 의해 일부 조정된다. 따라서 음이온 생성 효율을 높이기 위해서는 유효 평균 자유

행정 거리를 수송 거리 보다 길게 유지하여야 한다. 그러기 위해서는 가능한 낮은 압력에서 음이온 원을 운전해야 한다. 그러나 낮은 운전 압력은 전자 온도의 상승을 동반하므로 이를 조절하기 위해서는 강한 필터 자기장이 요구된다. 이 때 수송 거리를 짧게 하기 위해서 자기장이 인가되는 공간은 가능한 짧게 유지 되어야 한다. 이러한 자기장 구조의 영향은 TRIUMF에서 실험적으로 확인되었다. TRIUMF의 실험 결과에 따르면, 강하고 짧은 구조의 자기장이 음이온 생성에 효율적 임이 나타남에도 불구하고, 이의 이유를 구체적으로 설명하고 있지 않다. 따라서 본 연구에 따르면 이 현상을 쉽게 설명할 수 있게 된다.

수소 분자가 나타내는 또 다른 중요한 변수는 해리도 이다. 해리된 원자는 진동 여기 상태 완화와 음이온 파괴의 주 요인일 뿐만 아니라, 높은 해리도는 음이온의 생성 재료인 수소 분자 감소를 의미한다. 따라서 분광학적 측정과 모델링을 통해서 얻은 해리도 값과 음이온 밀도 사이의 관계에 대해서 조사하였다. 해리도는 전자 온도 또는 밀도의 상승에 따라서 같이 증가한다. 따라서 위에 언급된 음이온 운전 조건에 따라서 낮은 압력에서 운전하는 경우에도 해리도 증가에 따른 음이온 생성에 악영향이 발생하게 되어 음이온 밀도가 최대가 되는 최적의 압력 조건이 존재하게 된다. 또한 전자 밀도 증대에 따른 음이온 밀도 증가 효과를 가져오기 위하여 방전 전력을 높이는 경우에도 음이온 밀도를 무한정적으로 올릴 수 없게 된다. 음이온 밀도는 방전 전력 증가와 함께 증가하다가 포화 되는 현상을 나타내었으며 이는 음이온 생산을 위한 전력 효율의 감소를 의미한다.

본 연구에서 개발된 플라즈마 변수 바탕의 전산 모사를 통하여 펼쳐-알파 분광을 이용한 비-볼츠만 형태의 수소 분자의 진동 여기 상태

진단을 보완할 수 있었다. 또한 개선된 1 차원 모델을 이용해서는 진동 여기 수소 분자의 생성과 소멸 및 수송 과정 그리고 충돌에 의한 진동 여기 상태 완화 등을 확인 할 수 있었다. 게다가 효율적인 음이온 생산을 위해서는 유효 평균 자유 행정이 수송 거리보다 길어야 함을 도출하였다. 또한 수소 음이온 원의 운전 조건 최적화를 위해서는 플라즈마 변수만이 아니라 진동 여기 상태나 해리도와 같은 수소 분자의 거동 특성 또한 고려되어야 한다는 것을 알아냈다. 본 연구는 자기장 필터 방식의 음이온 원을 이해하는데 있어 큰 도움이 될 것으로 기대된다.

주요어: 수소 플라즈마, 수소 음이온원,
수소 분자 진동 여기 분포 함수, 펄처-알파 스펙트럼 분광,
입자균형방정식 모델, 수소 분자 수송 모델

학 번: 2011-30287